



**DESIGN ANALYSIS OF A SPACE BASED
CHROMOTOMOGRAPHIC HYPER SPECTRAL
IMAGING EXPERIMENT**

THESIS

Todd A. Book, Major, USA

AFIT/GA/ENY/10-M01

**DEPARTMENT OF THE AIR FORCE
AIR UNIVERSITY**

AIR FORCE INSTITUTE OF TECHNOLOGY

Wright-Patterson Air Force Base, Ohio

APPROVED FOR PUBLIC RELEASE; DISTRIBUTION UNLIMITED.

The views expressed in this thesis are those of the author and do not reflect the official policy or position of the United States Air Force, the United States Army, the Department of Defense, or the United States Government. This material is declared a work of the U.S. Government and is not subject to copyright protection in the United States.

AFIT/GA/ENY/10-M01

DESIGN ANALYSIS OF A SPACE BASED
CHROMOTOMOGRAPHIC HYPER SPECTRAL
IMAGING EXPERIMENT

THESIS

Presented to the Faculty

Department of Aeronautics and Astronautics

Graduate School of Engineering and Management

Air Force Institute of Technology

Air University

Air Education and Training Command

In Partial Fulfillment of the Requirements for the
Degree of Master of Science in Astronautical Engineering

Todd A. Book, BS, MBA

Major, USA

March 2010

APPROVED FOR PUBLIC RELEASE; DISTRIBUTION UNLIMITED.

DESIGN ANALYSIS OF A SPACE BASED
CHROMOTOMOGRAPHIC HYPERSPECTRAL
IMAGING EXPERIMENT

Todd A. Book, BS, MBA
Major, USA

Approved:

<hr/> <p>//signed//</p> <hr/>	<hr/> <p>10 Mar 2010</p> <hr/>
<p>Dr. Jonathan T. Black (Chairman)</p>	<p>Date</p>
<hr/> <p>//signed//</p> <hr/>	<hr/> <p>10 Mar 2010</p> <hr/>
<p>Dr. Richard G. Cobb (Member)</p>	<p>Date</p>
<hr/> <p>//signed//</p> <hr/>	<hr/> <p>10 Mar 2010</p> <hr/>
<p>Michael R. Hawks, Lt Col, USAF (Member)</p>	<p>Date</p>
<hr/> <p>//signed//</p> <hr/>	<hr/> <p>10 Mar 2010</p> <hr/>
<p>Eric D. Swenson, Lt Col, USAF (Member)</p>	<p>Date</p>

Abstract

This research develops the design of several components and/or systems for an experimental space-based chromotomographic hyperspectral imager that is being built by the Air Force Institute of Technology. The design work includes three separate topics.

The first topic was the development of a structure utilizing finite element analysis and eigenanalysis for the ground-based version of the chromotomographic experiment (CTEx). The ground-based experiment was performed as a risk mitigation measure for the space-based experiment.

The second topic includes a design review of a contractor's proposed off-axis Mersenne telescope for the space-based chromotomographic hyperspectral imager. The work included the creation of preliminary verification requirements from the contract and subsequent analysis of the telescope design based on those requirements.

The third topic addressed was a trade study of on-orbit focus, alignment, and calibration schemes for the space-based version of CTEx. The selected imaging focusing method entails imaging Earth-based sodium lights at night while stepping through several focus settings. The optimal focus setting shows the clearest sodium spectral features. The critical alignment concerns were identified as the alignment of the prism and of the collimated light onto the prism. The space-based CTEx utilizes three separate calibration methods involving vicarious Earth-based targets, and on-board laser diodes and spectral filters.

The results of the research varied by topic. For the first topic, a structural assembly was successfully fabricated that allowed the goals of the ground-based CTEx to be met, validating the design approach. The design review for the second topic was successful with the contractor's telescope design currently undergoing fabrication with delivery in May 2010. For the third topic, applicable methods and procedures were developed for the space-based CTEx.

Acknowledgments

First and foremost, I owe a large debt of gratitude to all my committee members (Dr. Black, Chairman; Dr. Cobb, Member; LTC Hawks, Member; and LTC Swenson, Member) for their tutelage, time and patience. It was with their guidance and direction that I was successfully able to complete this research.

Todd A. Book

Table of Contents

	Page
Abstract	iv
Acknowledgments	v
List of Figures	viii
List of Tables	xi
I. Introduction	1
1.1 Spectroscopy	2
1.2 Hyperspectral Imaging	7
1.3 Chromotomography	8
1.3.1 CTEEx - Lab-Based Experiment	10
1.3.2 CTEEx - Ground-Based Experiment	10
1.3.3 CTEEx - Space-Based Experiment	10
1.4 Problem Statement and Organization	11
II. Background and Theory	13
2.1 Literature Review	13
2.1.1 EO-1 (Hyperion)	13
2.1.2 HICO-RAIDS (HICO)	15
2.1.3 TACSAT 3 (ARTEMIS)	17
2.2 Structural Modeling	20
2.3 Off-Axis Mersenne Telescope	21
2.4 Hyperspectral Alignment and Calibration	25
2.4.1 Alignment and Focus	25
2.4.2 Spectral and Radiometric Calibration	28
2.5 CTEEx Theory	31
2.6 Summary	34
III. Ground-Based CTEEx Structural Design	36
3.1 Design Requirements and Methodology	36
3.2 Structural Modeling	38
3.2.1 Design Iteration One	38
3.2.2 Design Iteration Two	40
3.2.3 Design Iteration Three	44
3.2.4 Motor/Encoder Mount Design	48
3.2.5 Design Iteration Four	49
3.2.6 Design Iteration Five	51
3.3 Results	55

	Page
IV. Telescope Design Review	61
4.1 Methodology for Defining Verification Requirements	61
4.2 Requirements Verification	64
4.3 Results	76
V. CTE _x On-Orbit Focusing, Alignment, and Calibration	78
5.1 Methodology	78
5.2 Focusing	78
5.3 Maintaining Optical Alignment	80
5.4 Calibration	83
5.4.1 On-board Calibration	86
5.4.2 External Calibration	94
5.4.3 Lab Experiment	98
5.5 Results	102
5.5.1 Procedures	102
5.5.2 Design Requirements	104
VI. Conclusions	107
6.1 Ground-Based CTE _x Structure	107
6.2 Telescope Design Review	108
6.3 Focus, Alignment and Calibration	109
6.4 Proposed Future Work	110
6.5 Final Conclusions	112
Appendix A. Airborne/Spaceborne Spectral Imagers As Of May 2007 [1]	113
Appendix B. Verification Matrix	119
Appendix C. Telescope Minimum Design Requirements [2]	123
Appendix D. RCOS Selected Component Literature [3–8]	127
Appendix E. USGS Radiometric Questionnaire on Frenchman Flat [9]	145
Bibliography	161

List of Figures

Figure		Page
1.1	Electro-Magnetic Spectrum [10]	2
1.2	Spectroscopy Example [10]	3
1.3	Elemental Emissions [10]	3
1.4	Spectral Cube [10]	4
1.5	AVIRIS Images of Cuprite Mining District near Tonopah, NV [10]	5
1.6	AVIRIS Images of Cuprite Mining District near Tonopah, NV (400-1200 nm) [10]	6
1.7	AVIRIS Images of Cuprite Mining District near Tonopah, NV (2000-2500 nm) [10]	6
1.8	Spectral Imaging Classification [11]	8
1.9	Detonation Spectral Example [12]	9
2.1	Hyperion Sensor Assembly [13, 14]	14
2.2	CAD Drawing of HICO-RAIDS Experiment [15]	16
2.3	Japanese Experimental Module of the ISS [15]	16
2.4	CAD Drawing of the HICO sensor [15]	17
2.5	TACSAT 3 Artist's Conception[16]	18
2.6	Conceptual Mersenne Telescope and Imager for the CTE _x [17]	22
2.7	Optical Sketch of $F\ddagger$	22
2.8	Example Alignment Budget	26
2.9	Spectral Dispersal of an Hg Point Source [12]	32
2.10	Spectral Dispersion of Each Prism Position Overlaid as a Single Image Using Simulated Data[12]	33
2.11	Reconstruction of Simulated Chromotomographic Data into a Traditional Hyperspectral Cube [12]	34
3.1	FEMAP Model of Single Main Beam Structure	39
3.2	Conceptual Optical Component Placement Diagram [18]	40
3.3	FEMAP Beam Model of Original Structural Design	41
3.4	First Mode (28.56 Hz) for Model in Figure 3.3, Rocking about X-Axis, Green is Undeformed	42
3.5	Second Mode (59.48 Hz) for Model in Figure 3.3, Rocking about X-Axis, Green is Undeformed	42
3.6	Third Mode (61.31 Hz) for Model in Figure 3.3, Rocking about Y-Axis, Green is Undeformed	43

	Page
3.7	Forth Mode (91.22 Hz) for Model in Figure 3.3, Rocking about X-Axis, Green is Undeformed 43
3.8	Original Structure Modified with Box Structure 44
3.9	First Mode (29.14 Hz) for Model in Figure 3.8, Rocking about Y-Axis, Green is Undeformed 46
3.10	Second Mode (50.57 Hz) for Model in Figure 3.8, Rocking about X-Axis, Green is Undeformed 46
3.11	Third Mode (56.11 Hz) for Model in Figure 3.8, Rocking about X-Axis, Green is Undeformed 47
3.12	Forth Mode (80.32 Hz) for Model in Figure 3.8, Rocking about Y-Axis, Green is Undeformed 47
3.13	Fifth Mode (87.19 Hz) for Model in Figure 3.8, Rocking about X-Axis, Green is Undeformed 48
3.14	FEMAP Encoder Mount Model 49
3.15	FEMAP Model with Telescope Connected at Top 50
3.16	FEMAP Model with Telescope Side Mounted 52
3.17	First Mode (71.20 Hz) for Model in Figure 3.16, Rocking about Y-Axis, Green is Undeformed 53
3.18	Second Mode (92.02 Hz) for Model in Figure 3.16, Rocking about Y-Axis, Green is Undeformed 53
3.19	FEMAP Model with Telescope Side Mounted Including Reinforcement Plates 54
3.20	FEMAP Model with Telescope Side Mounted Including Plates and Spacer Blocks 56
3.21	Materials for Figure 3.20 model 56
4.1	RCOS Mechanical Layout for Off-Axis Mersenne Telescope [19] 65
4.2	RCOS Off-Axis Mersenne Telescope OAP Prescriptions [19] 66
4.3	RCOS Optical Layout and Image Simulation [19] 67
4.4	RCOS Root Mean Square(RMS) Wavefront Error(WFE) and Optical Path Differences [19] 68
4.5	RCOS Modulation Transfer Function and Point Spread Function [19] . . . 69
4.6	RCOS Off-Axis Mersenne Telescope Optical Alignment Tolerances [19] . . 71
4.7	RCOS Off-Axis Mersenne Telescope Monte-Carlo Simulation of Perturbations to Alignment Tolerances [19] 72
4.8	RCOS Off-Axis Mersenne Telescope Thermal Performance for Aluminum Breadboard[19] 73
4.9	RCOS Off-Axis Mersenne Telescope Thermal Performance for Invar Breadboard[19] 74

	Page
4.10	RCOS Proposed Mechanisms and Controllers [19] 75
4.11	RCOS Proposed Procurement and Delivery Schedule [19] 76
5.1	Conceptual imager design [19] 79
5.2	Graphic Depiction of a Mercury Line Source with Prism Rotation Angles of 0,90,180,270 Degrees 84
5.3	Theoretical Spectral Dispersion of the CTE _x Prism [17] 86
5.4	Theoretical Pixel Response Versus Log of Exposure Time 94
5.5	CEOS Reference Standard Test Sites [9] 97
5.6	LSPEC Frenchman Flat Radiometric Calibration Site Data Query Page [20] 98
5.7	Lab Experiment Setup 99
5.8	Array Saturation and Imperfect Collimation 100
5.9	Lasers Closely Aligned Showing Coincident Centers of Rotation for Four Prism Rotational Angles 101
5.10	Lasers Offset Showing Mis-Aligned Centers of Rotation 102
5.11	Theoretical CTE _x On-Orbit Initial Calibration Flow Chart 103
5.12	Theoretical CTE _x On-Orbit Maintenance Calibration Flow Chart 104
6.1	Constructed Portable Ground-Based CTE _x Imager [18] 107

List of Tables

Table		Page
3.1	Eigenvalue Analysis of the Design Shown in Figure 3.1	39
3.2	Eigenvalue Analysis of the Design Shown in Figure 3.3	42
3.3	Mode Shape Summary for the Design Shown in Figure 3.4 to 3.7	44
3.4	Eigenvalue Analysis of the Design Shown in Figure 3.8	45
3.5	Mode Shape Summary for the Design Shown in Figure 3.9 to 3.13	48
3.6	Eigenvalue Analysis of the Design Shown in Figure 3.15	51
3.7	Eigenvalue Analysis of the Design Shown in Figure 3.16	52
3.8	Mode Shape Summary for the Design Shown in Figure 3.17 to 3.18	53
3.9	Eigenvalue Analysis of the Design Shown in Figure 3.19	54
3.10	Eigenvalue Analysis of the Design Shown in Figure 3.20	57
3.11	Mass and CG Expected Values for the Model in Figure 3.20	60
5.1	On-Board Calibration Source DECMAT	89

DESIGN ANALYSIS OF A SPACE BASED CHROMOTOMOGRAPHIC HYPERSPECTRAL IMAGING EXPERIMENT

I. Introduction

This thesis is an engineering analysis of several components of a chromotomographic hyperspectral imaging experiment (CTEx). This experiment has three distinct iterations: a lab-based experiment, a ground-based experiment, and a space-based experiment. The ground-based experiment was created to further refine the technology of the lab-based experiment and as a risk mitigation measure for the space-based experiment. The space-based experiment will provide proof-of-concept to raise the technology readiness level for chromotomographic hyperspectral imaging to six [21].

This thesis is focused on the ground-based and space-based iterations of this experiment. Thesis work on the ground-based experiment includes the structural design. For the space-based experiment, there are two research topics. The first topic is a design review of a contractor's proposed telescope design for the imager. The second topic is an engineering design for the on-orbit alignment and calibration of the chromotomographic hyperspectral imager.

Remote sensing is a fundamental aspect of our human desire to learn more details about our environment. Hyperspectral imaging is one branch of this endeavor that is widely used for science and military activities. Current hyperspectral imagers are only capable of delivering spectral and spatial details of a static or slowly changing scene. However, a chromotomographic hyperspectral imager can deliver spectral, spatial, and temporal details, thus allowing not only the determination of location but also the classification and analysis of not only static scenes but very quick transient events, such as detonations and other combustion events. The previously described capabilities

are the fundamental reason for conducting a chromotomographic hyperspectral imaging experiment in order to validate the technology for future endeavors.

1.1 Spectroscopy

Prior to discussing the theory and technology for chromotomographic hyperspectral imaging, it is important to present the underlying science of hyperspectral imaging. We start this discussion by defining spectroscopy. Spectroscopy is the study of radiation that is transmitted, absorbed, emitted or reflected by different objects or mediums. This radiation can take many forms based on its wavelengths as shown in Figure 1.1. The human eye is only able to detect a small visible light portion of the electro-magnetic spectrum, which it can not separate into distinct wavelengths. Due to this limitation, instruments are necessary to characterize the electromagnetic spectrum.

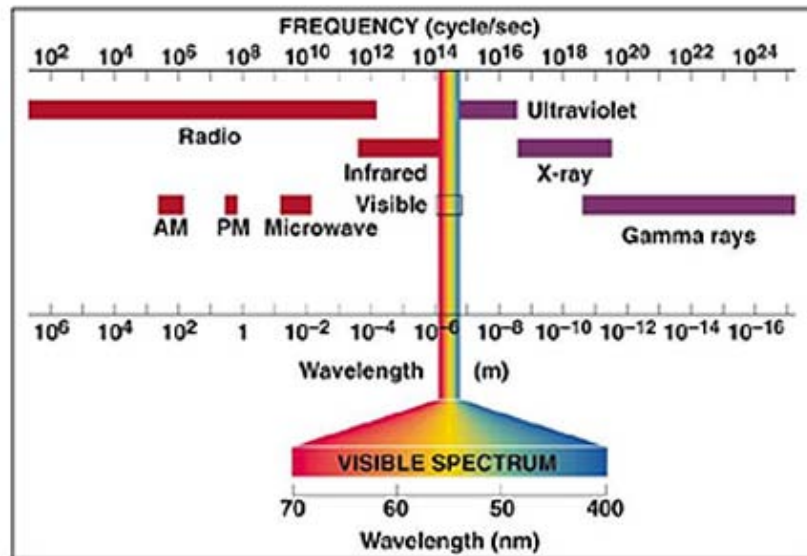


Figure 1.1: Electro-Magnetic Spectrum [10]

A fundamental aspect of spectroscopy is that every element and compound has a unique spectral signature. The idea of a spectral signature is displayed in Figure 1.2. The different wavelengths of light form a continuous spectrum when they are unobstructed as on the left of Figure 1.2. However, when the light spectrum must travel through a cloud of an unknown gas, such as a combustion plume, the underlying gaseous compound absorbs certain wavelengths of the light as shown by the absorption line spectrum on

the right of Figure 1.2. By looking at the emission line spectrum shown at the bottom of Figure 1.2, the compounds and elements of a combustion plume can be determined. Another example of elemental emissions for some elements is displayed in Figure 1.3.

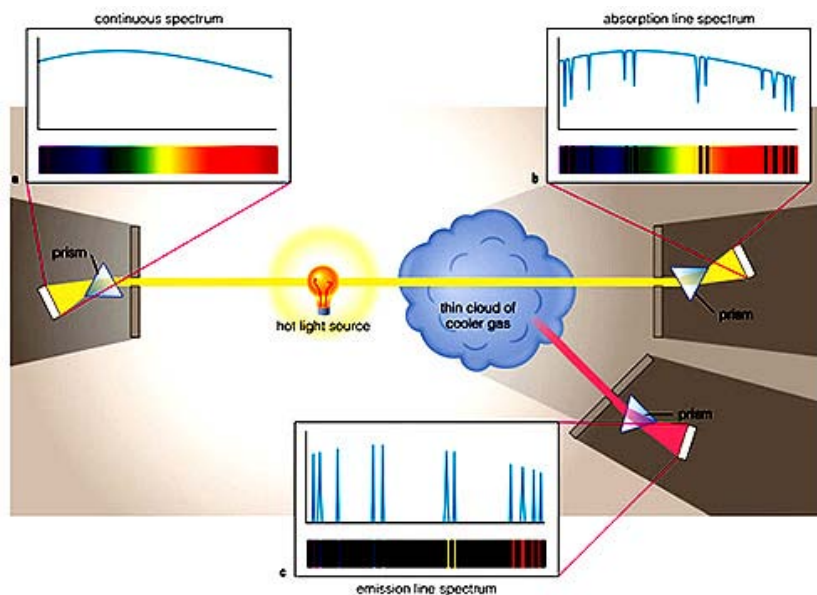


Figure 1.2: Spectroscopy Example [10]



Figure 1.3: Elemental Emissions [10]

The kind of spectroscopy that is the main focus of this report is imaging spectroscopy. In imaging spectroscopy, spectral information such as in Figure 1.3 is combined with the spatial information of each pixel to produce much more information than

a spatial image alone would have provided. The combined spectral information includes the reflected and emitted electro-magnetic spectrum from the imaged materials. The spectral information collected and combined with spatial information is only limited by the spectral bands that are utilized. Figure 1.4 shows how spectral information in each pixel can be turned into a continuous spectrum to provide an analyst more information than a spatial pixel alone would have provided. This near-infrared/visible continuous spectrum can then be analyzed to determine the underlying composition of that part of the target contained in that pixel or pixels.

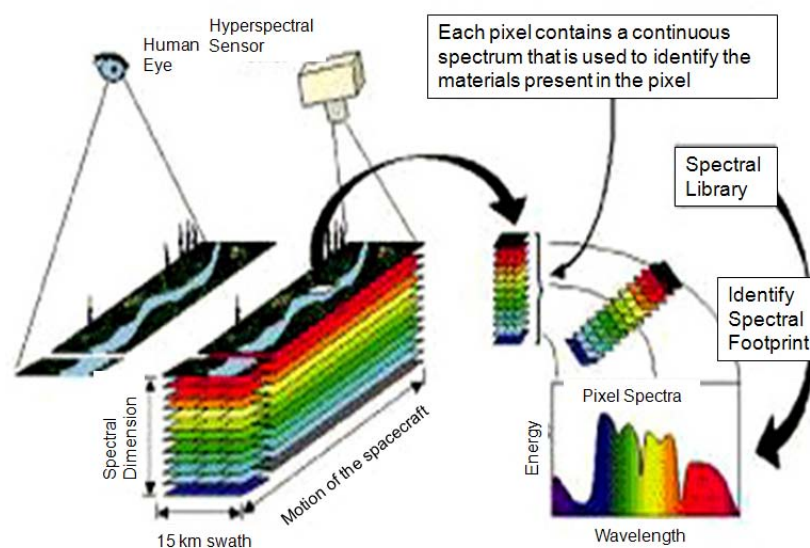


Figure 1.4: Spectral Cube [10]

By using spectroscopy in remote sensing, information that is not readily apparent in a spatial view becomes apparent. Figure 1.5 shows a spatial true color image of the Cuprite Mine District near Tonopah, NV taken by AVIRIS (Airborne Visible/infrared Imaging Spectrometer) [10]. The spatial information in this photo provides only terrain detail. Figure 1.6 taken by AVIRIS looking in the 400-1200 nm wavelength range incorporates the respective spectral information with the spatial information. This image clearly provides more information than the previous spatial image and allows it to be classified by the respective minerals. Figure 1.7 was again taken by AVIRIS, but used a different spectral wavelength range of 2000-2500 nm. This image shows that the

mineral content can be further refined by looking at the spectral reflectance and emissions in a different range of wavelengths. The information shown here produced by the AVIRIS imaging spectrometer would be very valuable to geologist and would save them considerable site exploration time.



Figure 1.5: AVIRIS Images of Cuprite Mining District near Tonopah, NV [10]

As shown in Figure 1.5 to 1.7, imaging spectroscopy is a very useful tool. In military applications, spectroscopy tactically allows a force to defeat an enemy's camouflage efforts. To the visible eye or a spatial search, an enemy's forces may be camouflaged and hidden to an analyst. Unbeknownst to the enemy, their camouflage efforts are futile because whatever they are trying to hide is still reflecting/emitting in some part of the electro-magnetic spectrum differently than its surroundings. A military analyst just needs to know in which part of the electro-magnetic spectrum to look in order to detect the enemy's forces or whatever they are trying to hide. Spectroscopy has numerous strategic military implications. Strategically, spectroscopy can be used to determine what different factories are producing by examining their emissions, the status of a country's food supply and crop yields, or what is being mined from open-pit mines. Spectroscopy

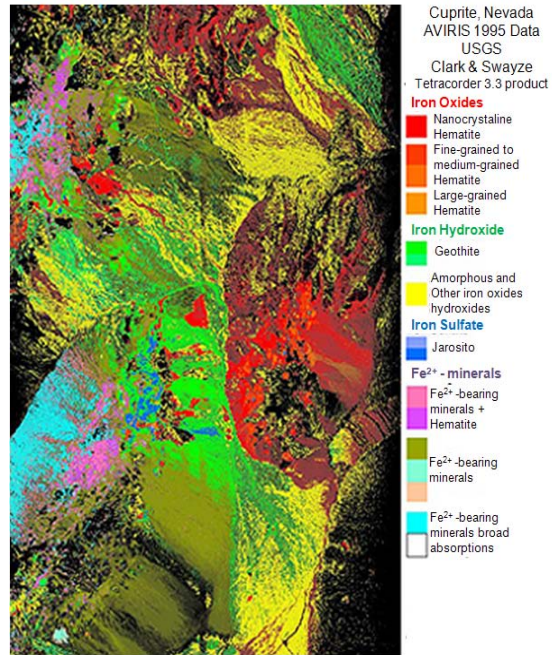


Figure 1.6: AVIRIS Images of Cuprite Mining District near Tonopah, NV (400-1200 nm) [10]

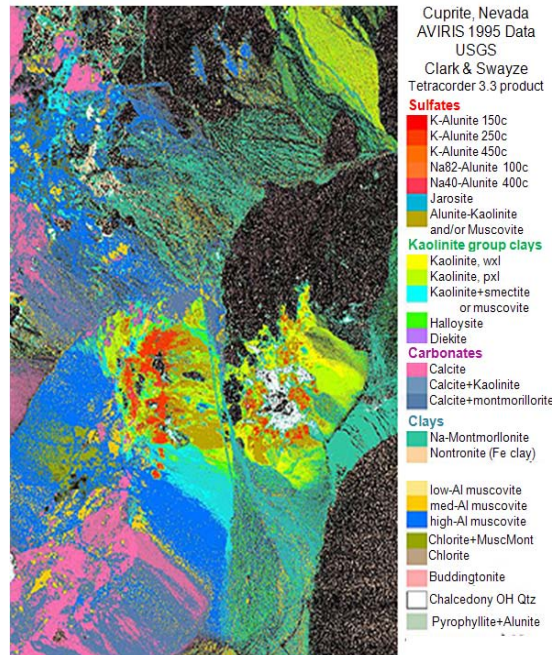


Figure 1.7: AVIRIS Images of Cuprite Mining District near Tonopah, NV (2000-2500 nm) [10]

has numerous other military and civil applications, with those cited here just being the tip of the iceberg.

For imaging spectroscopy, the instrument used is called a spectrometer. The main component of a spectrometer is a device to separate the incoming radiation into specific wavelengths. The simplest example of this device is a prism, as used in the chromotomographic experiment, but most spectrometers use gratings. The example hyperspectral imagers reviewed later in Chapter Two as part of the literature review, all use gratings. Appendix A provides a listing of not only space-based spectral imagers, but aircraft and handheld spectral imagers as well.

1.2 Hyperspectral Imaging

Imaging spectroscopy can be broken into separate classes as shown in Figure 1.8. The common classes used are multispectral, hyperspectral and ultraspectral. While there is no formal definition for each, all three differ by bandwidth and spectral resolution. Multispectral resolution has the lowest spectral resolution and focuses on several discrete spectral bands across the electro-magnetic spectrum rather than a continuous band. Ultraspectral resolution on the other hand has the highest spectral resolution, but covers a continuous spectral range, which means that it can detect very minimal spectral changes in a scene. Ultraspectral imagers usually have very low spatial resolution due to the data constraints imposed with the high spectral resolution. Hyperspectral imaging falls into the category between these two classifications; medium bandwidth and resolution, but the bands cover a continuous spectral range [11, 22]. Generally, hyperspectral imaging has enough spectral resolution for most applications. The chromotomographic imaging experiment covered in this thesis is a hyperspectral imager.

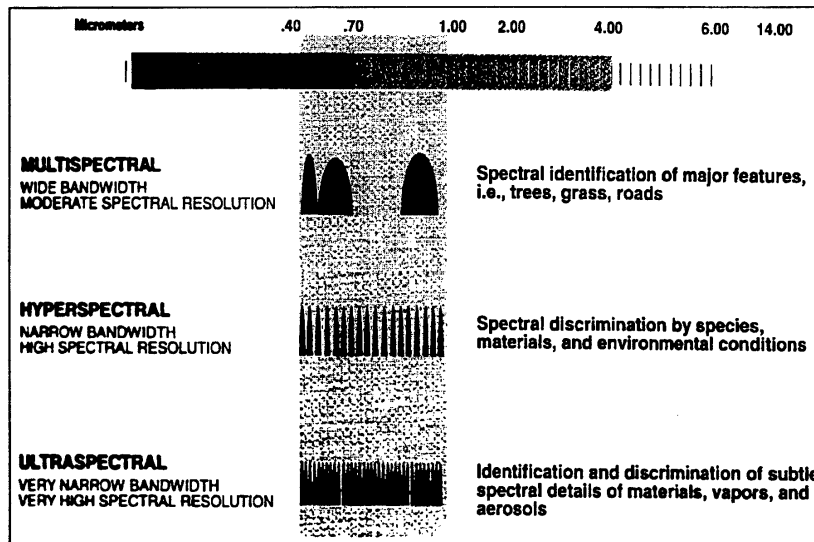


Figure 1.8: Spectral Imaging Classification [11]

1.3 Chromotomography

Hyperspectral imaging as shown in Section 1.1 is a valuable tool that combines spatial and spectral information from a target of interest, which can be exploited for scientific and military purposes. Traditional hyperspectral imaging, until recently, was only able to image static or slowly changing scenes. It was not able to combine a rapid temporal dimension with the spectral and spatial dimensions. There is current interest in being able to image fast transient events, less than 1/10 sec, such as explosions and muzzle flashes using hyperspectral imaging. However, in order to image fast transient events, an imager has to be able to successfully collect spatial, spectral and rapid temporal information at a rate equal to or greater than 10 Hz.

Chromotomography is one type of technology that can be used to image fast transient events in addition to others, such as Fourier Transform Spectroscopy (FTS). Chromotomography enjoys several advantages over FTS including less sensitivity to vibration, simpler integration, and increased temporal response [23]. The scientific concept for chromotomographic hyperspectral imaging originated with the Air Force Research Laboratory (AFRL) and Solid State Scientific Corporation (SSSC). The results of their work in chromotomographic hyperspectral imaging was published in *Compact*

Visible/Near-Infrared Hyperspectral Imager by Murguia, Reeves, Mooney, Ewing, Shepherd and Brodzik in SPIE [24].

At the center of the chromotomographic experiment at the Air Force Institute of Technology (AFIT) is a rotating prism and transforms similar to medical tomography to reconstruct the data. As mentioned earlier, most hyperspectral imagers use gratings to separate incoming wavelengths. Prisms used in chromotomography are a simpler device that can perform the same function to disperse the wavelengths of a collected spatial scene onto the Focal Plane Array (FPA). By rotating the prism, the spectral information is dispersed on the FPA at different angles, thus allowing the scene's spatial and spectral content to be reconstructed using tomography. In theory, in order to sample transient combustion events with a finite life of approximately 1/10 second, the prism would have to spin at a rate equal to 10 Hz. This performance is necessary to detect and classify detonation events whose spectral signature only lasts a fraction of a second as shown in Figure 1.9 [12].

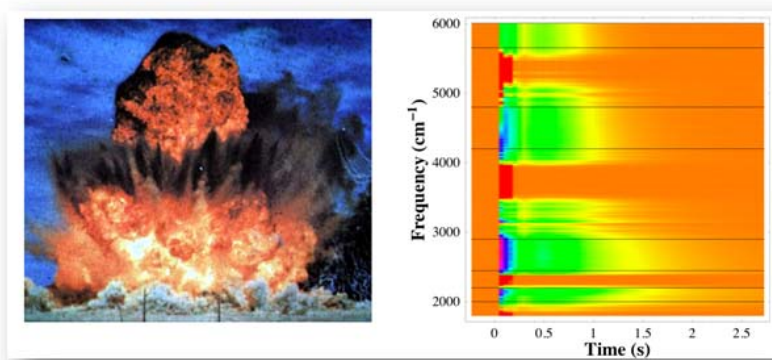


Figure 1.9: Detonation Spectral Example [12]

As mentioned earlier, the focus of the designs presented in this thesis is to support the chromotomographic experiment (CTEx) program taking place at AFIT. CTEx consists of three distinct experiments; a lab-based experiment, a ground-based experiment, and a space-based experiment. Each of these three experiments will be discussed further in the following subsections.

1.3.1 CTE_x - Lab-Based Experiment. Before this thesis effort started, the first lab-based experiment using chromotomography was already built and completed. The results of the lab experiment can be found in *Hyperspectral Imaging Using Chromotomography: A Fieldable Visible Instrument For Transient Events* by Bostick and Perram published in the International Journal of High Speed Electronics and Systems [23], and *Characterization of Spatial and Spectral Resolution of a Rotating Prism Chromotomographic Hyperspectral Imager* by Bostick, Perram, and Tuttle published in SPIE [25]. The AFIT research group met all its required goals, which included the following: [23]

- Construction of a chromotomographic hyperspectral imaging device
- Detailed performance characterization
- Demonstrate the capability to collect, process and exploit the spectral imagery for a primarily static spectral target

1.3.2 CTE_x - Ground-Based Experiment. The ground-based experiment results will be detailed in a master's thesis by O'Dell [18]. Part of the research in his thesis focused on the ground-based experiment and will be covered in Chapter Three. The main goals of the ground-based experiment include:

- Construction of a ground-based chromotomographic hyperspectral imaging device
- Demonstrate proof-of-concept outside the lab in a field environment using a changing spectral target at some distance

1.3.3 CTE_x - Space-Based Experiment. The initial research into the space-based chromotomographic imaging experiment has begun. The majority of the research in this thesis deals with the space-based experiment and is contained in Chapters Four and Five. For the space-based experiment, the system will be designed to interface with the Exposed Facility (EF) of the Japanese Experiment Module (JEM) on the International Space Station (ISS). On the ISS, the experiment will operate independently of the astronaut crew. The main goals of the space-based experiment include:

- Construction of a spaced-based chromotomographic hyperspectral imaging device that interfaces with the EF of the JEM
- Demonstrate a low-cost multi-functional chromotomographic imaging spectrometer that will provide visible-infrared (VIS-IR) hyperspectral imagery for transient combustion event classification [12]
- Raise the technology readiness level of chromotomographic hyperspectral imaging to 6

Three characterizations of different scenes are planned to achieve these goals, including: [12]

- Static hyperspectral scene, such as a tank through the trees
- Point source transient event, such as a salt emission line characterization of a burner
- Large transient event, such as a forest fire

1.4 Problem Statement and Organization

This thesis consists of three separate engineering design topics for the CTE_x at AFIT. The three topics covered have not been undertaken before, but are logical follow-on topics to work that was already conducted, such as the master's thesis by Sheirich [26], or is still on-going by the faculty and students at AFIT involved in this experiment. The three topics that are covered in this thesis include:

- Design and fabricate a supporting/mounting structure for the ground-based experiment
- Conduct a requirements verification review of a contractor's proposed design for a Mersenne telescope for the space-based experiment
- Design an on-orbit alignment and calibration scheme for the space-based experiment

For the research presented here, this document is organized into six chapters, not including appendixes. The first chapter is an introduction to spectroscopy, hyperspectral

imaging and chromotomography to provide the reader with a basic background into the overall experiment. Chapter Two contains all the background and theory information researched for the assigned space-based experiment topics. The third chapter covers the development of the ground-based experiment structure. Chapter Four covers the requirements verification review for the contractor's Mersenne telescope design prior to fabrication. The fifth chapter covers the on-orbit calibration and alignment system design. The final chapter, Six, covers the highlights of the proceeding chapters and makes recommendations for further research.

II. Background and Theory

A necessary step in research is to examine previous and current research in the field. This review is necessary in order to put this work into context with the state-of-the-art and find lessons learned from similar imagers and experiments. To do this, the literature review section of this chapter will be dedicated to the review of similar space experiments. The other sections will examine existing theory that is applicable to structural modeling, off-axis Mersenne telescopes, hyperspectral alignment and calibration, and CTE_x theory. The last section will provide a summary of the main points from this chapter.

2.1 Literature Review

In the field of spectral imagers, there are numerous space-based hyperspectral imagers that would offer insight into what is the current state-of-the-art. Several recent space-based imagers will be reviewed to define current technological trends in the field. This review will also describe how a chromotomographic hyperspectral imager such as CTE_x would contribute to the present efforts. The current imagers that will be reviewed include the EO-1 (Hyperion), HICO-RAIDS (HICO), and TACSAT3 (ARTEMIS).

2.1.1 EO-1 (Hyperion). The Hyperion imager on the Earth Observing One (EO-1) satellite represents the most advanced scientific hyperspectral imager currently in service today. It was launched on November 20, 2000 by NASA. The EO-1 satellite is in the same orbit as Landsat 7, trailing it by one minute. The EO-1 mission carries three separate payloads: the Advanced Land Imager (ALI), Hyperion Imaging Spectrometer, and Linear Etalon Imaging Spectrometer Array Atmospheric Corrector (LEISA or LAC). The focus of the following section will be on the Hyperion Imaging Spectrometer [27].

The mission objectives for the EO-1 program include: [28]

- Validate new technologies in-flight
- Provide useful data to the scientific research community

The Hyperion Imaging Spectrometer was built by TRW Space and Electronics for NASA. The instrument is a pushbroom imager that consists of three assemblies: Hyperion Sensor Assembly (HSA), Hyperion Electronics Assembly (HEA), and Cryocooler

Electronics Assembly (CEA). Figure 2.1 is a picture of the HSA, which is composed of a telescope, two grating spectrometers, calibration lamps, and focal plane electronics and cooling system. The telescope is a three mirror astigmat design with a field of view of 0.624 degrees by 42.55 microradians. One grating spectrometer is for the visible-near infrared (VNIR) and the other is for the short wave infrared (SWIR) [27]. Most of the imager's parts were custom fabricated.

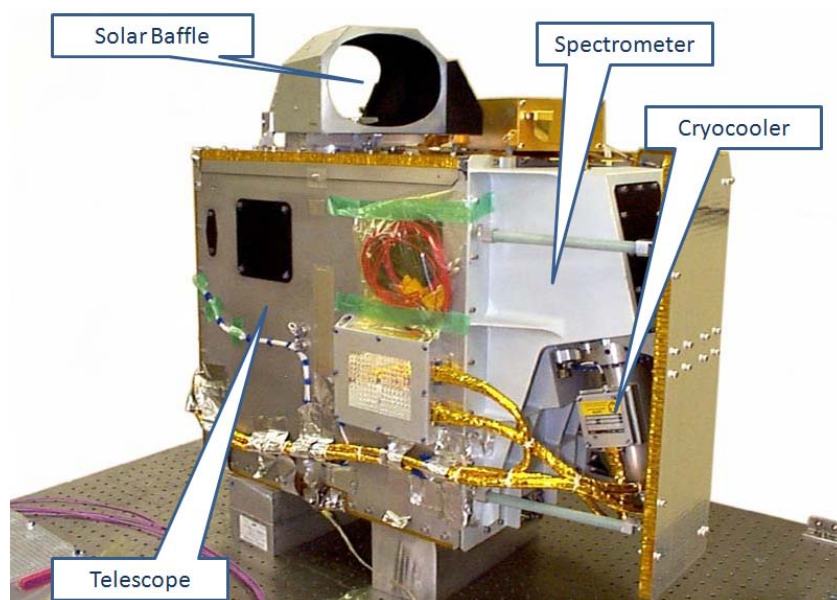


Figure 2.1: Hyperion Sensor Assembly [13, 14]

The Hyperion's performance represents the state of the art for scientific hyperspectral imagers. The use of two spectrometers allowed it to spectrally cover both the visible and near infrared parts of the electro-magnetic spectrum. It has a spectral range of 400 nm to 2500 nm with a spectral resolution of 10 nm. The hyperion's telescope provides a 30 meter spatial resolution. The hyperion is a pushbroom hyperspectral imager that is capable of sampling a swath of the earth 7.5 km wide and 20 km long from a 705 km altitude during each collect [14].

The Hyperion's data collection abilities have been instrumental in allowing scientist to monitor our planet. This has included, to name a few, monitoring the Amazon forest, lava flows, agriculture, and pollution; identifying and mapping vegetation species and minerals, and separating living and dead biomasses from soil [29]. Further details on earth observing experiments using hyperion and principle researchers can be found in

the article *Overview of the Earth Observing One (EO-1) Mission* by Ungar, Pearlman, Mendenhall, and Reuter published in IEEE [30]. This list is only the tip of the iceberg for Hyperion's past contributions to science, but with each day, scientists will find new ways for the Hyperion to assist in monitoring our changing planet.

2.1.2 HICO-RAIDS (HICO). The HICO imager located on the Naval Research Laboratory's HICO-RAIDS experiment, depicted in Figure 2.2, represents the most advanced hyperspectral imager for coastal bathymetry. The HICO-RAIDS experiment consists of two parts; the HICO (Hyperspectral Imager for the Coastal Ocean) experiment and the RAIDS (Remote Atmospheric and Ionospheric Detection System) experiment. The primary concern of this experiment is the HICO experiment, which is the hyperspectral imager payload. The HICO-RAIDS experiment was launched September 10, 2009 aboard a H2 Transfer Vehicle from Japan and is currently operational on the International Space Station (ISS) [31].

The mission objectives for the HICO program include: [31]

- Launch and operate the first spaceborne coastal Maritime Hyperspectral Imager(MHSI)
- Demonstrate the scientific and naval utility of MHSI from space
- Demonstrate new methods for the development of an operationally responsive space payload

The reason for taking a detailed look at this hyperspectral imager in addition to being the most advanced hyperspectral imager for coastal bathymetry is that the experiment will closely mirror that of the proposed space-based chromotomographic hyperspectral imager CTEx that is the focus of this research. Both experiments, in addition to being types of hyperspectral imagers, will be mounted on the Exposed Facility (EF) of the Japanese Experimental Module (JEM) on the ISS as shown in Figure 2.3. Although both imagers have different mission profiles and utilize different technology, there are many similarities, especially regarding ISS interfaces.

The HICO sensor in Figure 2.4 is a cross-track sensor designed for maritime coastal hyperspectral imagery. For maritime utility, the sensor is designed to have a higher sen-

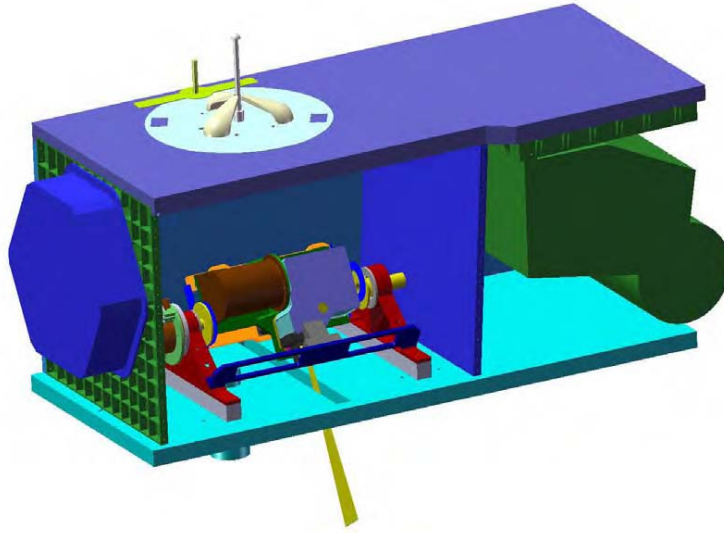


Figure 2.2: CAD Drawing of HICO-RAIDS Experiment [15]

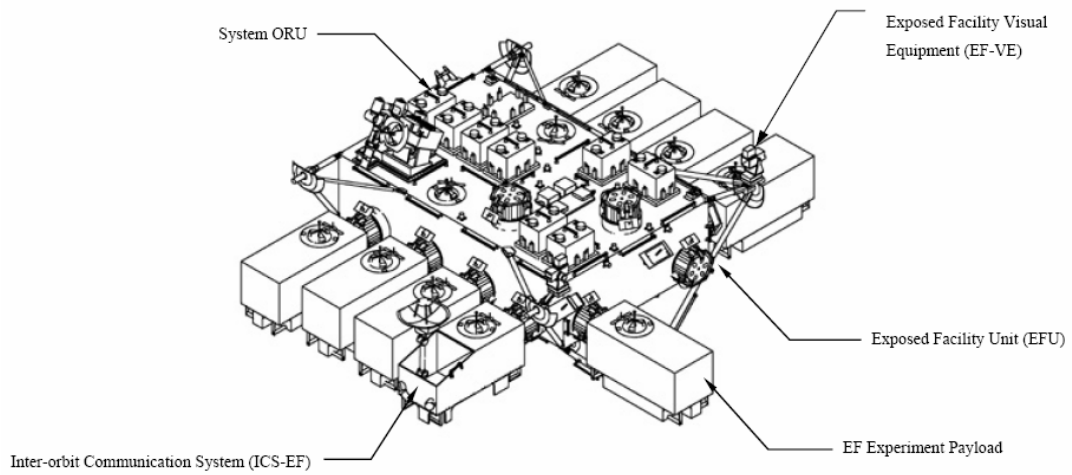


Figure 2.3: Japanese Experimental Module of the ISS [15]

sitivity to blue wavelengths and a high signal-to-noise ratio. Most of the HICO sensor is built from commercially available components. The spectrometer itself is a commercially available Brandywine Optics model 3035 Spectrometer that utilizes gratings. A Newport Research model RV120PEV6 rotation stage is used for pointing. Another commercially available item is the Rolera-MGI CCD Camera [15].

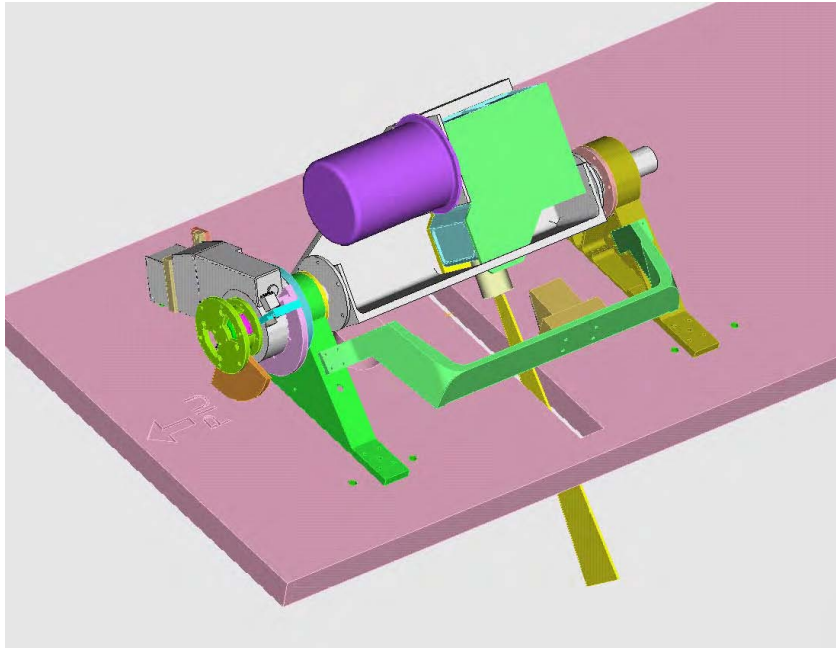


Figure 2.4: CAD Drawing of the HICO sensor [15]

The HICO's hyperspectral imaging abilities are unique. Its spectral range is from 380 nm to 1000 nm with a spectral resolution of 5.7 nm. HICO's optics give it a spatial resolution of only 100 m at nadir, which seems large when compared to other imagers, but is adequate to meet HICO goals. This gives the HICO the ability to capture a 50 km x 200 km scene per collection. Since HICO is focused on coastal bathymetry, it has some unique features, such as a greater sensitivity to blue wavelengths and a high signal to noise ratio of 200:1 [31]. With HICO just recently making it to orbit, reports further characterizing its orbital performance are expected in the future.

2.1.3 TACSAT 3 (ARTEMIS). The Advanced Responsive Tactically Effective Military Imaging Spectrometer (ARTEMIS) imager on Tactical Satellite 3 (TACSAT 3), depicted in Figure 2.5, is currently the most responsive hyperspectral imager. The

satellite is the third in a series of experimental satellites that were designed by the Air Force Research Laboratory (AFRL) and Operationally Responsive Space (ORS) Office of the Department of Defense. TACSAT 3 was successfully launched on May 19, 2009 aboard a Minotaur I rocket [32].

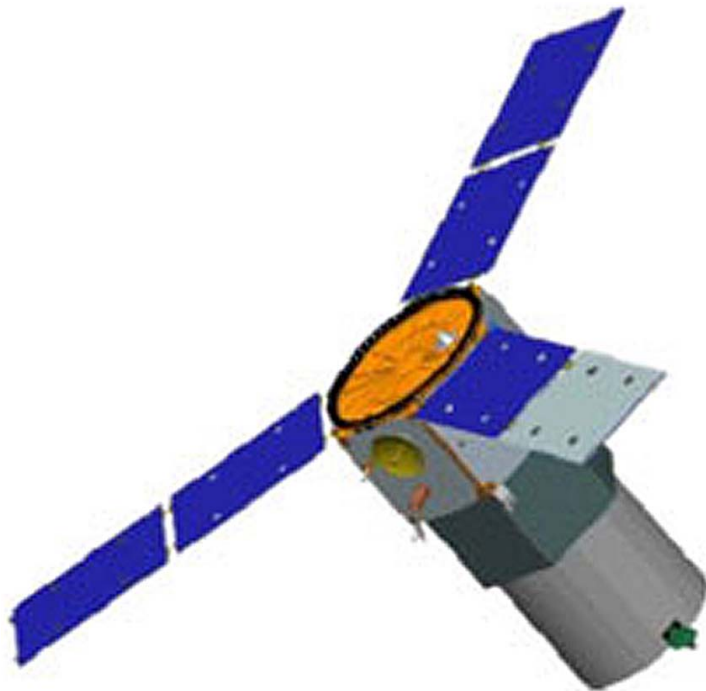


Figure 2.5: TACSAT 3 Artist's Conception[16]

The mission objectives for the TACSAT 3 program include: [33]

- Rapid response to a user-defined need for target detection and identification
- Rapid development of the space vehicle
- Rapid deployment from alert status for launch to theater control
- Responsive delivery of decision quality information to operational and tactical commanders by enabling tactical tasking and data delivery
- Deliver fieldable capability within reasonable cost constraints

TACSAT 3 includes three payloads; ARTEMIS built by Raytheon, the Office of Naval Research's Satellite Communications Package, and the Air Force Research Laboratory's Space Avionics Experiment. ARTEMIS, the hyperspectral imager, is the primary

payload on TACSAT 3, and is the reason that it is being reviewed for this research. The sensor was designed in 15 months at a cost of roughly 15 million dollars [34].

The ARTEMIS sensor is composed of a telescope, an image spectrometer, a high resolution imager, and a real-time processor. The telescope is a standard Ritchey-Chretien [35] design of less than 1 meter diameter with a built-in focus mechanism on the secondary mirror. The imaging spectrometer is the basic Offner [35] type with gratings. For this Offner design, multi-blaze gratings had to be perfected and were used for two purposes; one to reduce the effect of obscuration at the grating stop, and two to level the signal to noise ratio along all wavelengths [36]. The on-board health monitor, used to evaluate calibration, consisted of simple components, such as a low-wattage lamp, spectral absorption filter and pinholes on the end of the spectrometer entrance slit [37]. A modified Dalsa Piranha 2 line scan CCD camera was used. A simple improvement in the design over other spectrometers was that the ARTEMIS utilized only one focal plane like CTE_x, which contributed to its simplicity [36].

The designers for the ARTEMIS sensor were primarily concerned with maximizing optical quality while minimizing complexity and cost. The ARTEMIS sensor is a pushbroom hyperspectral imager designed as part of responsive space initiative for the tactical warfighter. For performance goals, the ARTEMIS system is designed to sample at 5 nm intervals with less than 5 percent spatial and spectral non-uniformity. The spatial and spectral non-uniformity is a big concern to ensure that the pixels are closely aligned in order to exploit the sensor data. For focusing, an image of a high frequency spatial scene is utilized. The focusing method is discussed more in Section 2.4.1 [38].

The greatest performance benefit of the sensor and satellite is that it is designed to provide tactical responsiveness for the warfighter. It does this by accepting taskings from tactical ground stations and then downloading the products back to tactical ground stations. This saves tremendous amounts of lead time for the warfighter, thus allowing the warfighter to make more informed and rapid decisions on the battlefield.

2.2 Structural Modeling

Chapter Three covers the design methodology for the development of the CTE_x ground instrument structure utilizing finite element (FE) modeling as the primary tool to evaluate conceptual designs and develop a design for fabrication. By using FE modeling, numerous configurations and changes are able to be evaluated with just labor to build the models, but without the expense and time of numerous fabrications and experimental testing. The primary result of the FE modeling is an eigenanalysis that allows the natural frequencies and modes of vibration of the structure to be examined, then the concept model or design can be altered to produce the desired results.

For structural design and analysis, the underlying theory of modal analysis was used. Natural frequencies are a fundamental property of a structure. For natural frequencies, there is an inverse relationship between stiffness and mass. For a single degree-of-freedom, the natural frequency ω for most cases is calculated using Eq. (2.1) [39],

$$\omega = \sqrt{\frac{k}{m}} \quad (2.1)$$

where k is the linear stiffness and m is the structural mass.

If the stiffness of a structure is increased, its structural natural frequencies are then increased. As mass is added to a structure, its structural natural frequencies are decreased. Since adding stiffness to a structure usually involves adding mass to it, care has to be taken to increase stiffness while minimizing the amount of mass in order to raise natural frequencies within a structure. The eigenvalue analysis used in FEMAP/-NASTRAN uses the basic mathematical formulation of the eigenvalue problem in Eq. (2.2) to calculate the natural frequencies ω for undamped free vibration with multiple degrees of freedom [39],

$$([K] - \omega^2[M])[d] = [0] \quad (2.2)$$

where $[K]$ is the stiffness matrix, $[M]$ is the mass matrix, and $[d]$ is the displacement vector. The size of the matrices is determined by the number of degrees of freedom in the

model. Solving the eigenvalue problem in Eq. (2.2) yields eigenvalues and eigenvectors that correspond directly to the natural frequencies and mode shapes of the structure.

2.3 *Off-Axis Mersenne Telescope*

Chapter Four covers the design review of a contractor’s proposed telescope design for CTE_x. The telescope is necessary to magnify the source image as well as collimate the light for CTE_x. Like the other space-based imagers in Section 2.1, a reflective mirror telescope will be utilized rather than a refractive lens telescopes for several reasons [26]:

- Mirrors do not introduce any chromatic aberration
- Mirrors provide a more stable structure
- Mirrors can be designed to provide a zero differential for thermal expansion coefficients between themselves and the structure
- Mirrors do not increase in weight as rapidly as lenses when size is increased

For CTE_x, an off-axis reflective Mersenne telescope was chosen by an earlier design trade study. The off-axis Mersenne is a two parabolic mirror design as shown in Figure 2.6. The Mersenne telescope was chosen because it had the most desirable characteristics of several telescope designs. It is compact to fit within the space requirements of the JEM external rack, provides room for a field stop to bound the image, and it allows the ability to collimate the image prior to the prism [26]. None of the space spectrometers in Section 2.1 utilized a Mersenne, but instead used a variety of other reflective telescope designs.

In order to understand the telescope design, certain optical properties, terminology and calculations must be reviewed. $F_{\#}$ is a ratio and is calculated using Eq. (2.3) [35],

$$F_{\#} = \frac{f}{D} \tag{2.3}$$

where f is the focal length and D is the entrance aperture diameter as shown in Figure 2.7. The lower the $F_{\#}$, the brighter the image will be because of a larger aperture

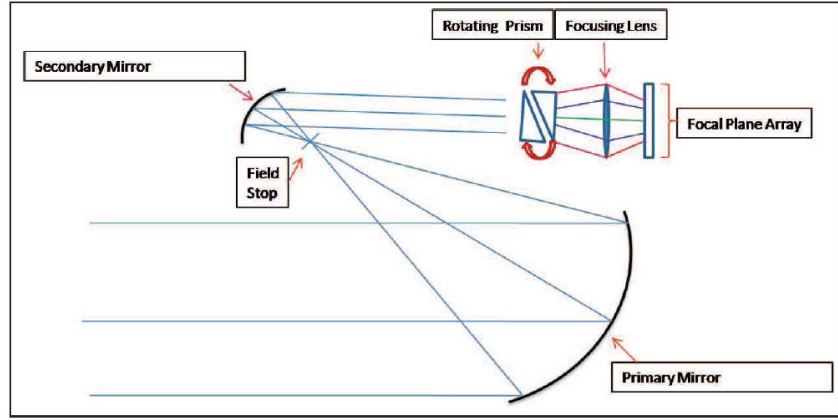


Figure 2.6: Conceptual Mersenne Telescope and Imager for the CTEX [17]

diameter that lets more light into the instrument. However, the shorter the focal length, the more pronounced the aberration error will be.

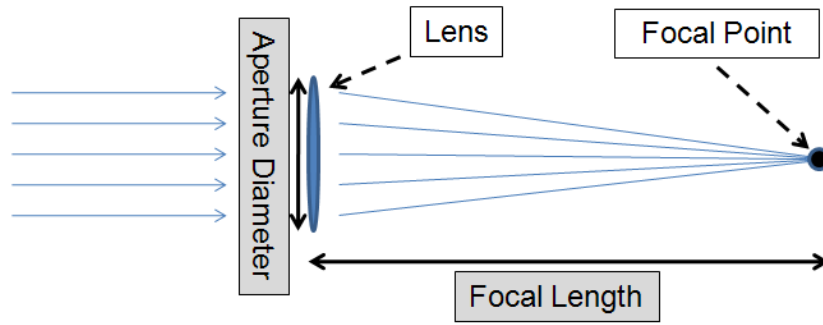


Figure 2.7: Optical Sketch of $F\sharp$

Magnification M is the ratio of image size to target size and is calculated using Eq. (2.4) [21],

$$M = \frac{f}{h} = \frac{r_d}{R} \quad (2.4)$$

where f is the focal length, h is the altitude (or slant range, if looking off-nadir), r_d is the image plane (detector) radius and R is the field of view radius. Field of view FOV is the area of the target encompassed by an image and is calculated using Eq. (2.5) [21],

$$FOV = \pi \left[\left(\frac{h}{\cos \eta} \right) \tan \left(\frac{\theta}{2} \right) \right]^2 \quad (2.5)$$

where R is the FOV radius, h is the altitude, θ is the angular diameter of the FOV , and η is the off-nadir look angle. Eq. (2.5) is only valid for small fields of view. The half angular field of view $\frac{\theta}{2}$ for a single optic system is calculated using Eq. (2.6) [21],

$$\frac{\theta}{2} = \arctan \frac{r_d}{f} \quad (2.6)$$

where r_d is the radius of the array and f is the focal length. Ground sampling distance GSD is the ratio of the target field of view to image size. It is expressed as length per pixel edge and is calculated using Eq. (2.7),

$$GSD = \frac{2h(\tan \frac{\theta}{2})}{Pixel(\cos(\eta))} \quad (2.7)$$

where $Pixel$ is the number of pixels per array side. Eq. (2.7) assumes that pixel and array dimensions are orthogonal and symmetric, and the angular field of view is small. Another equation for GSD is presented in Eq. (2.8) [40],

$$GSD = \frac{pp * range}{f * \sqrt{\sin \phi}} \quad (2.8)$$

where pp is the pixel pitch, $range$ is the slant range, f is the focal length, and ϕ is the ground elevation angle. All of the above equations will be useful in Chapter Four for analysis of the contractor's proposed Mersenne telescope design.

To analyze an optical system for aberrations, several fundamental tests can be utilized. The first one is to analyze the optical wavefront. A perfect optical wavefront is defined as a perfect sphere or plane. To characterize optical wave front errors the Root Mean Square (RMS) Wavefront Error (WFE) is measured. The WFE is the difference between the wavefront and a perfect wavefront. A useful way of analyzing the RMS WFE is to plot the RMS WFE over the Field of View (FOV). This shows how the RMS WFE grows as a function of the FOV, however, it must be remembered that large changes in the WFE on the edge of a FOV will not show up initially, since the RMS is an average [41]. In order to see large changes in the WFE on the edges of a FOV, the Optical Path Difference (OPD) must be analyzed. The OPD displays the difference between

the wavefront and a perfect wavefront for a specific FOV without taking the RMS. This allows changes in the WFE at the edges of a FOV to be recognized prior to showing up in the RMS WFE [41].

Another useful tool for the analysis of optical systems is the Modulation Transfer Function (MTF). The MTF tells how well an image can be resolved as a function of angular frequency. Angular frequency refers to the angular spacing between objects in an image. As the angular frequency would increase at some point the objects in an image would blur together as a one blob instead of distinct objects. For an ideal optical system, this relationship would be linear, but is not in most cases. To avoid issues, one would not want the MTF to drop off very quickly just as the angular frequency started to increase, but would want a slow, close to linear, decrease as the angular frequency increased [41].

The final tool to evaluate optical performance that needs to be reviewed is the Point Spread Function (PSF). The PSF represents how well a point is displayed, i.e. blurriness. For an ideal system, the PSF would have a large amplitude with a very narrow width. However, as system performance decreases, the PSF would change to a smaller amplitude with a larger width, thus showing the point is blurry [41].

The off-axis Mersenne telescope for the space-based CTE_x will use several parabolic and flat mirrors each with specialized optical properties that are worth some review. Parabolic mirrors have a focusing point, unlike flat mirrors which do not have a focus point. Parabolic mirrors do not cause spherical aberration, but coma and astigmatism are inherent [35]. Mirrors will not cause chromatic aberration, unlike lenses [21].

A field stop is also being used in the CTE_x telescope. There are two types of stops generally used in telescopes; an aperture stop and a field stop. An aperture stop is used to control the amount of light that reaches the image plane by limiting rays. A field stop is used to bound an image, thus restricting the field of view of an optic [35]. The use of a field stop is necessary in the CTE_x design in order to limit the spatial image on the array to allow sufficient room for the spectral image.

2.4 *Hyperspectral Alignment and Calibration*

Chapter Five is concerned with the alignment, focus, and calibration of the space-based CTE_x. The following subsection will provide some theory into these areas.

2.4.1 Alignment and Focus. While on-orbit, alignment and focus will be a concern for the CTE_x imager, because the optical path is usually sensitive to changes in tilt/pan or translation of the optical elements. Changes in alignment from ground to orbit usually happen as the result of four mechanisms: vibration, thermal changes, absence of gravity, and launch. Given that the ISS is a noisy environment for vibrations, the station can cause small changes in the tilt/pan or centering of optical elements at various frequencies. However, analysis of optical jitter is not included as part of this thesis. Thermal cycles on orbit can cause expansion and contraction of materials resulting in changes in the optical elements and beam paths. When the imager is built and tested, it will be subject to gravity on Earth. The absence of gravity in orbit can introduce changes in the optical path that were not present when built and tested on the ground. The final mechanism that can cause permanent changes in the optics is the launch environment, which will cause the greatest stress on the optical package during its lifetime. The CTE_x optics as discussed in Chapter Five will be subject to all of these mechanisms and must be capable of either remaining unchanged or capable of measuring the change and adjusting itself [21].

Proper alignment of the CTE_x imager consists of two components. The first is the optical alignment. Optical alignment is required in order to prevent aberrations in the optical images. The second part is the spatial and spectral alignment. The reason for doing spectral and spatial alignment is to be able to geo-reference the spectral data. For instance, if we wanted to collect data on a forest fire and there was no spectral and spatial alignment, from imager data, one could determine there was a forest fire, but one could not determine where it was located. If the instrument was aligned, one could determine the exact location and size of the forest fire.

Part of the alignment verification prior to launch includes the creation of an alignment budget before construction and alignment testing after construction to verify and

update the alignment budget. The alignment budget includes two parts: the actual assembly alignment errors after construction and estimated changes to the optical alignment caused by the environment over the lifetime of the imager. Figure 2.8 is an example of an alignment budget for a two mirror telescope and detector. The alignment budget provides a means to monitor alignment to ensure that pixel shift does not exceed the overall limits for the imager and may be a useful tool in ensure the alignment of the imager in Chapters Four and Five. During qualification testing the alignment is verified to ensure that it remains within overall design limits. Testing that qualifies the alignment includes a vibration test that simulates normal operational and the launch environments, a thermal vacuum test that simulates the thermal cycle of the operational environment, and a gravity test that ensures the optics remain aligned in the absence of gravity. Gravity testing can be performed by measuring the alignment, then flipping the instrument upside down and measuring the alignment again to ensure there is no change.

Component		Unit	Input	Shift (Pixels)	
				Spatial	Spectral
Primary Mirror	Dx	mm	0.02	0.5	
	Dy	mm	0.02	0.5	
	Dz	mm	0.01	0.1	
	tilt x	mrad	0.4	0.4	
	tilt y	mrad	0.4	0.4	
	tilt z	mrad			
Secondary Mirror	Dx	mm	0.03	0.6	
	Dy	mm	0.03	0.6	
	Dz	mm	0.04	0.4	
	tilt x	mrad	0.5	0.3	
	tilt y	mrad	0.5	0.3	
	tilt z	mrad			
Detector	Dx	mm	0.05	0.8	
	Dy	mm	0.05	0.8	
	Dz	mm			
	tilt x	mrad			
	tilt y	mrad			
	tilt z	mrad			
Image Shift (Pixels)				5.7	

Figure 2.8: Example Alignment Budget

Alignment can be controlled passively or actively. Passive alignment control measures include alignment budgeting, tight machine tolerances of optical parts, and selection

of materials, to name a few. Using tight machine tolerance in the manufacturing of optical systems leaves little room for the movement of optical components. Materials can be selected that have low thermal expansion/contraction properties. Active alignment can be performed using a variety of techniques that include alignment telescopes, lasers, or pinholes for the measurement of alignment errors, then a powered optical element to correct the aberrations.

An example of a passive alignment scheme is HICO. The imager was designed and constructed utilizing just aluminum to ensure alignment was not affected by difference in the rates of thermal expansion. Zemax was used to model the optical properties of the glass foreoptic to ensure that it stayed aligned and in focus when subjected to expected orbital thermal cycling. Ground vibration testing was utilized to ensure that the alignment could survive launch. To test alignment on orbit, HICO utilizes a small object with a distinct spectral signature and verifies if the dispersed light follows a column of pixels. However with passive measures, it was found that there was a two nm difference in spectral capabilities once HICO was on orbit that could possibly be attributed to changes in the alignment of the slit or focal plane array from launch [42]. Alignment for CTE_x is discussed more in Chapter Five.

Due to changes in focus while on orbit, the ability to maintain focus in the optical system must be explored. A focused image allows as much detail as possible from the optical system to be observed during a collect. An unfocused image occurs when the optics do not project a focus point on the collection array surface, but instead before or behind.

The incorporation of a focus mechanism into an optical path is relatively easy and is done by incorporating a motorized mirror or lens along the optical path. The difficult part of focusing an image is determining how to control the focusing mechanism to obtain the best focus. Focus control can be accomplished using a variety of feedback mechanisms. If there is more than one focus point within an imager, an image placed at an earlier focus point should also be in focus at the last focus point [17]. A second mechanism is using the pinhole technique and adjusting the focus to achieve the clearest light dot projected onto the array. The pinhole allows just a tiny dot of light to reach the

array to provide focusing feedback. The sharper the dot of light is; the more in focus the imager is. A final mechanism is using a vicarious scheme (an external calibration source) for focusing. In contrast, the HICO incorporates no active focus control, but relies on a fixed focus that was thoroughly analyzed and optimized through extensive modeling prior to launch [42].

An example of an optical instrument using a vicarious focus scheme is ARTEMIS on TACSAT 3, which would be useful for review, if a vicarious focus scheme is also used for the CTE_x focusing in Chapter Five. A cost driver for most imagers is active focus control. The ARTEMIS imager does include a secondary mirror focus mechanism as a trade-off to several other design methods, such as complex thermal control, structural modeling and testing. In order to focus the imager, a test location is selected with high spatial frequency content. The imager is stepped through its full range of focus settings while images are taken of the test scene. The spatial frequency of each image is then computed using a standard Fast Fourier Transform in MATLAB. The focus setting corresponding to the image with the highest spatial frequency is selected as the optimum focus position. An important note when determining spatial frequency found by the ARTEMIS development was that pixel to pixel non-uniformity will affect the spatial frequency of collected images, so pixel gains should be adjusted for uniformity, prior to utilizing this focus method [37].

2.4.2 Spectral and Radiometric Calibration. Like any measurement system, calibration of measurement mechanisms is necessary to ensure the validity of data that is collected. On orbit, hyperspectral imagers require two types of calibrations: spectral and radiometric. Spectral calibration of an imager is performed to determine if the actual spectral response of each pixel aligns with the theoretical spectral response. Radiometric calibration of an imager is performed to measure the intensity of a response against theoretical response intensity at a pixel. Both calibrations are necessary on orbit because spectral and radiometric characterization of the imagers changes from the ground characterization due to launch stresses, equipment aging, thermal cycles, atmosphere, etc.

Spectral calibration is performed on orbit either using on-board spectral calibration sources, vicarious sources, or both. The following is a list of orbital spectral calibration schemes used by the imagers in Section 2.1.

- Hyperion (EO-1) - Solar spectral features [28]
- HICO (HICO-RAIDS) - Measuring the known positions of atmospheric absorption lines and Fraunhofer lines [42]
- ARTEMIS(TACSAT 3) - Atmospheric absorption features with on-board filter to monitor trending between atmospheric spectral calibrations [43]

Like spectral calibration, radiometric calibration is accomplished through on-board sources, vicarious sources, or both. The following is a list of orbital radiometric calibration schemes used by the imagers in Section 2.1.

- Hyperion (EO-1) - Utilizes solar-based measurements. On-board lamps reflected off of a calibration panel used to monitor changes in radiometric calibration between solar-based measurements. [44]
- HICO (HICO-RAIDS) - Utilizes imaging of selected test ground sites [42]
- ARTEMIS (TACSAT 3) - Utilizes imaging of selected test ground sites [43]

In the previous calibration scheme examples, there seems to be a trend for not using on-board calibration sources for primarily calibration, but to use either the sun, moon, atmosphere or earth-based targets. On-board calibration sources are primarily utilized to measure calibration stability and changes between regular calibrations. There are a couple of reasons for this, including the fact that external calibration sources do not drift over their lifetime on orbit, and they allow an improvement in calibration accuracy. The byproduct of not using complex internal calibration schemes is that it lowers the cost of the imager. Calibration schemes for CTE_x will be discussed in Chapter Five.

These principles were further stressed during the development of the ARTEMIS sensor as part of TACSAT 3. Two ways of reducing payload cost as demonstrated by the ARTEMIS development were to eliminate complex on-board calibration systems and limit ground characterization of radiometric, spectral and spatial properties of the

imager. On ARTEMIS, only the minimum essential ground testing was performed prior to launch for the characterization of items that could not be done on orbit. For on-board calibration hardware, ARTEMIS only uses simple components, such as a low-wattage lamp, a spectral absorption filter and pinholes on the end of the spectrometer entrance slit. These pieces of hardware are included to only monitor changes in system calibration stability between external calibrations. The lamp is used to monitor radiometric stability. The filter is used to monitor spectral stability. The pinholes in the entrance slit are used to detect changes in the spatial response. The problem with using on-board sources for primary calibration is that they trend unknowingly with time, but by using vicarious calibration, as in the case of ARTEMIS, this problem is removed. The operationally responsive space mindset used in developing the ARTEMIS calibration scheme resulted in delivery of the ARTEMIS sensor quickly and at low cost [37].

To better understand how vicarious calibration works, the ARTEMIS sensor's use of it is reviewed. To accomplish radiometric calibration for verifying data accuracy, ARTEMIS uses a two part process. The first part uses a spectrally and spatially uniform target to detect differences in pixel responsiveness. Examples of uniform targets include lake beds, ice sheets and deserts. From the collect on the uniform target, each pixel i and spectral channel j is assigned a raw digital number $DN_{raw}(i, j)$. A corrected average digital number for each pixel and spectral channel DN_{corr} is computed by using Eq. (2.9) [37],

$$DN_{corr}(i, j) = \frac{DN_{raw}(i, j) - b(i, j)}{g(i, j)} \quad (2.9)$$

where b is the pixel bias for each spectral channel that comes from a deep space look, and g is a relative pixel gain for each pixel and spectral channel. DN_{corr} computed in Eq. (2.9) represents the average pixel/channel response for the imaged uniform scene, and the corrections determined here can be applied to later targets to equalize pixel/channel responses [37].

From the image of the second calibration target, the average corrected digital number $DN_{corr}(Target)$ is calculated once again using Eq. (2.9). Once done, the absolute gain for each spectral channel $G(j)$ is calculated by using Eq. (2.10) [37],

$$G(j) = \frac{DN_{corr}(target)}{L_{\lambda(j)}} \quad (2.10)$$

where $L_{\lambda(j)}$ is the predicted radiance spectrum at the top of atmosphere for the calibration target. From the gain calculated in Eq. (2.10), the absolute radiance measured by the ARTEMIS sensor for each spectral channel $L(j)$ is calculated using Eq. (2.11) [37],

$$L(j) = \frac{DN_{corr}(i, j)}{G(j)} \quad (2.11)$$

To conduct vicarious spectral calibration for ensuring spectral data accuracy, ARTEMIS utilizes atmospheric absorption features. The atmospheric spectral absorption features utilized for spectral calibration include the 760 nm oxygen feature, 940 nm and 1140 nm water features, and a 2010 nm carbon dioxide feature. A MODTRAN atmospheric model is used with the ideal ARTEMIS spectral response function. Using the model data and measured spectral data of these features, fit statistics are performed to first center the channels and then determine the channel's width [43].

2.5 CTE_x Theory

As mentioned in Chapter One, the theory for chromotomographic hyperspectral imaging originated with the Air Force Research Laboratory (AFRL) and Solid State Scientific Corporation (SSSC). The results of their work in chromotomographic hyperspectral imaging was published in *Compact Visible/Near-Infrared Hyperspectral Imager* by Murguia, Reeves, Mooney, Ewing, Shepherd and Brodzik in SPIE [24]. This research in chromotomographic hyperspectral imaging served as the basis for the start of CTE_x at AFIT.

The actual operation and theory of the ground-based CTE_x mechanism is of interest in order to develop the requirements for the space-based CTE_x calibration scheme in

Chapter Five. Three basic concepts of chromotomography need to be reviewed. The first is why the spectral points for a spatial pixel source lie along a line and why the spacing along the line is important. The second is why the line rotates and what determines the center of rotation. The third is how the algorithm takes this raw data and reassembles a traditional spectral cube for a pixel.

Figure 2.9 represents the first concept on why the spectral points for a spatial pixel source lie along a line and why the spacing along the line is important. The collimated Hg point source is dispersed by the prism by wavelength as a line onto the camera array. The spectral signature of the collimated Hg point source and the dispersion by the prism determines where the signature is recorded along the spectral line on the array. The location along the line represents the spectral wavelength of the source.

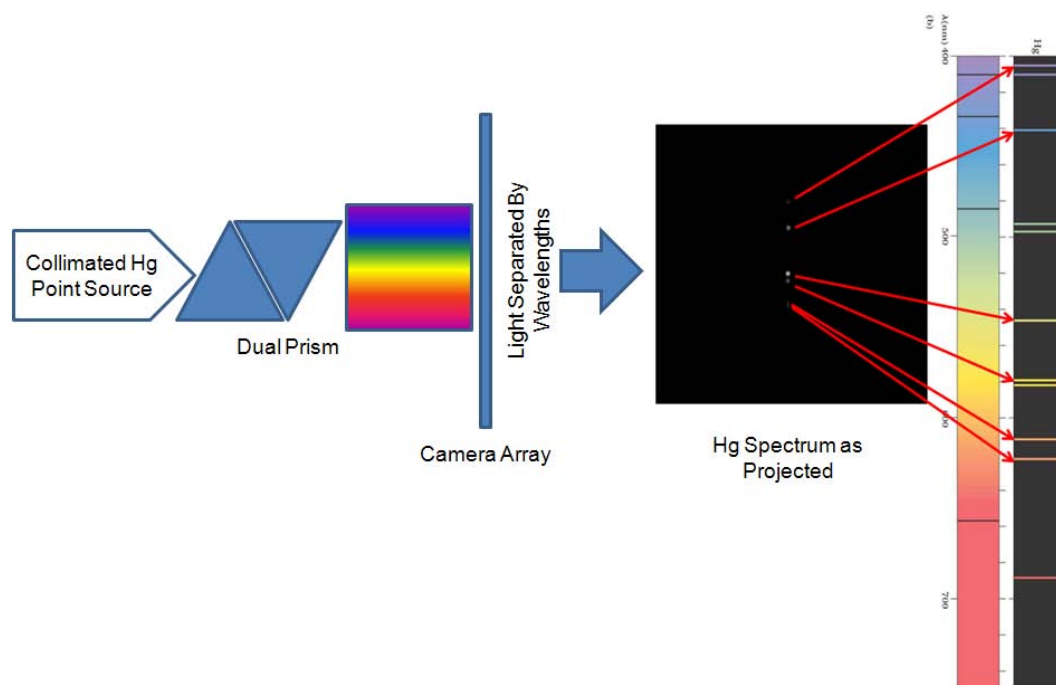


Figure 2.9: Spectral Dispersal of an Hg Point Source [12]

Figure 2.10 represents the second concept why the spectral line rotates and what determines the center of rotation. For simplicity only four prism angles are depicted in Figure 2.10, but center image is a composite of over a hundred prism angles. The reason that the image rotates is because the prism rotates. The prism is rotated in order to allow for the chromotomographic data to be reconstructed into a traditional

spectral cube, which will be explained as part of the third concept below. The center of rotation represents the undeviated wavelength of the spatial pixel being imaged. This is the wavelength whose path is not altered by the prisms. In the case of the ground-based CTE_x, this undeviated wavelength is approximately 550 nm.

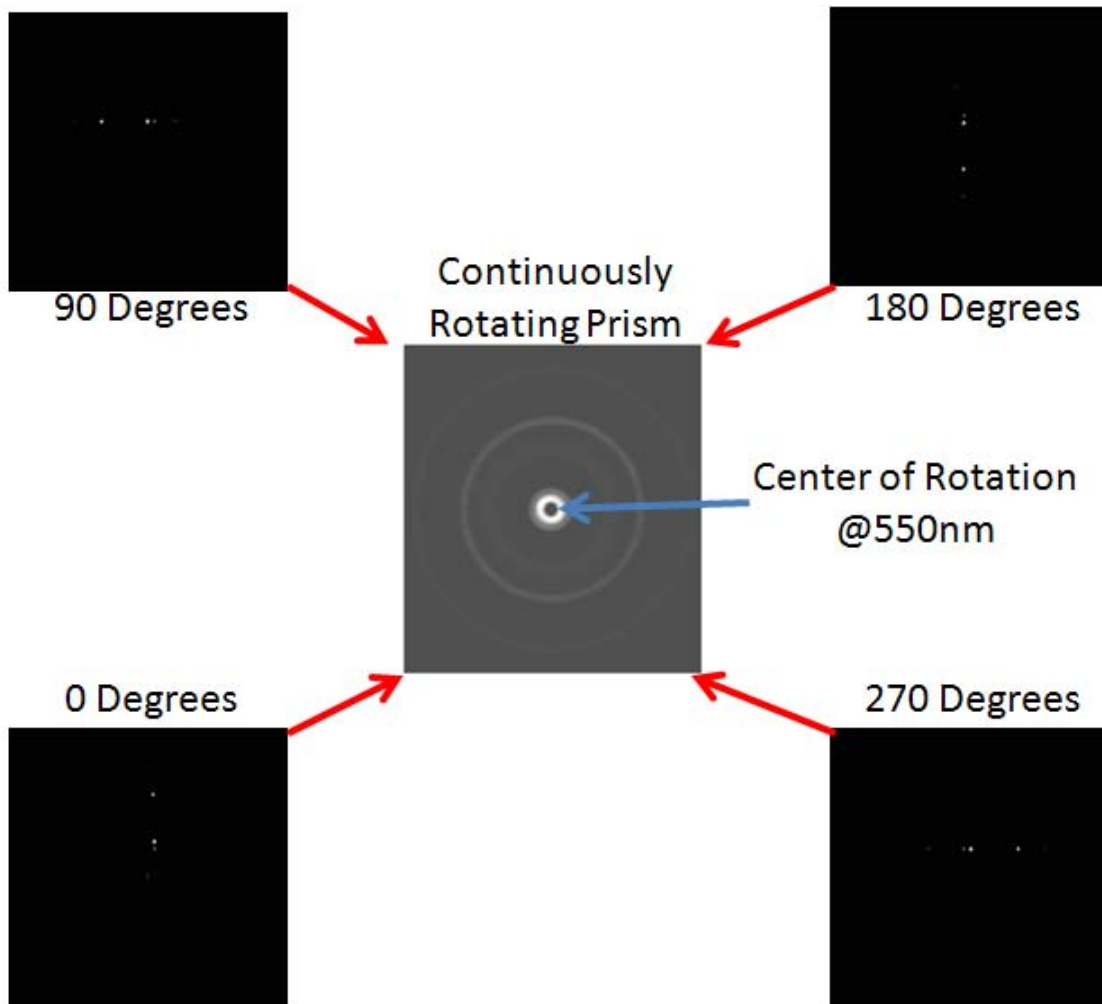


Figure 2.10: Spectral Dispersion of Each Prism Position Overlaid as a Single Image Using Simulated Data[12]

Figure 2.11 represents the final concept on how the algorithm takes this raw data and reassembles a traditional spectral cube for a pixel. The figure shows an example of how two spectral wavelengths are reconstructed for a single spatial pixel using the chromotomographic data. Since each location from the center of rotation represents a wavelength, the reconstruction algorithm takes a frame of the wavelength location at each prism angle. For simplicity, only eight prism angles are represented. The frames

are then dragged to the spatial pixel location, which is the center of rotation, and overlaid on top of each other to form a single spectral image for that wavelength and pixel. Since adjacent spatial pixels would add noise to each frame, the images are overlaid. In the case here, only a single spatial pixel is shown, but in reality, the field of view would contain numerous spatial pixels, which would add noise to the reconstruction process. To overcome the noise issue, the more prism angles that are imaged, the less noise is present in the reconstruction because more images would be overlaid causing only spectral features for that spatial pixel to show up.

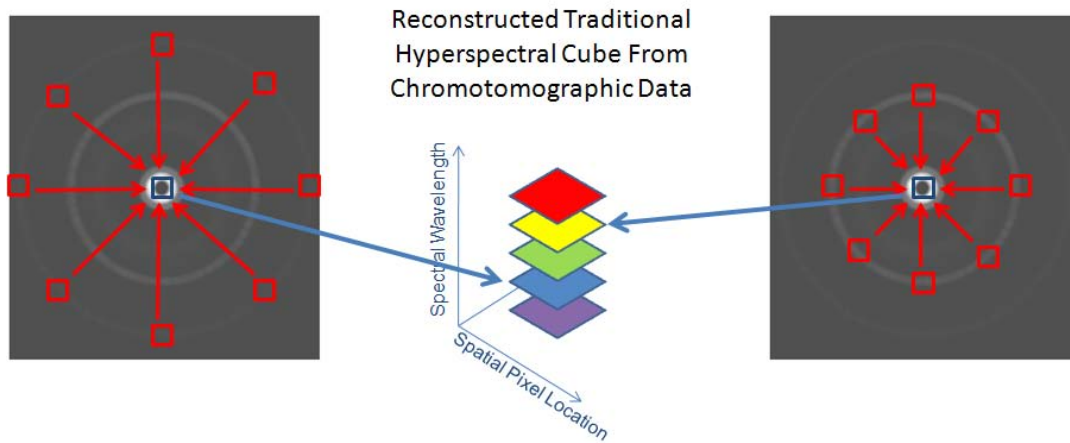


Figure 2.11: Reconstruction of Simulated Chromotomographic Data into a Traditional Hyperspectral Cube [12]

2.6 Summary

The information presented in this chapter will be used directly or indirectly in the following chapters for research. There are a few takeaways that should be highlighted prior to doing further research.

Looking at other state-of-the-art imagers in Section 2.1, CTE_x is designed to fill a niche that is not currently covered. CTE_x will be able to produce a higher temporal resolution than existing hyperspectral imagers. This ability puts CTE_x technology at the cutting edge in hyperspectral imager development and warrants its further development and exploitation.

Modeling is a very useful tool for the development of imagers today. Modeling allows designs to be optimized without incurring significant developmental costs. Modal analysis through FE modeling will be a useful tool in developing the CTE_x ground structure in Chapter Three. Optical modeling used by the contractor for the telescope performance will be critical in evaluating the potential design for the design review in Chapter Four.

Simplicity in the design and operation of the imager decreases cost and risk to the overall mission. The simplest solution for each trade needs to be considered first in the following chapters. Examples of simple solutions that need to be reviewed for inclusion are the following: the incorporation of passive optical alignment measures in Chapters Four and Five maybe more beneficial than the use of active alignment mechanisms, the exploration of vicarious focus and calibration schemes, if feasible in Chapter Five, would simplify the imager design.

These are only a couple of the highlights brought out from Chapter Two. There will be other information from this chapter discussed in the following research that will contribute greatly to the understanding and advancement of the CTE_x space-based imager design.

III. Ground-Based CTE_x Structural Design

This chapter will cover the structural design for the ground-based CTE_x instrument. The ground-based CTE_x instrument was constructed to further refine the understanding of how to design, build and test the space-based CTE_x as a risk mitigation measure. This chapter contains three subsections: design requirements and methodology, structural modeling, and results.

3.1 Design Requirements and Methodology

The design for a ground-based instrument structure had to meet several requirements. These requirements provided a baseline for the initial structural design and are listed below.

- Mount all experimental components including:
 - Vixen R200SS Telescope [45]
 - Phantom V5.1 Camera [46]
 - Allied Motion Tech. CM5000 Hollow Shaft Motor/Encoder with prisms [47]
 - Field Stop
 - Lens
 - Necessary turning mirrors
- Be portable to a field location
- Provide enough rigidity to ensure the optical path is not distorted during data collection
- Meet optical distance requirements and allow for adjustment of the optical components along the optical path
- The maximum tilt moment generated on the tripod should not exceed its capacity of 50 ft-lbs [48]
- Use 80/20 for fabrication, whenever feasible [49]

The driving requirement for the structure found during initial analysis was creating a structure with high rigidity [17]. Movement in the optical path during data collection would cause the pixels to be mis-aligned in the data cube resulting in either bad data or the need for extensive software to realign the data cube pixels. For the structure, this translated to ensuring that vibrations resulting from the motor spinning the prism did not correspond to structural natural frequencies of the structure itself. Since the maximum operating speed of the motor/encoder was 25 Hz, all structural natural frequencies had to be above 25 Hz to minimize the chance of data cube distortion during collection from the structure resonating at natural frequencies.

Designing the structure to ensure structural natural frequencies are not in the excitation range of the encoder does not guarantee that the data cube and data collection will be un-effected by the motor/encoder vibrations. It does ensure that movement along the optical path is not amplified as in the case of the structure having a resonance frequency at or near the same frequency as the motor/encoder operating speed. If the encoder does not affect structural natural frequencies and there is a problem with vibrations, then either a damping system would have been needed for the motor/encoder or software would have to remove the vibrational issues from the data cubes.

The methodology for creation of the ground-based instrument's structure was primarily based on FE modeling for design. Numerous FE models of structures were able to be modeled and analyzed quickly and cheaply. Once the modeling produced an acceptable structure that met all requirements, it was fabricated by AFIT's model shop. Because the modeled structure's predicted first mode requirement (100 Hz) is four times the 0-25 Hz motor/encoder operating speed, experimental testing was not performed because the model showed that structural frequencies were sufficiently above excitation of the motor/encoder. If there was a later issue in the ground experiment with lining up the pixels in the data cube, then experimental testing would confirm if any modes were below 25 Hz and if so the structure would have been stiffened even more.

This methodology is focused strictly on designing a structure using eigenanalysis to ensure the motor/encoder operating speed does not correspond to resonant structural frequencies. A stress/strain analysis was not performed due to the use of the 80/20

structural beam fabrication system, which was overly strong for this application, and due to the short design timeline. Interface modeling between the telescope and structure using spring and damper elements could be an extension of this work. This analysis focused strictly on the structure and not how vibrations transmitted through the interface to the telescope would effect the optical properties. A greater depth of analysis could be performed in the future to optimize the structure and system.

3.2 Structural Modeling

Two main concepts were explored for the ground-based CTE_x structure design. The first concept was mounting all experimental equipment along the length of a central beam. The second concept was to create essentially a table top and mount all experimental equipment to the top of the table. Each concept was simple, easily mountable to a tripod and could be manufactured with 80/20 components as well as some other materials and fasteners (80/20 is a brand name for a structural beam fabrication system).

FEMAP/NASTRAN was used to model each of the two conceptual structures for the ground instrument design. Beam elements were primarily used for modeling and analysis because the beam models are less complex and faster to create. However, the beam models did incorporate some plate and solid elements. For the 80/20 beam cross-sections and material properties, these could easily be imported from the 80/20 website [49] and modeled in FEMAP/NASTRAN.

3.2.1 Design Iteration One. The first design concept considered was mounting all the components to a central beam. Figure 3.1 represents the beam model of the structure in FEMAP with the 90 degree attachment plates and telescope modeled as plate structures. Point masses for the encoder, camera and telescope were used to as accurately as possible represent the actual component masses in the real structure. The beams consisted of 1515 cross section 80/20 beams. A 1515 cross section refers to 1.5 inch x 1.5 inch 80/20 cross section.

To evaluate the structure's dynamic response, an eigenvalue analysis was performed in FEMAP/NASTRAN. Since the maximum encoder speed was expected to be 25 Hz,

Table 3.1: Eigenvalue Analysis of the Design Shown in Figure 3.1

Mode Number	Frequency
1	7.5 Hz
2	7.6 Hz
3	19.5 Hz
4	27.2 Hz
5	40.3 Hz
6	52.9 Hz
7	58.7 Hz
8	66.2 Hz
9	118.4 Hz
10	126.6 Hz

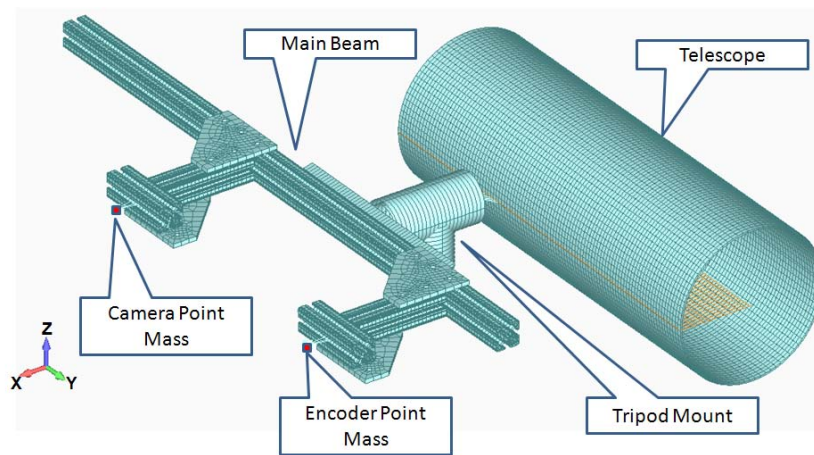


Figure 3.1: FEMAP Model of Single Main Beam Structure

it was desired to have all modes above 100 Hz to allow for a safety factor, since models do not directly translate to reality due to approximations, assumptions and modeling error. The results of this analysis shown in Table 3.1 revealed that eight of the first ten structural modes for this design were below the desired 100 Hz level.

Based on the results of the eigenvalue analysis, it was concluded that the single beam structure as modeled would not be stiff enough. The options to stiffen the structure included either increasing the cross section of the central beam, connecting the structure out of plane, or both. At this point, the decision was made to discard the central beam concept as unfeasible because the modifications were judged to be impractical and evaluate the second conceptual design for suitability.

3.2.2 *Design Iteration Two.* For the second design concept, the exact optical component spacing was provided from a thesis in progress [18], unlike the first design concept where the spacing was estimated from the existing lab apparatus. Figure 3.2 below contains a conceptual diagram of the optical layout that was provided. In addition, the exact focal point of the Vixen telescope was obtained from an optical diagram provided by Vixen Optics [50]. With both of these parameters, the exact positions of the components could be modeled. At a minimum, the design would include at least an inch of adjustment in the telescope position to allow for final adjustments. To simplify the FE model, the lenses and turning mirror were not included, since their combined mass would be low, when compared to the structure and other components.

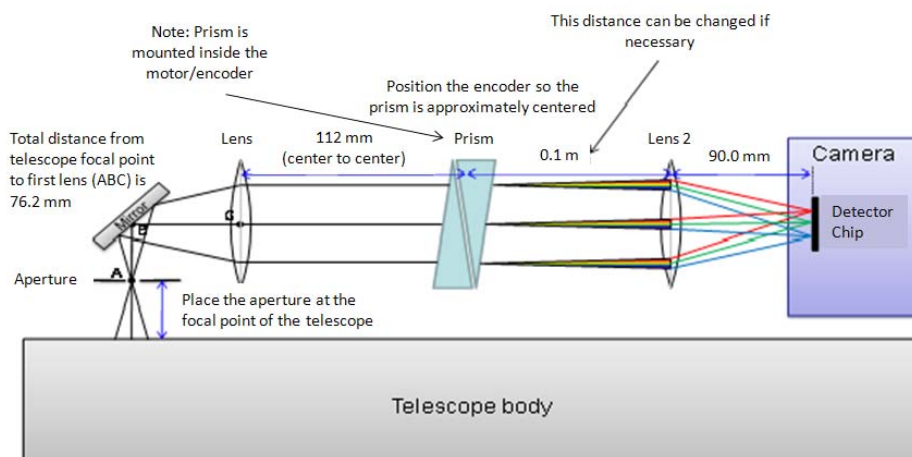


Figure 3.2: Conceptual Optical Component Placement Diagram [18]

The second concept to be evaluated was the equivalent of a modified table top with all components for the ground-based CTE_x attached to that. The conceptual design utilized 1515 and 1530 cross section 80/20 frame with a Thorlab's threaded aluminum breadboard for attaching all optical components. A 1530 cross section refers to 1.5 inch x 3.0 inch 80/20 cross section. The Vixen telescope would be attached to the structural frame itself, rather than through the breadboard to lessen the cost of the breadboard for construction. The breadboard would be utilized for mounting the motor/encoder, camera

and other optical components with the exception of the telescope. The camera and motor/encoder along with estimated mounts were represented by point masses. Linear 80/20 slides were modeled to allow for adjustment of the telescope body along the one axis. Figure 3.3 shows a beam model of this structure with the beam cross sections displayed.

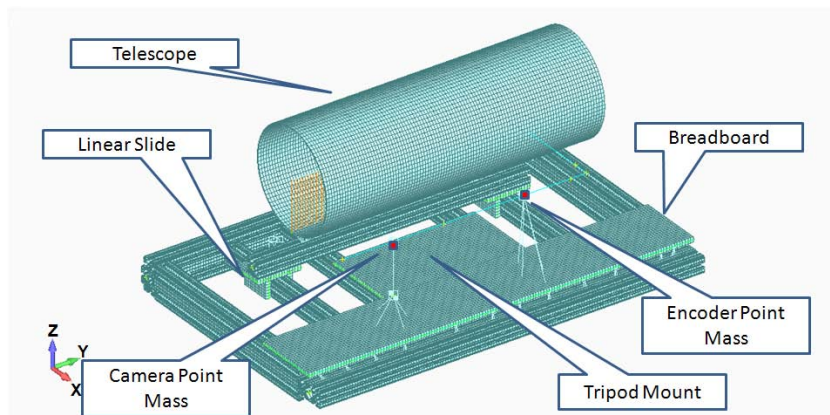


Figure 3.3: FEMAP Beam Model of Original Structural Design

Another eigenvalue analysis was conducted in NASTRAN with the results contained in Table 3.2. This analysis revealed that the structure had 4 modes under 100 Hz. This was fewer than the model in Subsection 3.2.1, but showed that the structure still required additional rigidity in order to meet the mode requirement of greater than 100 Hz.

To stiffen the structure, the deformation of the modes had to be observed in the model. The mode shapes for the first four modes that were less than 100 Hz are displayed in Figure 3.4 to 3.7 and summarized in Table 3.3. The deformation observed in these four modes occurred on the telescope side of the structure.

Table 3.2: Eigenvalue Analysis of the Design Shown in Figure 3.3

Mode Number	Frequency
1	28.56 Hz
2	59.48 Hz
3	61.31 Hz
4	91.22 Hz
5	118.95 Hz
6	135.41 Hz
7	156.98 Hz
8	171.09 Hz
9	177.60 Hz
10	195.87 Hz

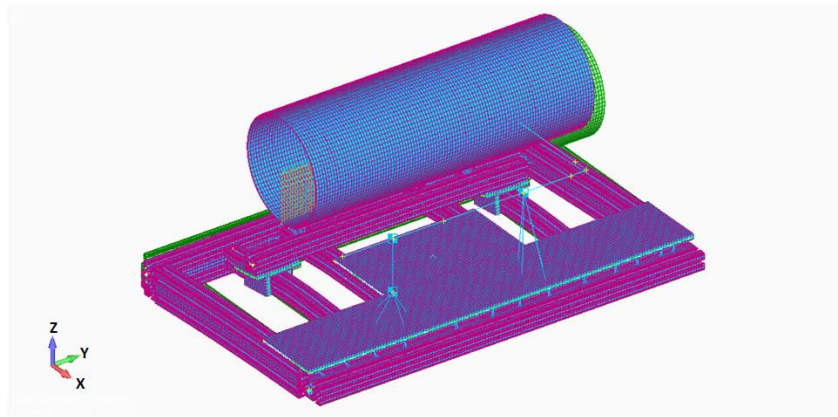


Figure 3.4: First Mode (28.56 Hz) for Model in Figure 3.3, Rocking about X-Axis, Green is Undeformed

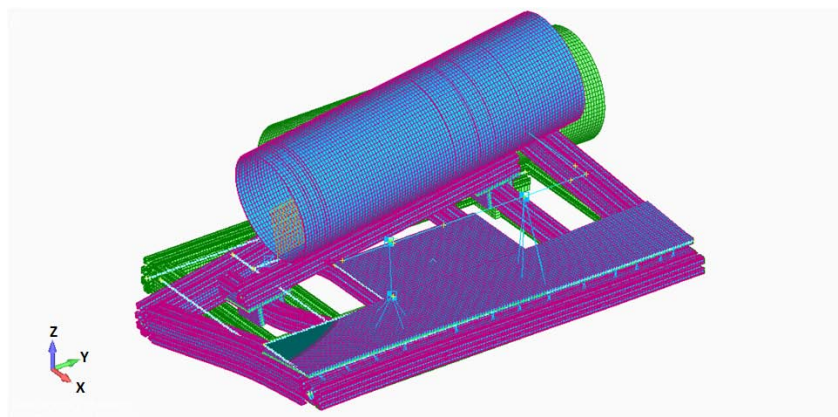


Figure 3.5: Second Mode (59.48 Hz) for Model in Figure 3.3, Rocking about X-Axis, Green is Undeformed

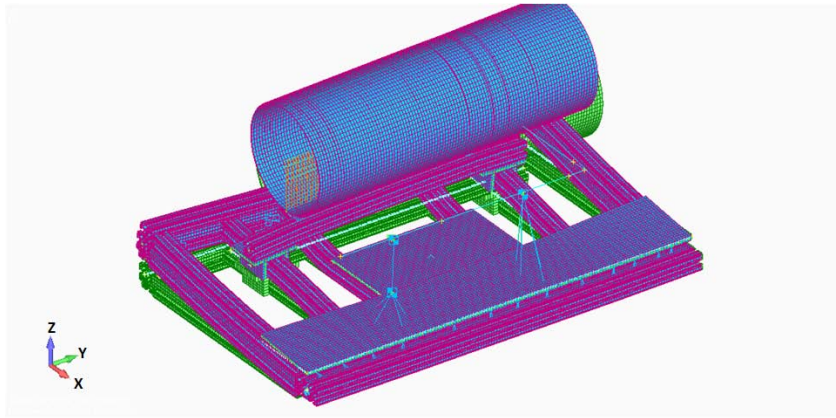


Figure 3.6: Third Mode (61.31 Hz) for Model in Figure 3.3, Rocking about Y-Axis, Green is Undeformed

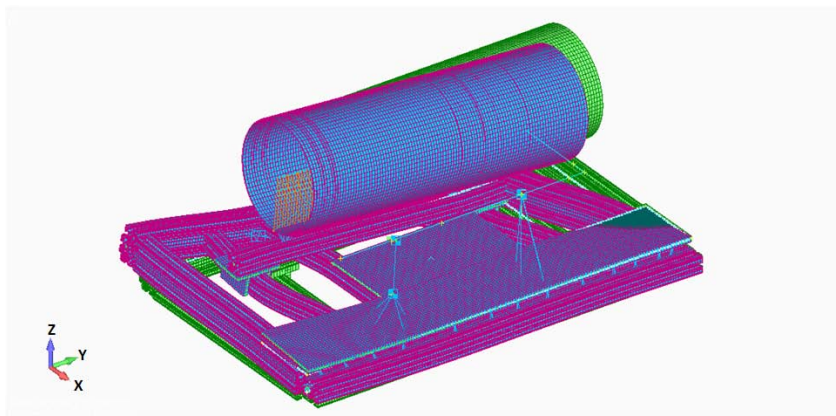


Figure 3.7: Forth Mode (91.22 Hz) for Model in Figure 3.3, Rocking about X-Axis, Green is Undeformed

Table 3.3: Mode Shape Summary for the Design Shown in Figure 3.4 to 3.7

Mode Number	Figure Number	Mode Description
1	3.4	Rocking about X-Axis
2	3.5	Rocking about X-Axis
3	3.6	Rocking about Y-Axis
4	3.7	Rocking about X-Axis

3.2.3 Design Iteration Three. Based on these four modes, the structure was experiencing deformations in numerous directions on the telescope side meaning that the other side was stiffer. To stiffen the telescope side, a box structure was considered. The added box structure was modeled out of 1515 - 80/20 beams, which proved insufficient. Additional diagonal reinforcement was added to increase rigidity, with rigid links used to simulate 80/20 beams for analysis as shown in Figure 3.8.

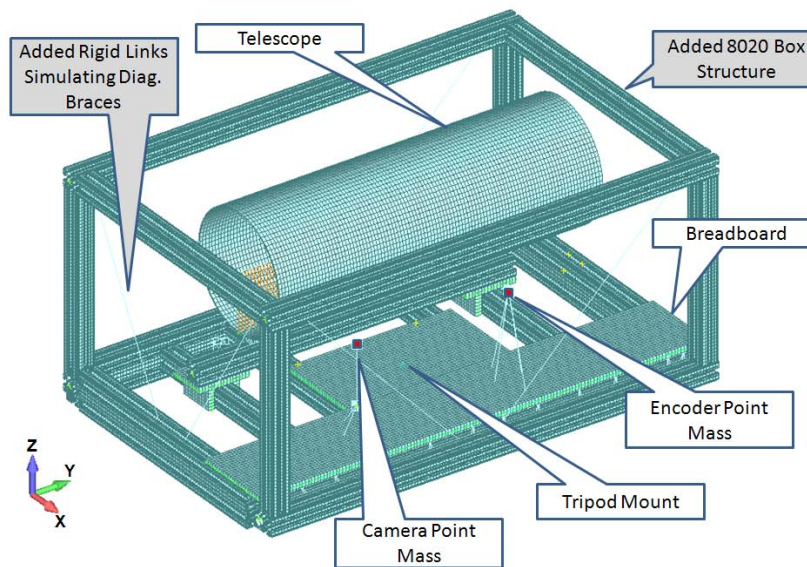


Figure 3.8: Original Structure Modified with Box Structure

Table 3.4: Eigenvalue Analysis of the Design Shown in Figure 3.8

Mode Number	Frequency
1	29.14 Hz
2	50.57 Hz
3	56.11 Hz
4	80.32 Hz
5	87.19 Hz
6	100.28 Hz
7	102.42 Hz
8	103.29 Hz
9	114.04 Hz
10	127.59 Hz

The eigenvalue analysis in Table 3.4 for the box structure revealed that it was still inadequate. Worse than the previous design, five of the structural modes were below 100 Hz. Examining the five mode shapes for these frequencies in Figure 3.9 to 3.13, it was seen that most of the deformation occurred in the telescope side of the structure once again. Table 3.5 presents a summary of the mode motions. Even with modeling the diagonal supports as rigid links, the modes in an actual structural model with 80/20 diagonal braces were lower because of the additional mass added. The conclusion was reached that the additional rigidity added by a box structure did not offset the increase in mass that it would cause. Another structural approach was required.

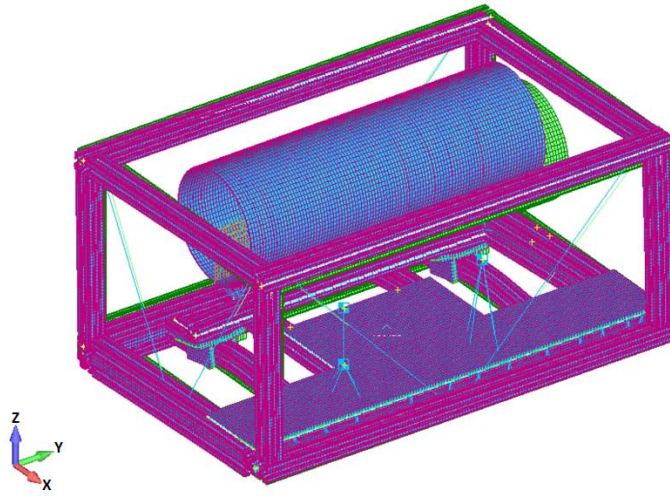


Figure 3.9: First Mode (29.14 Hz) for Model in Figure 3.8, Rocking about Y-Axis, Green is Undeformed

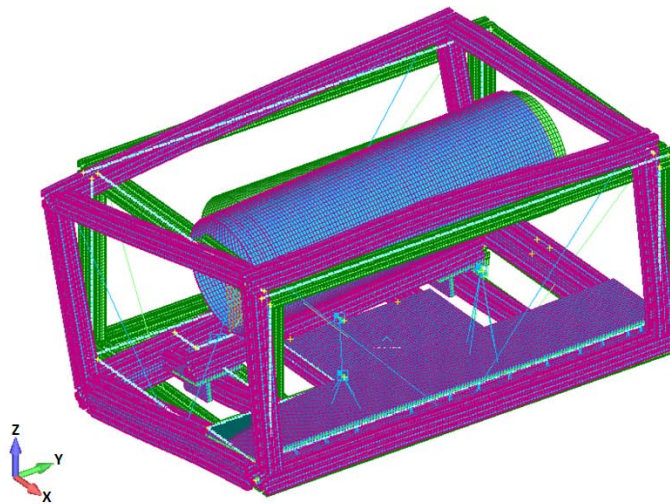


Figure 3.10: Second Mode (50.57 Hz) for Model in Figure 3.8, Rocking about X-Axis, Green is Undeformed

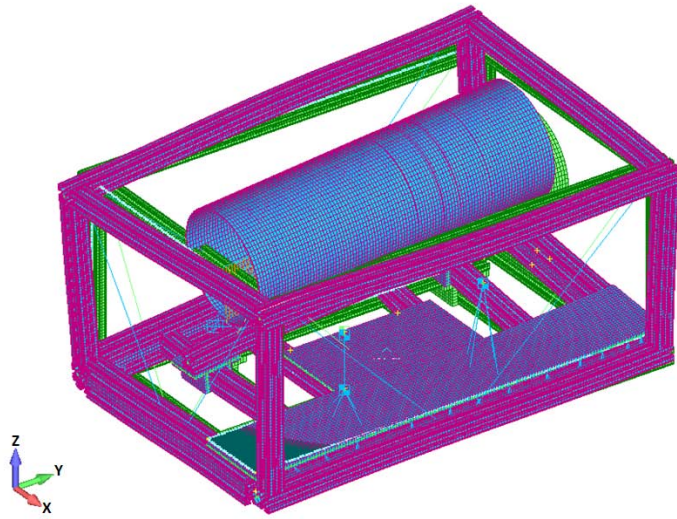


Figure 3.11: Third Mode (56.11 Hz) for Model in Figure 3.8, Rocking about X-Axis, Green is Undeformed

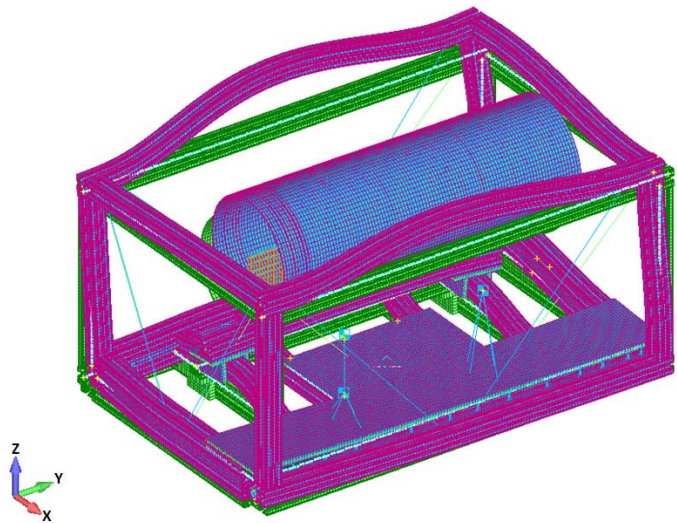


Figure 3.12: Forth Mode (80.32 Hz) for Model in Figure 3.8, Rocking about Y-Axis, Green is Undeformed

Table 3.5: Mode Shape Summary for the Design Shown in Figure 3.9 to 3.13

Mode Number	Figure Number	Mode Description
1	3.9	Bending about Y-Axis
2	3.10	Rocking about X-Axis
3	3.11	Rocking about X-Axis
4	3.12	Bending about Y-Axis
5	3.13	Rocking about X-Axis

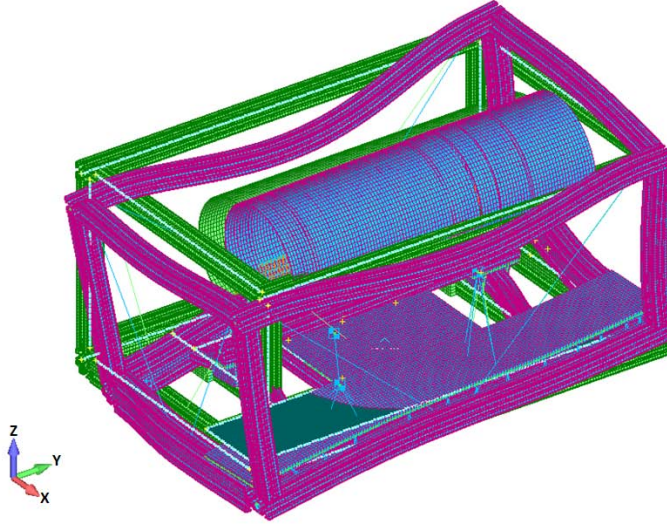


Figure 3.13: Fifth Mode (87.19 Hz) for Model in Figure 3.8, Rocking about X-Axis, Green is Undeformed

3.2.4 Motor/Encoder Mount Design. Prior to another structural modeling iteration, a motor/encoder mount had to be designed. The motor/encoder mount attaches the motor/encoder to the structure so the prism is in the optical path. By designing the encoder mount, it could be more accurately represented in the structural model, rather than as a point mass. The motor/encoder mount also need to be designed for the ground apparatus. The motor/encoder was modeled using solid elements of 2024 aluminum as shown in Figure 3.14 and attached to the breadboard by rigid links at the likely bolt locations. The actual motor/encoder within the mount was still modeled as a point mass.

The motor/encoder mount was designed to be milled out of a solid block of aluminum. This was done to ensure square surfaces. The mount would connect directly to

the breadboard using 0.25 inch bolt holes with one inch centers. A center hole was left in the mount to fit the motor/encoder and holes were tapped around that for mounting. For simplification, the bolt holes were not included in the models.

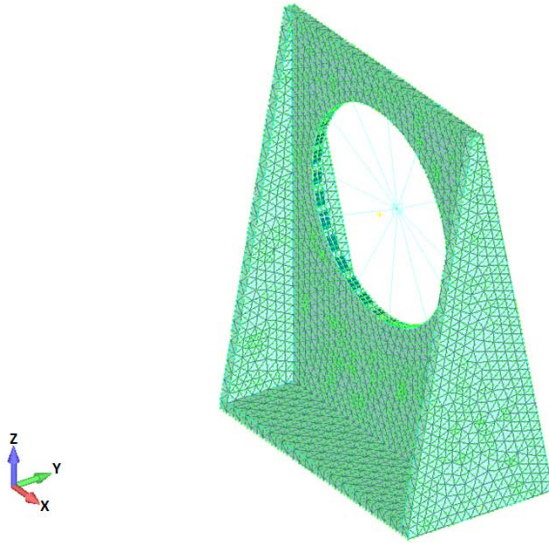


Figure 3.14: FEMAP Encoder Mount Model

3.2.5 Design Iteration Four. To determine the next structural design for modeling, the previous models were studied. In each model, the deformation observed at low frequencies always involved the telescope side of the structure. This led to the conclusion that the telescope had to be connected out of plane to increase the low frequency structural modes. By pinpointing a specific part of the structure to strengthen, rigidity could be increased without suffering a mass penalty as was the case of the box structure in Subsection 3.2.3. To add rigidity to the structure, the telescope was connected out of plane on top using the additional structure shown in Figure 3.15. For this structure, the encoder mount was also included in the model.

The eigenvalue analysis of the model in Figure 3.15 revealed that all structural modes were above 100 Hz as shown in Table 3.6. The lowest observed mode was 127.35 Hz confirming the earlier conclusion that connecting the telescope out of plane was necessary to stiffen the structure. The only drawback to this method was that by connecting the telescope at the top, it raised the center of gravity of the structure. A high center of gravity would have an inverse effect on the tilt mechanism of the mounting tripod by

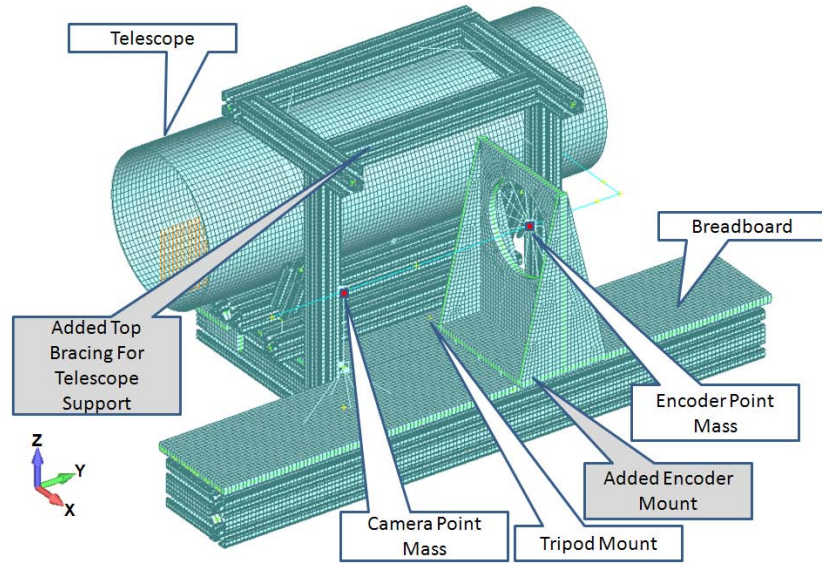


Figure 3.15: FEMAP Model with Telescope Connected at Top

increasing the moment exerted on the tripod tilt lock, which had a capacity of 50 ft-lbs. Eq. (3.1) was used to calculate the maximum tripod moment M that occurs at the highest tilt of 90 degrees

$$M = \left[\frac{H + 3.00}{12} \right] * w \quad (3.1)$$

where H is the height in inches of the center of mass above the tripod mating surface and w is the structural weight. The 3.00 value between the tripod mounting face and the tripod mounting pivot. The highest calculated moment that the structure in Figure 3.15 would produce on the tripod tilt lock at 90 degrees tilt is 48.86 ft-lbs as shown in Eq. (3.2). The values for H and w were taken directly from the FEMAP model.

$$M = \left[\frac{4.0180 + 3.00}{12} \right] * 83.54 = 48.86 \text{ ft} - \text{lbs} \quad (3.2)$$

Table 3.6: Eigenvalue Analysis of the Design Shown in Figure 3.15

Mode Number	Frequency
1	127.35 Hz
2	139.54 Hz
3	155.45 Hz
4	201.47 Hz
5	249.06 Hz
6	251.19 Hz
7	257.65 Hz
8	289.40 Hz
9	330.58 Hz
10	366.77 Hz

However, the moment calculation Eq. (3.2) does not include an estimated connector (bolts, attachment plates, etc) weight of 8 lbs and if this is figured in as in Eq. (3.3), it would produce a moment of 53.54 ft-lbs, thus exceeding the limits on the tripod at the maximum tilt. The model meets the structural frequency requirements, but the structure’s overall mass needs to be decreased or the center of gravity needs to be lowered.

$$M = \left[\frac{4.0180 + 3.00}{12} \right] * 91.54 = 53.54 \text{ ft} - \text{lbs} \quad (3.3)$$

3.2.6 Design Iteration Five. Another method considered for stiffening the telescope mount was connecting it out of plane at the sides to keep the center of gravity of the structure low, as in Figure 3.16. For the model in Figure 3.16, the breadboard was cut in accordance with a new requirement to be able to remove the camera/encoder assembly and place these component pieces on another laboratory setup for development and adjustment prior to mating it back to the tripod mounting structure. The 80/20 linear slide assemblies were also removed from this model to more securely attach the telescope to the structure.

The eigenvalue analysis for the structure with the telescope connected out of plane on the sides revealed two structural modes below 100 Hz as shown in Table 3.7. Examining both of these structural mode shapes in Figure 3.17 and 3.18 revealed that the deformations occurred in the telescope supports. The summary of the modes is located in Table 3.8. It was concluded that the four telescope 80/20 structural members were

Table 3.7: Eigenvalue Analysis of the Design Shown in Figure 3.16

Mode Number	Frequency
1	71.20 Hz
2	92.02 Hz
3	147.98 Hz
4	150.79 Hz
5	163.58 Hz
6	182.74 Hz
7	184.90 Hz
8	195.25 Hz
9	242.55 Hz
10	264.75 Hz

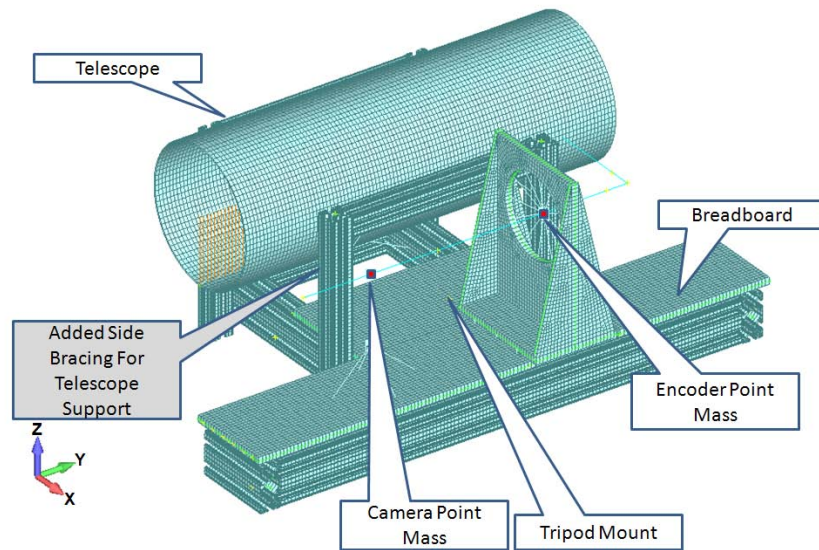


Figure 3.16: FEMAP Model with Telescope Side Mounted

not rigid enough. To increase the rigidity, two 0.125" thick 2040 aluminum plates were applied as in Figure 3.19 to increase the rigidity and the eigenvalue analysis was ran again.

Table 3.8: Mode Shape Summary for the Design Shown in Figure 3.17 to 3.18

Mode Number	Figure Number	Mode Description
1	3.17	Rocking about Y-Axis
2	3.18	Rocking about Y-Axis

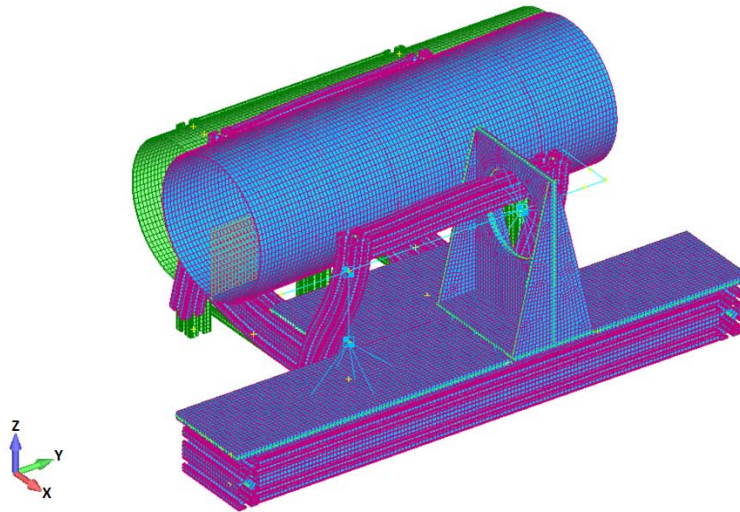


Figure 3.17: First Mode (71.20 Hz) for Model in Figure 3.16, Rocking about Y-Axis, Green is Undeformed

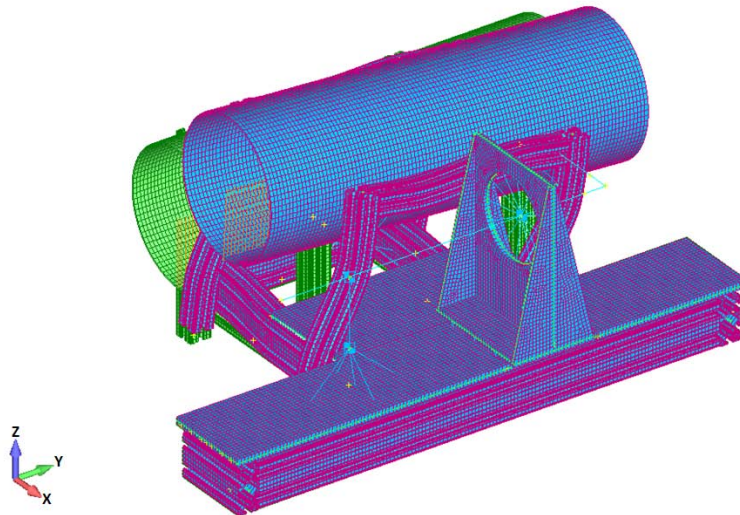


Figure 3.18: Second Mode (92.02 Hz) for Model in Figure 3.16, Rocking about Y-Axis, Green is Undeformed

Table 3.9: Eigenvalue Analysis of the Design Shown in Figure 3.19

Mode Number	Frequency
1	110.06 Hz
2	115.68 Hz
3	151.17 Hz
4	163.69 Hz
5	184.60 Hz
6	194.70 Hz
7	243.28 Hz
8	264.69 Hz
9	275.01 Hz
10	325.53 Hz

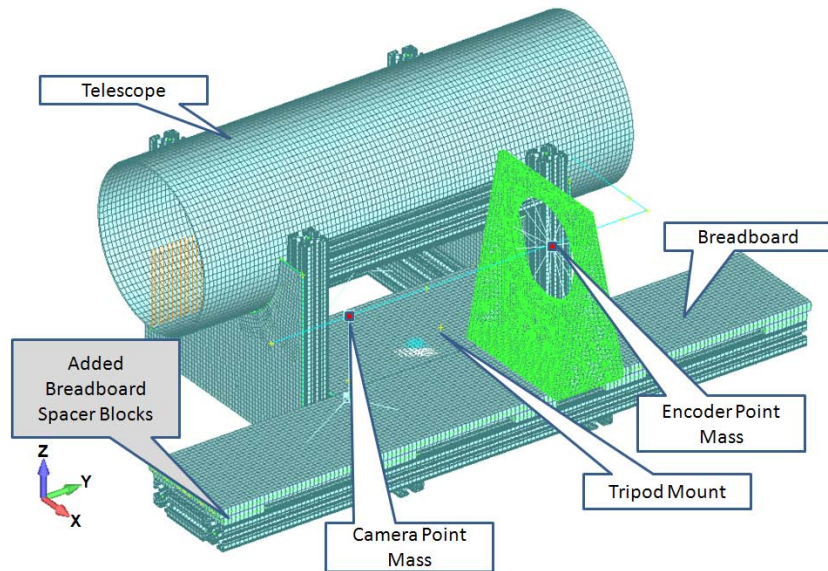


Figure 3.19: FEMAP Model with Telescope Side Mounted Including Reinforcement Plates

Looking at the eigenvalue analysis in Table 3.9 for the model in Figure 3.19 revealed that all modes were above 100 Hz. This model met the required structural mode design specifications. It has a total weight of 84.55 lbs and center of mass located 3.51328 inches above the tripod mating surface. As calculated in Eq. (3.4), this resulted in a maximum tripod tilt moment of 45.34 ft-lbs.

$$M = \left[\frac{3.5133 + 3.00}{12} \right] * 84.55 = 45.34 \text{ ft} - \text{lbs} \quad (3.4)$$

Adding an estimate connector (screws, attachment plates, etc) weight of 8 lbs, Eq. (3.5) reveals a maximum tripod moment of 50.22 ft-lbs, which is just slightly outside the tripod limit of 50 ft-lbs. [48]

$$M = \left[\frac{3.5133 + 3.00}{12} \right] * 92.55 = 50.22 \text{ ft} - \text{lbs} \quad (3.5)$$

Although this is close to the tripod tilt limit, a couple of things need to be considered. The likelihood of the tripod ever being tilted to its maximum moment at 90 degrees is likely zero, because it would be looking at the ground. A minor weight reduction would be far easier for the model in Subsection 3.2.6 because its center of gravity is lower than the model in Subsection 3.2.5. The model in Subsection 3.2.6 was selected for refinement and final design.

3.3 Results

The model in Subsection 3.2.6 was selected for final design. A more detailed analysis model is shown in Figure 3.20. In this model, the connecting rigid links were primarily redefined. This included adding the stainless steel spacer blocks located under the breadboard to develop the proper number of spacers and attachment points for final structural design. This model had the dimensions of some beam elements reduced from a 1530 cross-section to a 1515 cross-section in order to decrease mass.

Figure 3.21 provides a synopsis of the materials and elements used in the model in Figure 3.20. The beam elements are all 1515 cross-sections with the exception of the two main telescope support beams and the two side tripod pocket beams, which utilized a 1530 cross-section. The telescope end panels are 1/8" 2040 aluminum plates. The tripod head plate was constructed out of 1/4" 303 stainless steel. The breadboard spacer blocks were 1/2" 303 stainless steel blocks. Although stainless steel was heavier for these two applications, it was chosen over top of aluminum to allow for better threading. The breadboard was from Thorlabs and built of 6061 aluminum. The encoder mount was built from a block of 2024 aluminum.

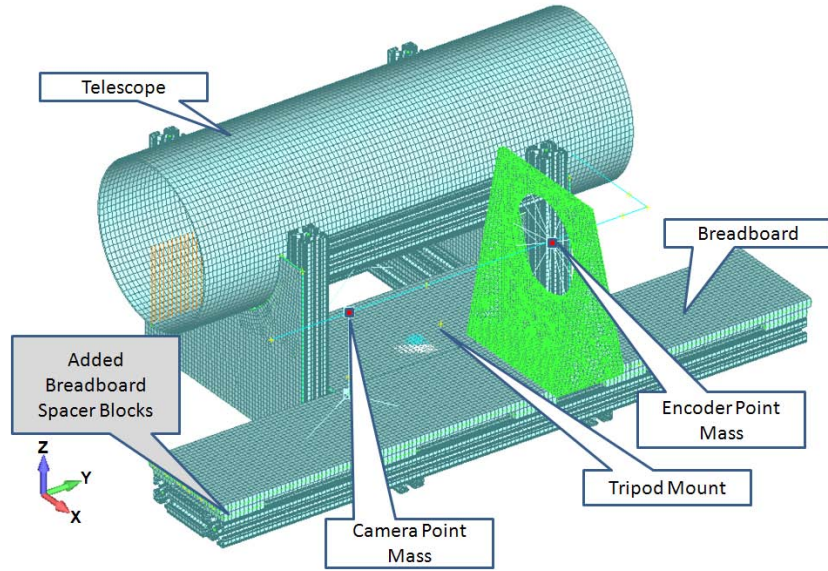


Figure 3.20: FEMAP Model with Telescope Side Mounted Including Plates and Spacer Blocks

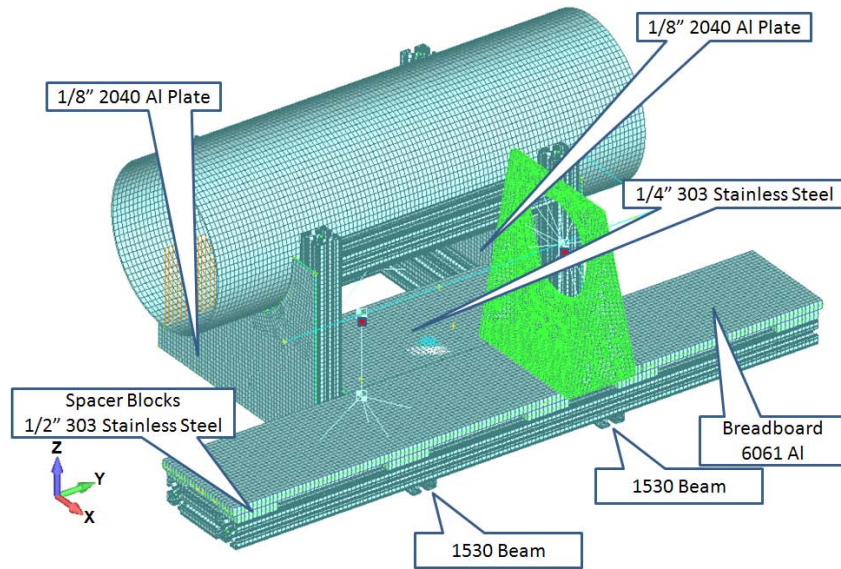


Figure 3.21: Materials for Figure 3.20 model

Table 3.10: Eigenvalue Analysis of the Design Shown in Figure 3.20

Mode Number	Frequency
1	112.63 Hz
2	115.02 Hz
3	115.80 Hz
4	116.65 Hz
5	125.74 Hz
6	142.07 Hz
7	178.15 Hz
8	193.31 Hz
9	194.83 Hz
10	249.31 Hz

The eigenvalue analysis in Table 3.10 for the FEMAP model in Figure 3.20 revealed that it still met specifications following these minor alterations. There was only a slight drop in mode frequencies, which was expected due to the increase in mass from the breadboard spacer blocks. It should be noted that the model does not include some mass elements such as bolts, connector plates, nuts and washers. Table 3.11 outlines the model estimated weight, the researcher's estimated weight by including bolts, connector plates, nuts, and washer weights. This means that a drop in modal frequencies could be expected between the model and an actual constructed structure, but with the high safety margin of 100 Hz in the model and the actual excitation source at 25 Hz or less, the mass increases should not affect the performance.

When evaluating the model results contained in this chapter, it is important for the reader to understand the limitations of the modeling analysis. The FEA method using FEMAP/NASTRAN is not an exact solution, but an approximate solution, which is subject to modeling assumptions and limitations. For the modeling process, a couple of assumptions had to be made to linearize the problem: [51]

- Material properties - constant, homogeneous, and isotropic
- Assume linear response
- Everything is assumed to be steady state
- Small displacements and rotations

- Fixed loads and boundary conditions

For the models in Section 3.2 of this report, it is important to note possible sources of error, so that limitations of the analysis are understood by a reader. The following are possible limitations of the analysis: [51]

- Mesh density and element type - 0.25” elements were used throughout most of the models for simplicity. The effect of different discretization sizes was not examined, nor were different types of elements due to time constraints
- Numerical error - Internal to NASTRAN (rounding error, neglecting higher order terms)
- Assumptions - Validity of earlier assumptions
- Simplification of structure - Neglecting connectors and fasteners, modeling of breadboard as a solid plate without holes
- Mass distribution - Point masses used to represent camera, encoder, and additional telescope mass do not accurately represent component mass distributions.
- Boundary conditions - simplified mating of structure to tripod head plate as a couple of point boundary conditions.
- Connections - Represented approximately with rigid links, which may not be close to reality without experimental testing.
- Tripod - Not modeled as part of structure, which could change the dynamics of the structure.

The connections in the beam models were initially concluded to represent the largest portion of possible error. This was because the connections between materials were simulated with rigid links and due to the fact that they were beam models, connections can cause some unrealistic torsional motions if care is not taken. The accuracy of the connections could have been improved prior to modeling by experimental testing of different types of connections then re-creating these connections back in FEMAP using optimization. However given the short design timeline for the structure, it was assumed

that most actual connections would provide more stiffness in the actual structure than in the modeled one because of surface contact interfaces between the parts.

A second area of possible error was the simplification of the breadboard as a solid plate structure without any holes. An adjustment was made to the material density by lowering it to reflect the actual mass of the breadboard, but the modulus of elasticity was not lowered to account for the decreased rigidity that the holes cause in the real breadboard. The reason for not lowering the modulus of elasticity was the lack of information on an approximate value, and the lack of time to experimentally obtain a reasonable approximation.

The above mentioned limitations are standard, well-accepted simplifications. If these simplifications were not used; the models would become very complicated. The complications would render the models infeasible for inclusion as a design tool. By utilizing these well accepted simplifications, the models are useful approximations that contribute to the design process.

Given the modeling limitations, the model in this section meets all design specifications cited in Section 3.1 of this report, and the decision was made to construct it. The design was capable of mounting all components, including a breadboard interface, which is a common interface for most optical experiments. Given the final calculated weight in Table 3.11, the structure is portable using a two man carry. All modeled structural modes are above 100 Hz, and the fabricated modes with confidence were above the 25 Hz motor/encoder excitation range. The structure had a maximum tilt moment of 45.52 ft-lbs, as shown in Eq. (3.6), within the 50 ft-lbs capacity of the tripod tilt lock. 80/20 fabrication was used for the construction. 3.19911 inches and 88.13 lbs were obtained from the latest FEMAP model with the addition of the estimated eight lbs connector weight.

$$M = \left[\frac{3.1991 + 3.00}{12} \right] * 88.13 = 45.52 \text{ ft} - \text{lbs} \quad (3.6)$$

The final structure was produced from the model pictured in Figure 3.20. Separate IGES files were exported of each part and given to the AFIT model shop along with

Table 3.11: Mass and CG Expected Values for the Model in Figure 3.20

Expected Measurement	Value
FE Weight	80.130 lbs
FE Weight + Est Connector Weight	88.130 lbs
FE CG - X Dir	1.280 inches
FE CG - Y Dir	-0.882 inches
FE CG - Z Dir	3.199 inches

all materials for production. The modeling approach utilized allowed a design to be successfully produced in a short period of time.

IV. Telescope Design Review

The design and fabrication of the off-axis Mersenne telescope was contracted out from the Air Force Institute of Technology (AFIT) to RC Optical Systems (RCOS) of Flagstaff, Arizona, based on a bid and previous optical design experience. Most of the company's design experience is in the fabrication of ground-based astronomical and specialized telescope designs, but does currently include one space-based telescope design on-orbit for a project that was launched in December 2007 [52].

The contract was awarded to RCOS with the condition that AFIT approve the engineering drawings prior to fabrication in order to ensure the telescope design meets the requirements for the CTE_x project. The initial requirements that were contained in the contract are included in Appendix C. These requirements specified that the telescope was to be an off-axis Mersenne telescope in order to meet the space requirements, and included optical performance requirements. However, since CTE_x is an on-going project, additional requirements have surfaced that also must be verified. The purpose of this part of the thesis was to conduct the design review of the engineering drawings and recommend acceptance of those drawings and/or suggest modifications to RCOS.

The design review was a critical step in the process to allow AFIT the chance to review the design and evaluate its likelihood of successfully operating and surviving in the harsh launch and space environments. For launch, the telescope will be subjected to high acceleration and vibration levels that could cause alignment issues in the telescope if everything is not properly secured and fastened. The space environment will subject the telescope to thermal cycling that can degrade optical quality and alignment. The design review also allows the design to be evaluated for its ability to meet space qualifications, such as the use of proper materials, wiring, etc; evaluate the telescope's interfaces as they pertain to the rest of the experiment, such as size, electronics, etc; and ability to meet mission requirements, such as tracking an Earth-based target from orbit.

4.1 Methodology for Defining Verification Requirements

The methodology for the creation of approval requirements was to develop a verification measures document as a starting point, which is contained in Appendix B. The

basis for the requirements verification document was the initial contract in Appendix C along with any changes negotiated during the development process. Changes to the contract requirements that came about as part of the design process are highlighted in red. The most critical changes were the slow dwell mirror is now two axis instead of one to allow it to follow an Earth-based target, the collimated beam is now two inches in diameter instead of one to enable a larger prism size, and AFIT is responsible for fabricating the baffling, enclosure, and field stop based on RCOS design specifications. The dwell mirror was originally specified as one axis, but after further evaluation, it was determined that two axis slewing was required to increase the chances of locating and tracking an Earth-based target. Increasing the collimated beam diameter to two inches instead of one inch allows a larger prism to be used, simplifying the prism and mount design. The trade-off for changing the original specifications was that AFIT is responsible for fabricating the baffling, enclosure and field stop in lieu of rebidding the contract after changing the dwell mirror to two axis to compensate for the additional cost.

The next step in the contract verification was to develop a method for evaluating whether the contract requirements in Appendix C were being met. Verification measures were developed for each contract requirement. The verification measures were grouped into several subcomponent categories that include optical properties, mechanisms, structural, electronics, and contracting as shown in the verification measures document in Appendix B. Each verification measure is tied on the document back to one or more contract requirements. For each verification measure, a verification method is listed as to what information will be required from the contractor for validation.

At the current level of progress in the acquisition process, not all the requirements can be verified, because some designs are not complete such as the baffling and enclosure. To better specify exactly what would be required from the contractor to approve the design and trigger the initial payment and start of procurement, a teleconference was held 24 November 2009. This meeting included the contractor as well as the input of several faculty members. From the verification measures document and teleconference, a revised verification measures list was submitted to RCOS.

The following is a list of the verification measures submitted to RCOS to approve the design based on the most current and developed space experiment mission plan for CTE_x: [53],

- Items required for approval of the drawings
 - CAD Model
 - Optical Properties - beam description, field of view, magnification, wavelength sensitivities, etc.
 - Ray tracings - wavefront analysis and error budget
 - Stray light analysis
 - Subcomponent specifications/literature wherever possible
- Other requested deliverables by the end of the contract
 - CAD Model - final as built signed drawings
 - FE model
 - Thermal analysis - survival limits, operational limits, and description of limiting factors
 - Test and calibration reports - wavefront error characterization including off-axis
 - Optics mounting scheme - attachment to breadboard and additional devices required to secure for launch
 - Baffling/enclosure design
 - Materials list - space qualified per NASA-STD-6016 [54] - deviations should be noted
 - Mechanisms - range, rate and accuracy. (Evaluation of mechanisms to meet NASA-STD-5017 [55] for COTS)
 - Field stop design - hardware recommendation
- Other items of interest

- How is alignment maintained - what is done to prevent changes? i.e. bonding adjustment screws, etc.
- What are the power requirements for each electrical component - power voltage, current, signal conditionings, etc?
- Shipping - method, estimate date, containment method, and required reassembly and retest at AFIT.

However, given that the enclosure design was not finalized yet, the stray light analysis requirement was dropped until later.

4.2 Requirements Verification

On 08 December 2009, RCOS conducted a teleconference with AFIT for approval of the initial drawings. The members in attendance at AFIT included several faculty and students to review and approve the RCOS design. The following information is a synopsis of what was reviewed.

The first area reviewed was the mechanical platform layout as pictured from the CAD model in Fig 4.1. The current design contains all necessary components as required, including the appropriate area for the primary CTE_x instrument, which is 60 cm x 15 cm. The final evolution of the design has the breadboard oriented vertical to the experiment base with the telescope aperture out the side (nadir pointing), which is a change from the original design that had the breadboard parallel and the telescope aperture looking through a hole in the breadboard. This design evolution eliminates the requirement to put a hole in the breadboard. The overall dimensions of 45.5 cm x 132.5 cm x 70 cm meets the adjusted space requirements for the optical enclosure for the experiment [19].

The main mechanisms that are required for the CTE_x experiment to function according to the mission plan are the dwell mirror, fast steer mirror, linear slide for the field stop and associated controllers. The dwell mirror is included in the design to allow the telescope to track and/or acquire an Earth-based target within +/- 8 degrees of Nadir. The Fast Steering Mirror (FSM) is necessary to reduce jitter due to station vibrations. The two Off-Axis Paraboloid (OAP) mirrors are present to magnify and

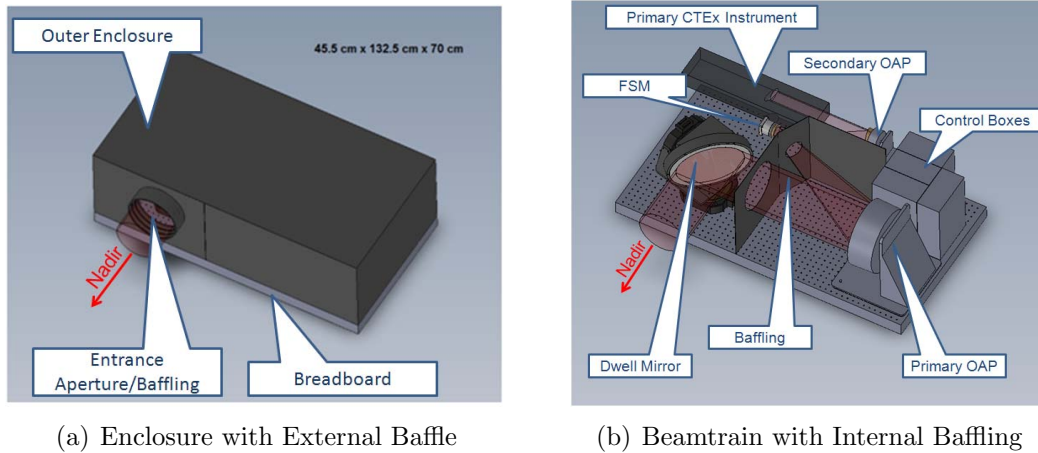


Figure 4.1: RCOS Mechanical Layout for Off-Axis Mersenne Telescope [19]

collimate the collected image. The linear slide for the field stop is not pictured due to obstruction by the baffling, but would be located between the FSM and secondary OAP. Four controllers are pictured, two for the dwell mirror, one for the FSM, and a yet undefined one for the linear slide [19].

The baffling and enclosure shown in Figure 4.1 is intended to prevent any stray light issues. The overall enclosure is designed to keep stray light out of the imager, but it is still possible for off-axis light to enter the imager through the entrance aperture. Two sets of baffling are used to prevent off-axis stray light. The first set of baffling is located protruding from the entrance aperture of the enclosure. The second set of baffling is internal and only lets on-axis light pass between the dwell mirror and the FSM. Together both the enclosure and internal baffling should eliminate any stray light from entering the imager telescope.

Of primary interest was the evaluation of the design's optical performance. The two OAP mirrors are the primary optical elements for the telescope. Figure 4.2 contains the prescription data for the 23 cm primary OAP and 7 cm secondary OAP that yield a 4.65 magnification (ratio between focal lengths of 800 mm and 172 mm) and 0.191 degree half angle field of view. The prescriptions were calculated using the Zemax optical program [19].

	Primary OAP	Secondary OAP
Substrate Material:	Zerodur/ULE or equivalent	
Shape:	Concave Parabola	
Focal Length:	800 mm	172 mm
Off-Axis Distance To Inner Edge:	235 mm, (350 mm to center)	40.246 mm (75.246 mm to center)
Outer Diameter:	230 mm	70 mm
Clear Aperture:	210 mm	62 mm
Edge Thickness:	TBD Per SORL Mount	
Surface Figure:	0.0715 RMS @ 632.8nm (1/4 PV)	
Surface Roughness:	25A RMS	
Optical Coating:	Please quote Protected Aluminum and Protected Silver	

Figure 4.2: RCOS Off-Axis Mersenne Telescope OAP Prescriptions [19]

Figure 4.3 represents the modeled optical performance of the off-axis Mersenne telescope design. The optical layout shows the location of the focus point between the Fast Steering Mirror (FSM) and secondary OAP and that the optical beam is collimated after the secondary OAP. The image simulation is a modeled depiction of an image viewed through the off-axis Mersenne telescope showing that there are no apparent aberrations. The root mean squared (RMS) wavefront error (WFE) versus FOV chart in Figure 4.4 shows that the RMS WFE is within the two times diffraction limit for the entire FOV with the exception of 400 nm at the FOV limits that just barely exceeds this requirement. The diffraction exception at the FOV limits for 400 nm is also shown by the Optical Path Differences (OPD) performed for FOVs of +/- 0.191 degrees showing that the increase in WFE at the outer FOVs is a gradual rather than an abrupt change. However, given that the maximum FOV that will be utilized by CTE_x is 0.05 degrees, the results are acceptable and within diffraction limits. The Modulation Transfer Function (MTF) in Figure 4.5 shows no sharp drop offs as angular frequency is increased for the on-axis FOV (blue) and the off-axis FOVs (Red and Green), which is expected for optimal performance. The Point Spread Function (PSF) shows a large amplitude and very narrow width that is expected for optimal performance. Overall, the optical performance for the proposed design is suitable [19].

Optical Layout

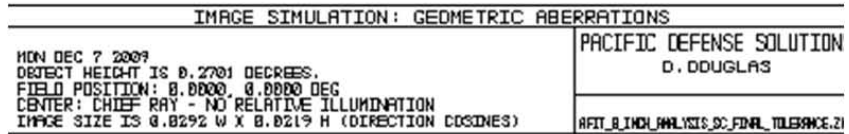
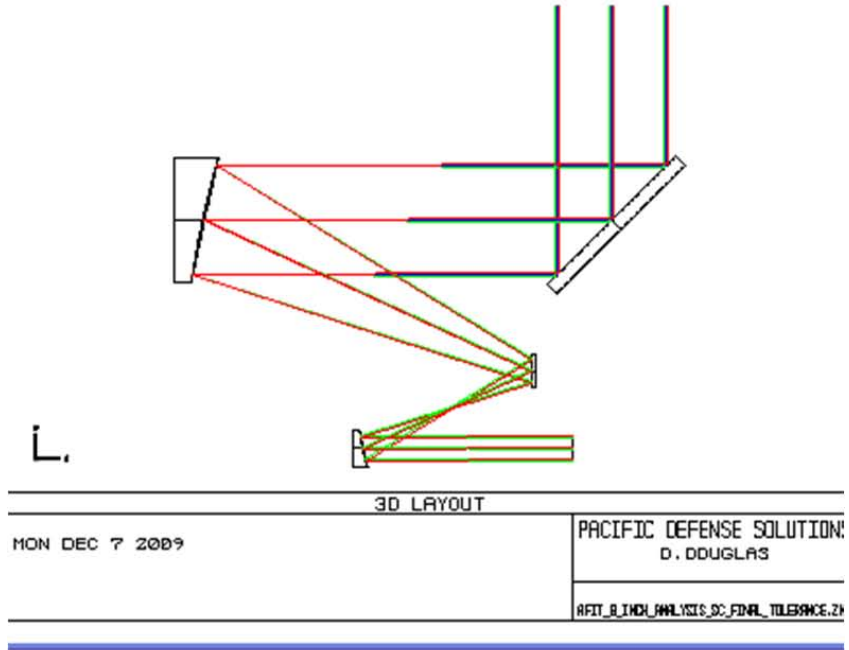


Image Simulation

Figure 4.3: RCOS Optical Layout and Image Simulation [19]

RMS WFE vs. FoV

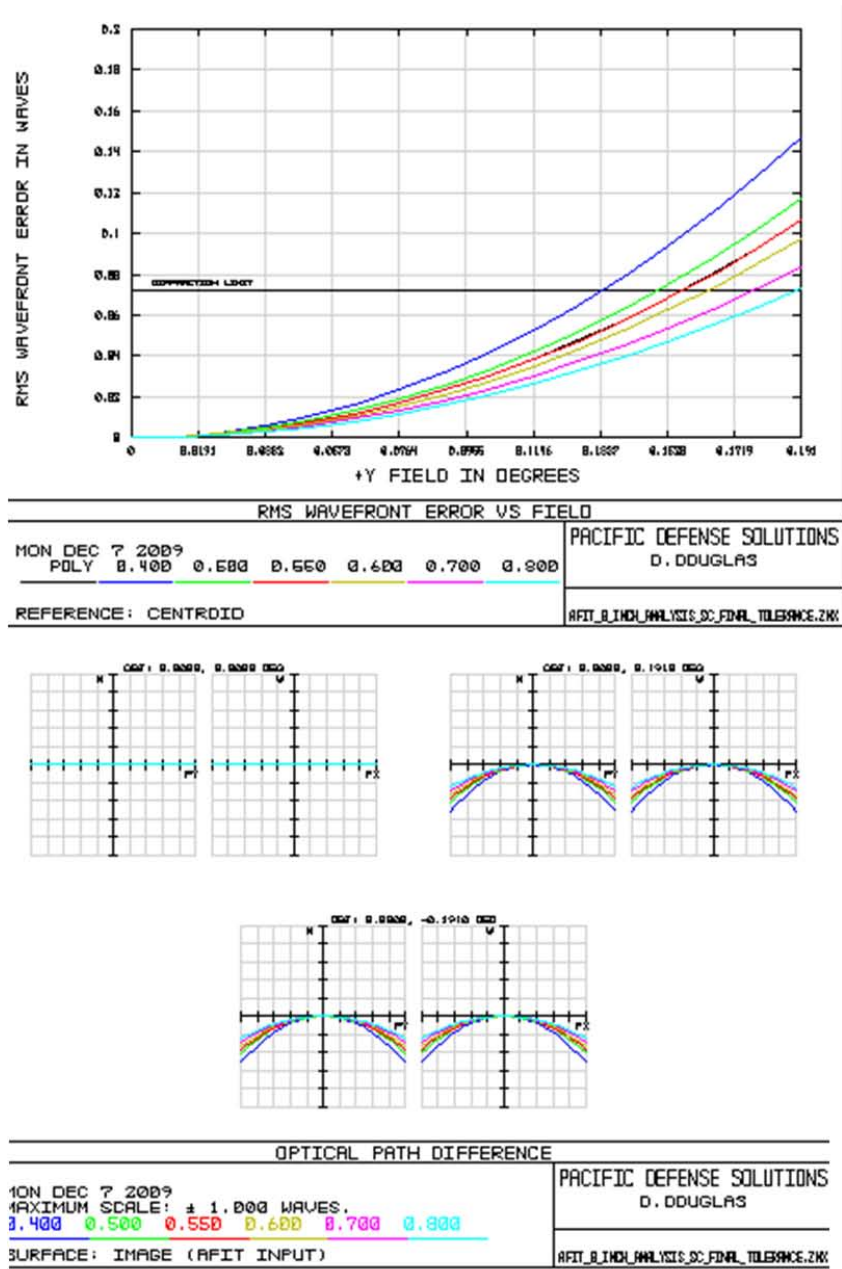
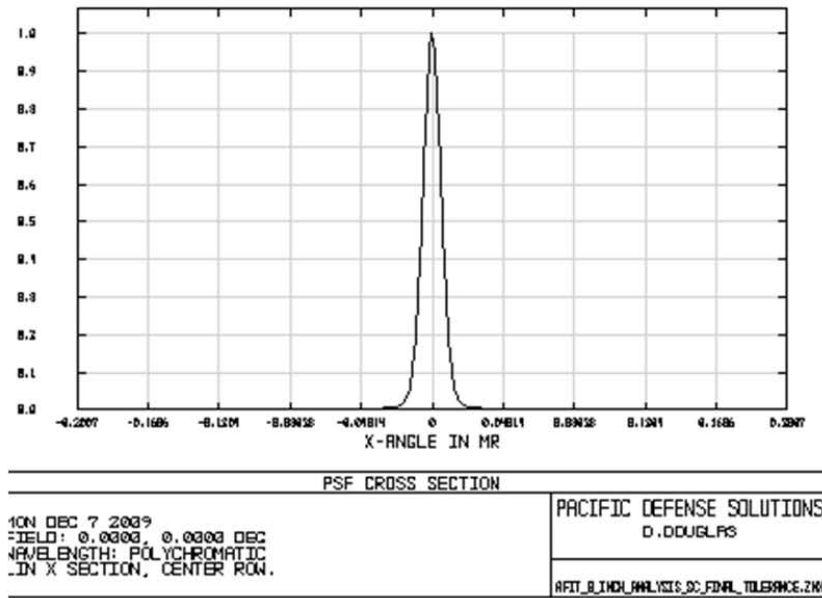
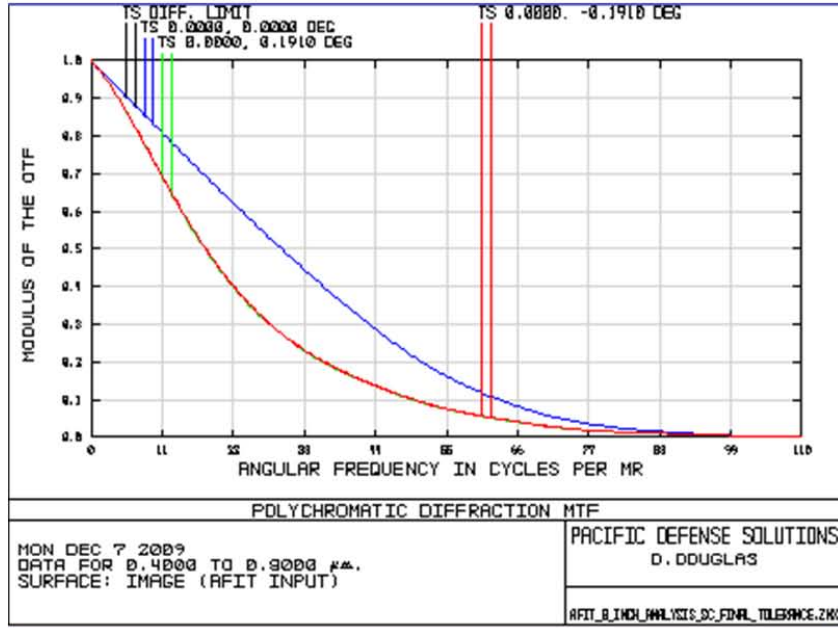


Figure 4.4: RCOS Root Mean Square(RMS) Wavefront Error(WFE) and Optical Path Differences [19]

MTF



PSF

Figure 4.5: RCOS Modulation Transfer Function and Point Spread Function [19]

The ground sampling distance (GSD) for the RCOS off-axis Mersenne telescope design is determined by first calculating the Effective Focal Length f_e in Eq. (4.1),

$$f_e = \frac{f_1 * f_3}{f_2} = \frac{0.800 * 0.150}{0.172} = 0.698 \text{ meters} \quad (4.1)$$

where from the RCOS telescope, $f_1=800$ mm and $f_2=172$ mm, and estimated focal length of the final focusing lens in the CTE_x instrument is $f_3=150$ mm. From the Effective Focal Length, the GSD is calculated in Eq. (4.2)[40],

$$GSD = \frac{pp * range}{f * \sqrt{\sin \theta}} = \frac{20 * 350}{698 * \sqrt{\sin 90}} = 10.0 \text{ meters/pixel} \quad (4.2)$$

where from the contract in Appendix C, $pp=20$ micron and $range=350$ km. The θ was estimated to be 90 degrees for this calculation. A GSD of 10.0 meters/pixel meets the contract requirements.

Figure 4.6 represents the alignment tolerances that would be possible for the off-axis Mersenne telescope with linear distances in mm and angular distances in degrees. The tolerances provided here can be coupled with that of the primary CTE_x instrument to develop an alignment budget for the entire system as discussed in Section 2.4. However, for the purpose here, the concern was with how the proposed system would be able to maintain its optical performance requirements when subjected to minor perturbations in the component alignment from the launch and/or operating environments. Monte Carlo simulations were performed by the contractor using 1000 trails with a test wavelength of 632.8 nm to display alignment confidence levels. Figure 4.7 shows that with greater than 90 percent confidence, the system will maintain its alignment when subjected to perturbations caused by the harsh launch and space environments. The most sensitive optical component in the system shown by this analysis was the alignment of the secondary OAP [19].

Nominal	Min	Max	Comment
-	-	-	Back Focus Compensation
400.000	-2.500	2.500	
-	-	-	
-	-	-	***** Compensators *****
-	0.633	-	- Test Wavelength = 0.6328 microns HeNe
-	-	-	
-	-	-	***** Dwell Mirror Tolerances *****
-45.000	-0.020	0.020	Dwell Mirror Mount X-tilt
0.000	-0.020	0.020	Dwell Mirror Mount Y-Tilt
0.000	-1.582E-005	1.582E-005	Dwell Mirror Surface Figure (1/20) RMS
-800.000	-0.500	0.500	Dwell Mirror to Primary OAP Distance
-	-	-	
-	-	-	***** Primary OAP Tolerances *****
0.000	-0.050	0.050	Primary OAP X-tilt
0.000	-0.050	0.050	Primary OAP Y-Tilt
0.000	-0.100	0.100	Primary OAP X-Decenter
0.000	-0.100	0.100	Primary OAP Y-Decenter
-350.000	-0.050	0.050	Primary Mirror Off Axis Distance
0.000	-0.020	0.020	Primary OAP Clocking
0.000	-6.328E-005	6.328E-005	Primary OAP Surface Figure
650.000	-0.075	0.075	Primary OAP to FSM Distance
-	-	-	
-	-	-	***** FSM Tolerances *****
0.000	-0.020	0.020	FSM X-tilt
0.000	-0.020	0.020	FSM Y-Tilt
0.000	-0.100	0.100	FSM X-Decenter
0.000	-0.100	0.100	FSM Y-Decenter
0.000	-1.583E-005	1.583E-005	FSM Surface Figure
-322.000	-0.075	0.075	FSM to Secondary OAP Distance
-	-	-	
-	-	-	***** Secondary OAP Tolerances *****
0.000	-0.050	0.050	Secondary OAP X-tilt
0.000	0.050	0.050	Secondary OAP Y-Tilt
0.000	-0.075	0.075	Secondary OAP X-Decenter
0.000	-0.075	0.075	Secondary OAP Y-Decenter
0.000	-0.100	0.100	Secondary Mirror Off Axis Distance
0.000	-0.020	0.020	Secondary OAP Clocking
0.000	-6.328E-005	6.328E-005	Secondary OAP Surface Figure
400.000	-1.000	1.000	Secondary OAP to AFIT Input
-	-	-	

Figure 4.6: RCOS Off-Axis Mersenne Telescope Optical Alignment Tolerances [19]

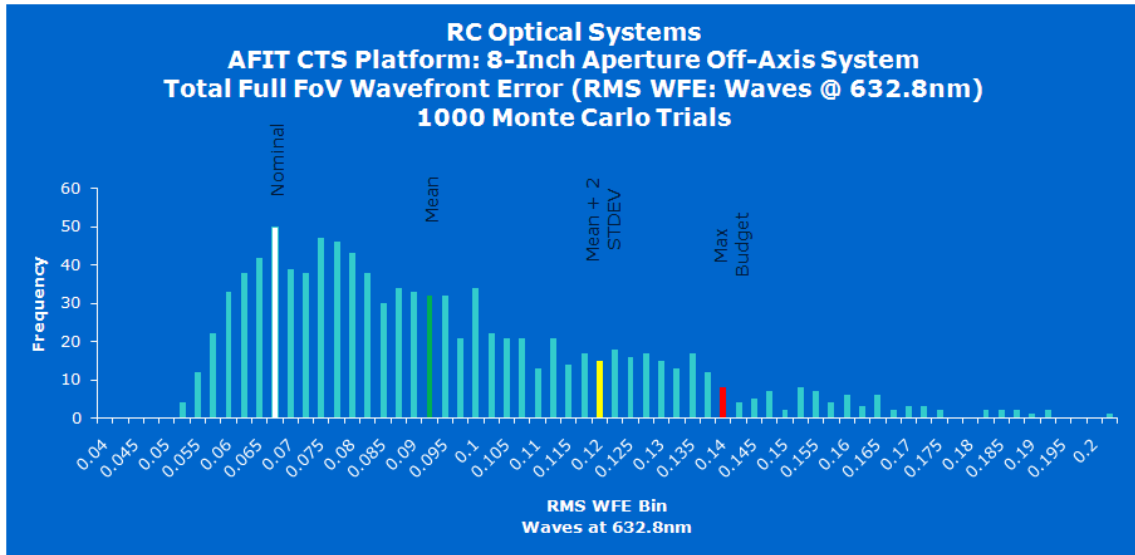


Figure 4.7: RCOS Off-Axis Mersenne Telescope Monte-Carlo Simulation of Perturbations to Alignment Tolerances [19]

Figure 4.8 and 4.9 present the initial thermal analysis provided by RCOS comparing aluminum and Invar breadboards. Figure 4.8 was created using an aluminum breadboard showing that the off-axis Mersenne telescope would have a very narrow thermal range in which the optics would have to be maintained to meet optical performance requirements. Figure 4.9 is the same analysis using an Invar breadboard which has a very low thermal expansion rate. Based on this analysis, the contractor concluded that an Invar breadboard was required for the imager to operate in an exposed space environment and meet optical performance requirements without using active thermal control, which would be required if an aluminum breadboard was used [19].

For alignment, a bonding agent was selected. After the telescope is aligned with an interferometer, the adjustment screws will be bonded with EPO-TEK 820 epoxy to prevent any future changes in alignment. This epoxy was selected because it is designed for mounting optically sensitive components and has very low outgassing properties. The specification sheet for this epoxy is contained in Appendix D for further review.

Aluminum 6061:
CTE = 23.4 E-10/C

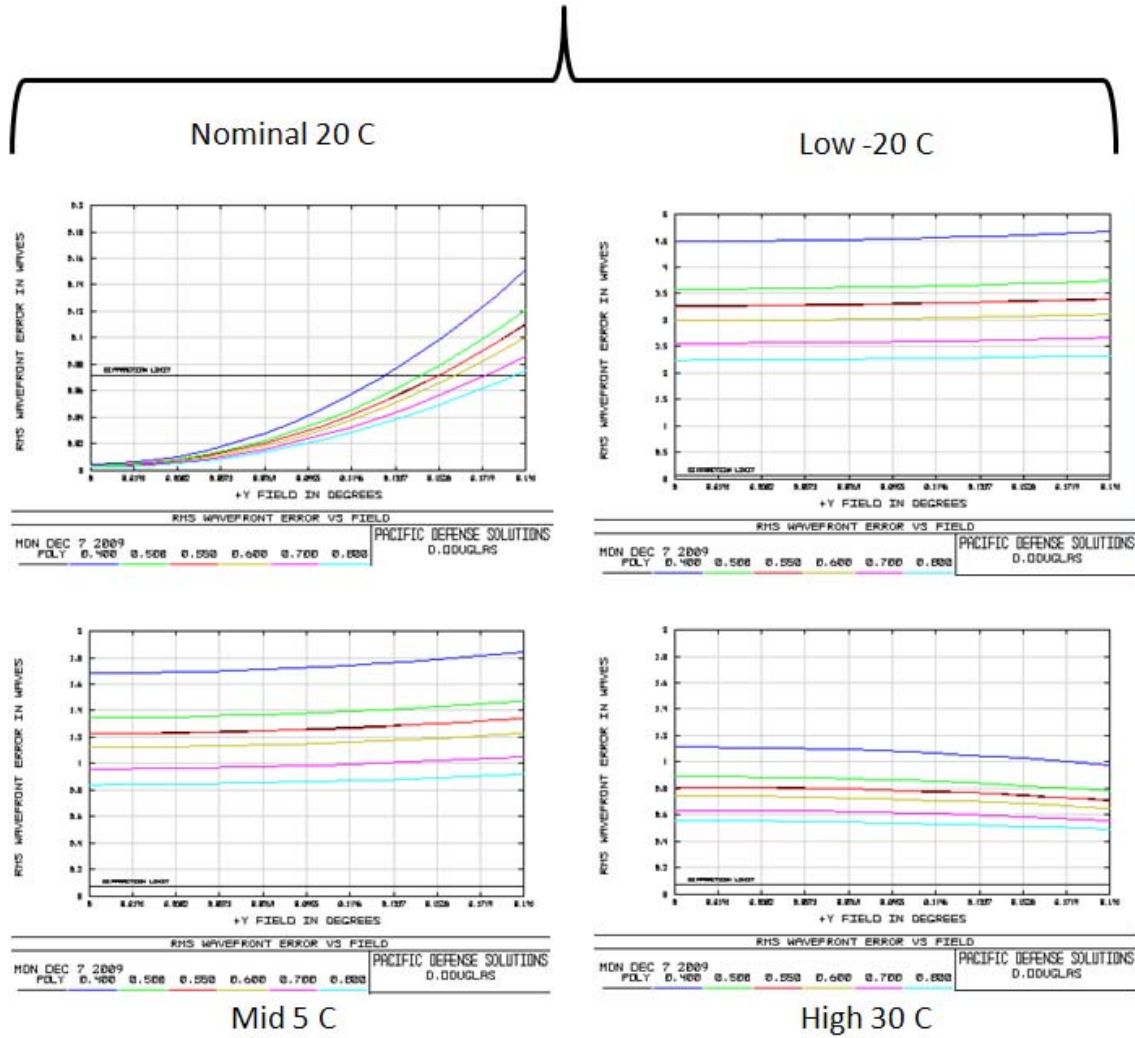


Figure 4.8: RCOS Off-Axis Mersenne Telescope Thermal Performance for Aluminum Breadboard[19]

Invar (Typical):
 $CTE = 1.2 \text{ E-}10/\text{C}$

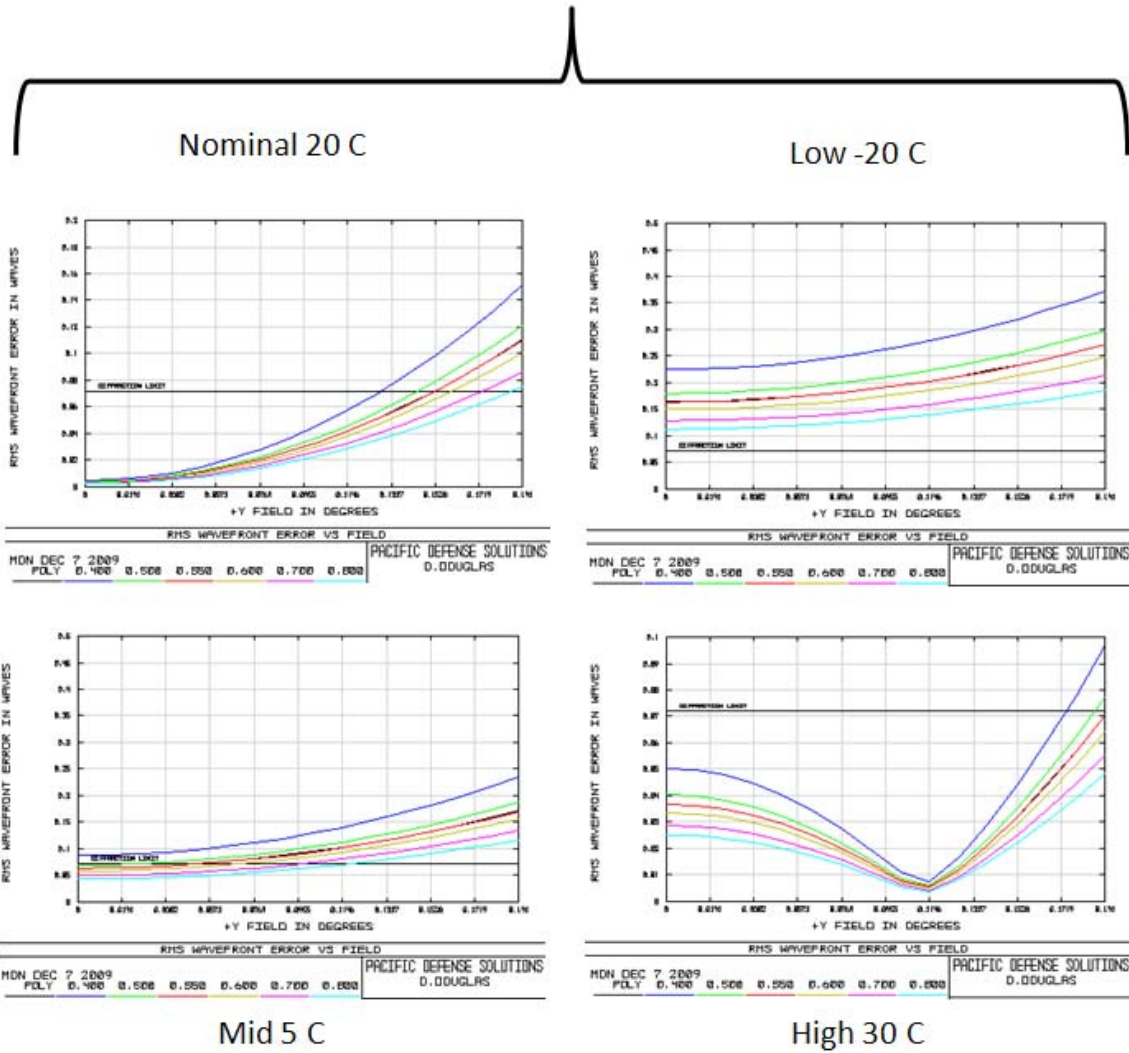


Figure 4.9: RCOS Off-Axis Mersenne Telescope Thermal Performance for Invar Breadboard[19]

Figure 4.10 displays the mechanisms that were selected for the off-axis Mersenne telescope. The first one is the dwell mirror mechanism. Instead of using a traditional two axis gimbel, which has a higher profile, two Aerotech ADRS-200 rotary stages will be utilized with a wedge in between them for two axis control. The dwell mirror mechanism will require two Aerotech Ensemble CL controllers for operation, one for each rotary stage. The Fast Steering Mirror (FSM) mechanism is the Physik Instruments S-340 tip/tilt platform. It requires one Physik Instruments E-616 controller for operation. Although it will not be provided by the contractor as part of the off-axis Mersenne telescope, the Physik Instruments M-122 precision micro-translation stage was selected for the field stop at the focus point. The contractor stated that all mechanisms are vacuum rated. Vendor documentation for mechanisms and controllers is contained in Appendix D.

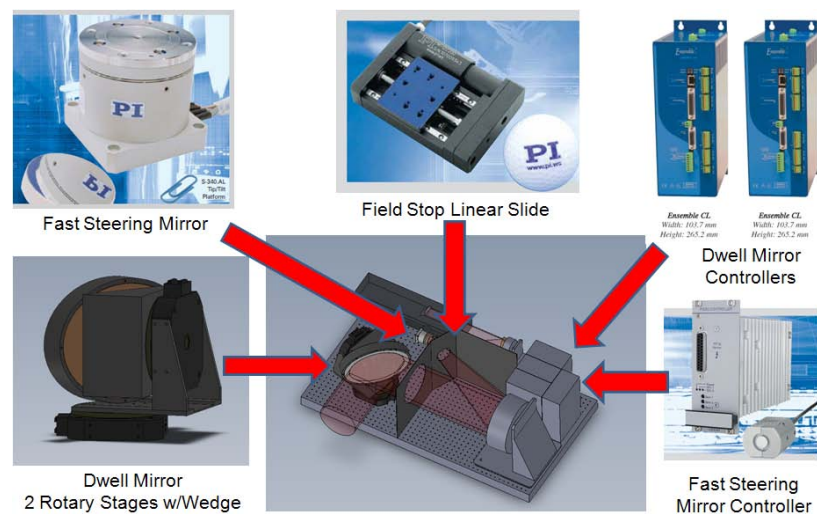


Figure 4.10: RCOS Proposed Mechanisms and Controllers [19]

Figure 4.11 contains the proposed schedule that was briefed by RCOS. The schedule, assuming approval of the design, starts with initial component procurement on 14 December 2009. The longest lead time is for fabrication of the OAPs by a sub-contractor in New York. The main fabrication for the telescope will take place at RCOS in Arizona, but after shipment, the final alignment will happen at the sub-contractor's location in New York. The telescope will then be transported to AFIT approximately the first week in May 2010.

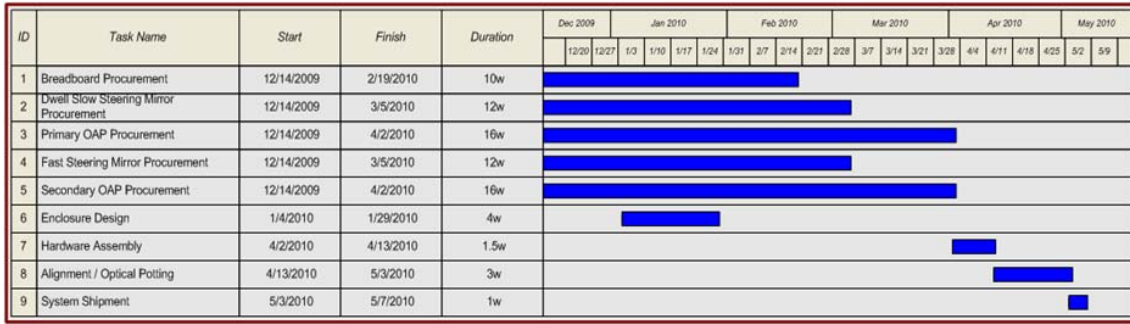


Figure 4.11: RCOS Proposed Procurement and Delivery Schedule [19]

4.3 Results

The mission plan for CTE_x was used for setting most of the design requirements and limitations for the off-axis Mersenne telescope. The size limitations of the EF payload bays on the JEM and estimated additional structure and components was the reason for constraining the telescope size. The experimental objectives and desired abilities were responsible for determining the contract requirements for optical and mechanical performance of the telescope. Thermal and survival requirements for the proposed design were dictated by the launch and exposed space environment.

The RCOS design that was briefed to AFIT meets all of the requirements that can be validated at this point in the acquisition process. It is within the imposed size limitations and provides the required space for additional CTE_x instrumentation. The required GSD and FOV as well as mechanical abilities for the telescope should allow the space-based CTE_x to achieve its objectives. The optics should be free of aberrations and unaffected by thermal cycling. Adequate measures are being taken to ensure proper alignment when subjected to launch stresses with the epoxy bonding of adjustment screws and the inclusion of one-time tie downs for moving components within the telescope.

Overall, AFIT accepted the current drawings for the RCOS off-axis Mersenne telescope design. This acceptance triggers two events. It triggers the first quarter of the contract payment to be released to RCOS and the start of procurement by RCOS for the main components of the telescope.

However, with the initial approval of the off-axis Mersenne telescope drawings, AFIT expressed several concerns to the contractor that need to be addressed. There

were several concerns for the selected controllers. The controllers are the limiting factor for the temperature regime with operating temperatures between 0-50 degrees and 5-50 degrees celcius. These operating temperature ranges do not meet the generally accepted space requirements of -30 to 80 degrees celcius. The input voltage for the controllers is AC, rather than DC as used on the ISS. Understanding that the wiring was vacuum rated, there was concern over the makeup of the wiring insulation to ensure that it meets flammability requirements for space qualification. The final issue addressed was the noise profile of the dwell mirror mechanism. RCOS understood all the concerns and was going to address these issues prior to final delivery.

V. CTE_x On-Orbit Focusing, Alignment, and Calibration

5.1 Methodology

Focus, alignment and calibration are critical to the operation of CTE_x while on orbit. Each method needs to be developed to be as simple as possible, and lower risk and cost, while meeting the technical requirements of the imager and overall experiment. The following chapter involves a trade study and creation of schemes to focus, maintain optical alignment and calibrate the CTE_x imager. It is organized in five sections that include; Methodology, Focusing, Maintaining Optical Alignment, Calibration, and Results.

5.2 Focusing

While on orbit, CTE_x will need to be able to adjust its focus. Although it is possible to design an optical system with an entirely fixed-focus system with extensive analysis and modeling, as was the case for the HICO sensor discussed in Section 2.1.2, it is desired to have some active focus control for CTE_x at this point in the design process to account for any uncertainties [42]. There are currently two focus points in the CTE_x optical design: one at the field stop location as shown in Figure 5.1 labeled Focus Point Location and another one at the camera array in the primary CTE_x instrument. The telescope is being designed with a fixed focus for the first focal point. The active focus control for CTE_x is designed to occur at the second focal point on the camera array. For active focus control, two options were considered: a focusing lens or mirror. The focusing lens represents the simplest mechanism at this point in the design process.

Given the active focus control at the camera array, the question then becomes what is the ideal method to determine the required focus setting. Since the telescope is fixed focus, changes in the ISS altitude do not need to be accounted for. Analysis of the root mean square wave front error (RMS WFE) showed that altitudes and slant ranges greater than 50 km will be in focus for the telescope prescription because the wave front error is less than 2 times the diffraction limit. Even though the telescope is fixed focus, it is still desired to have an active focus control at the camera array to account for any uncertainty or shift of optical components. Given that the optical compartment will be thermally controlled while in orbit to some extent, discussed later in Section 5.3,

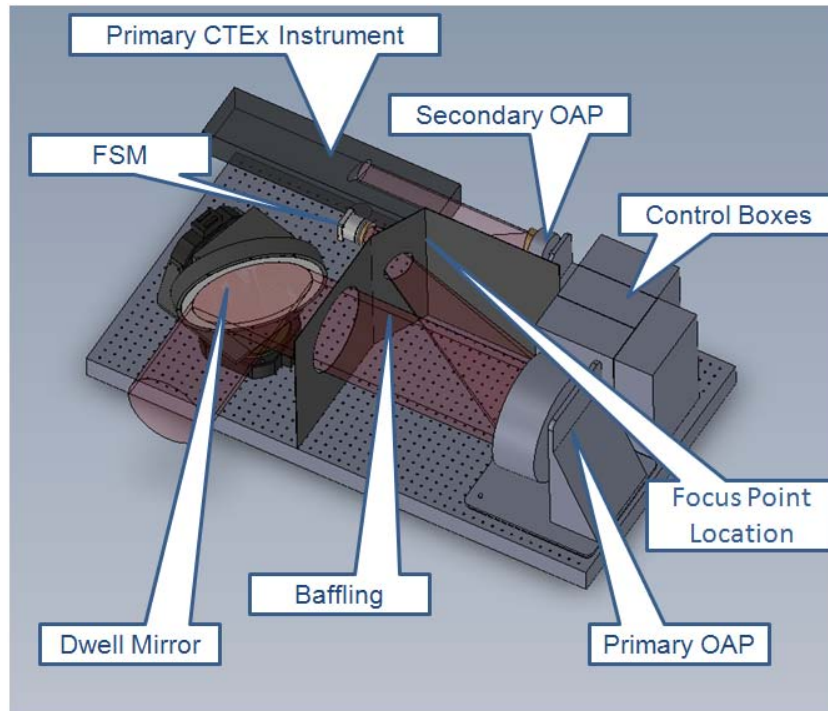


Figure 5.1: Conceptual imager design [19]

the initial focusing procedure should only need to be accomplished once during system checkout to adjust and fine-tune the focus following the violent launch environment.

Determination of the optimal focus setting for the CTEEx focus control on the camera array will occur on the ground during the system design and characterization process, prior to launch. This process ensures that only minor changes maybe required after launch, thus lessening the number of focus steps that must be stepped through vicariously to optimize focus while on orbit.

After launch, the ideal primary method for optimizing focus is by using a vicarious target. ARTEMIS did this using a high spatial frequency scene as discussed in Section 2.4.1, however, unlike ARTEMIS, CTEEx would require the collected images to be processed and reconstructed into traditional hyperspectral cubes before this method could be used. The ideal vicarious focus scheme for CTEEx would not require processing first. This can be done with CTEEx by instead of viewing a high spatial frequency scene, using a single sodium street light in a remote location at night. Knowing the theoretical focus setting from the design and ground characterization, a range of focus steps forward and

aft of this setting should be selected. A single pass will be done over a remote area with a sodium street light at night while stepping through the range of focus settings. Once this data is down-linked, the scene with the sharpest sodium spectral features would represent the best focus setting. During the next uplink, the focus setting can be commanded to this position. As a backup, a focus target will be included on the field stop [17].

A couple of considerations need to be taken into account for focusing the instrument. A lesson from ARTEMIS is that vicarious focus should not be used until after the gains of the individual pixels in the array are averaged with the first vicarious radiometric calibration target because of possible errors using spatial frequency without first leveling the gains [37]. Another consideration is that changes in the focus setting have impacts on the calibration because it changes the spectral spread and offset. Impacts to the calibration are easily adjusted for on orbit during the focusing procedure by characterizing the changes in spectral spread and offset on the ground and applying these changes as a rough estimate to the down-linked focusing data cubes.

5.3 Maintaining Optical Alignment

Optical alignment is a critical concern for imagers because, with changes in alignment, aberrations such as those discussed in Section 2.3 can be introduced. In Figure 5.1, for CTE_x the critical alignment concerns are the alignment of the collimated light beam and the prism. The reason for this concern is that small changes in either of these alignments can have detrimental effects on the ability of the algorithm to reconstruct the data since changes in either alignment affects how the spectrum for a spatial pixel is distributed on the array. A change in alignment requires a re-characterization of the imager to be able to reconstruct the data. The requirements for re-characterization will be discussed in Section 5.4, the calibration section of this chapter. This section will cover maintaining optical alignment.

For analysis, it is important to remember the four alignment error mechanisms that could cause mis-alignment on orbit: thermal, vibration, gravity and launch stresses. While on orbit, CTE_x will experience thermal cycling as it moves in and out of eclipse

which will cause expansions and contractions in the optics and breadboard to which they are mounted. If the optics and their mounts have structural natural frequency within the vibration profile of its operating environment, amplifications caused by resonances can also cause misalignment. The optics will not experience gravity in orbit as they do on Earth during development. Finally launch stresses represent the most severe loads that the optics will be subjected to during their lifetime. Under all four of these stresses, the optics for CTE_x must be precisely aligned to produce high quality data.

With the two alignment concerns identified as the prism and collimated beam, only alignment of the collimated beam will be examined. Maintaining the alignment of the prism will not be covered here because the final prism design is currently evolving and not complete enough to start reviewing mounting options. The mounting of the prism will need to be examined in follow on research. Maintaining the alignment of the collimated beam can be done by ensuring the optical axis of the first off-axis paraboloid (OAP) mirror and the second OAP mirror remain perfectly parallel to each other. Maintaining this alignment has a couple of key benefits. One, it ensures the on-axis field of view is correctly aligned with the center of the prism. Two, it also ensures that the first focus point at the field stop is centered in the field stop aperture.

To control alignment within optical systems, there are two methods: active and passive. Active methods are the most complicated due to the complexity of their control systems and mechanisms. An active system is composed of an actuator with encoder, a feedback sensor to measure alignment and a control system to autonomously correct the alignment. Due to complexity and expense, active methods are usually only used where they are absolutely necessary to correct cyclic errors such as jitter. Passive measures, rather than constantly trying to control the alignment like active measures, are used to maintain the alignment of an optical system from the start. Passive measures may include selecting materials with low thermal coefficients of expansion, or extensive modeling to correct for possible issues to name a few. Passive measures are the preferred choice for most applications due to simplicity and cost.

Only two of the mechanisms mentioned earlier are cyclic that could cause misalignment: thermal and vibration. Thermal cycling can be accounted for passively by

performing a very detailed analysis and/or designing the optics using costly materials with very low thermal expansion properties. However, an active method to account for thermal cycling is to thermally control the CTE_x optical package within its upper and lower thermal limits. The current plan is to design the CTE_x optical package to the lowest and highest thermal range possible in orbit. Film heaters on the optical package will be included if necessary to overcome any shortcomings in meeting alignment requirements based on orbital thermal loads. The alignment of the optics during thermal cycling will be tested by measuring the alignment during thermal vacuum (TVAC) ground testing to ensure the proper temperature range and gradient is maintained within the optical package and determine its behavior on orbit.

Vibration is the other cyclic mechanism that can cause misalignment. Here the concern is to ensure the optical package of CTE_x does not have natural frequencies within the excitation environment profile of the ISS that would resonate in the optics causing misalignment. Two passive mechanisms can be utilized here. The first is the use of finite element models to perform an eigenvalue analysis to ensure all the natural frequencies in the optical system are greater than the ISS vibration spectrum. The second passive measure to is verify the natural frequencies are above the excitation spectrum of the ISS during the vibration testing for space protoqualification mentioned below. Research on a passive vibration isolation system for CTE_x is contained in the master's thesis, *Investigation of a Novel Compact Vibration Isolation System for Space Applications* by Miller [56].

The next mechanism that can cause misalignment on orbit is gravity. Gravity misalignment can be dealt with by conducting a simple passive ground test to ensure the lack of it on orbit does not cause mis-alignment. On the ground, the alignment of the optics should be verified. Once the alignment is verified, the optics should be flipped 180 degrees so that gravity is acting in the opposite direction and then the alignment reverified. If the alignment changes, then the optics have a gravity-induced alignment issue requiring redesign. This test should also be performed when the telescope is delivered from the contractor to verify that the telescope design upfront does not suffer from gravity-induced misalignment.

The final and most severe mechanism on maintaining the optical alignment is launch stresses. During ascent, the optics will be subjected to very severe loading and vibration (15-20 g's) that can cause permanent mis-alignment of the optics. Launch stresses can be dealt with by using several passive mechanisms. The first one is design in which launch loads and vibrations are approximated and accounted for as part of the modeling process. Another passive measure is the use of close tolerances during manufacturing to ensure there is no room for the optics to shift in the first place. A final passive mechanism is the use of random vibration testing during space qualification. After checking alignment on the ground and as a part of protoqualification for space, a random vibration test equal to three decibels above the maximum expected flight level for a one minute duration in each of the three axes is performed [57]. After the random vibration test, the alignment of the optics is reverified. If changes in the alignment occur, then the source of the misalignment must be located in the optics and corrected prior to the testing being performed again.

With the alignment between the OAPs being a primary concern, the lock-down method used by the telescope contractor to maintain alignment of these elements was reviewed as a part of Chapter Four. The mounts for the OAPs will be secured directly to the breadboard utilizing bolts. Once the contractor verifies the alignment of the telescope optics, the alignment mechanisms for the OAPs will be permanently secured using EPO-TEK 320 epoxy which has very low outgassing. The use of bolted mounts and epoxy for the adjustments should adequately secure the OAPs during CTEEx's lifetime and prevent shifting during launch.

5.4 Calibration

Calibration of a scientific instrument correlates its data to that of recognized standards. Just like any other scientific instrument, CTEEx requires calibration to validate and ensure the integrity of its data. The complexity of chromotomography appears during calibration of the imager. In chromotomography, the prism alignment and spectral calibration go hand in hand, which is not the case with most traditional spectrometers. The alignment of the prism disperses the spectral data of a spatial pixel on the array face.

Its spectral spread must be exactly known in order to be able to reconstruct a traditional data cube from a chromotomographic image. For traditional spectrometers, just spectral and radiometric responses need to be calibrated, however for a chromotomographic hyperspectral imager four characteristics must be measured; offset, spectral spread, undeiated wavelength, and pixel gain. For CTE_x, pixel gain (radiometric) calibration is the same as with traditional hyperspectral imagers.

Figure 5.2 displays the first three characteristics for calibrating a chromotomographic imager using the spectral lines of a single spatial pixel of a mercury lamp source with prism rotation angles of 0, 90, 180 and 270 degrees. Given the alignment and spectral geometry of an ideal chromotomographic imager, the center of rotation would be on the spectral line at 550 nm with no offset. As shown in Figure 5.2, this is not the case because the undeiated wavelength is displayed as approximately 540 nm with an offset. All of these three measurements; offset, undeiated wavelength, and spectral spread, must be known precisely in order for the algorithm to be able to reconstruct an image. These characterizations are currently obtained by looking at a one spatial pixel source with a known spectrum at prism angles of 0, 90, 180, and 270 degrees.

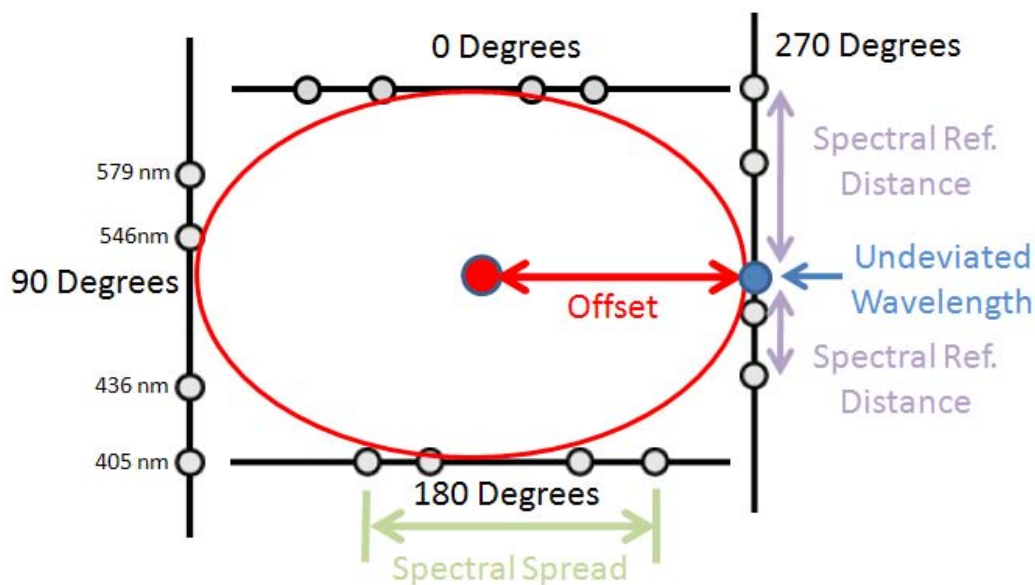


Figure 5.2: Graphic Depiction of a Mercury Line Source with Prism Rotation Angles of 0,90,180,270 Degrees

For spectral calibration, several measurements are needed: offset, undeviated wavelength and spectral spread. The offset is the measurement in pixels from the center of rotation to the undeviated wavelength, which is the point on the spectral line perpendicular to the center of rotation. The offset can be measured at only one prism rotation angle, but as shown this offset may be different for different prism angles creating an ellipse as shown in Figure 5.2 or another shape instead of a perfect circle. To currently characterize the offset, four prism rotation angles at 0, 90, 180, and 270 degrees are utilized. In order to determine the undeviated wavelength, the spectral spread must first be determined. The spectral spread is calculated by counting the number of pixels between the reference spectral points. In Figure 5.2, the reference spectral points of a mercury source are 405, 436, 546 and 579 nm. The spectral spread is a nonlinear relationship that allows a spectral wavelength value for each pixel along the spectral line to be determined. Once the offset and spectral spread are determined, the pixel position of the undeviated wavelength can be correlated to a spectral wavelength. Characterization of the offset, spectral spread and undeviated wavelength completes the spectral calibration of CTE_x, leaving just the radiometric calibration.

In order to calibrate CTE_x on orbit, provisions must be implemented for calibration during the design process. For calibration, the imager's field of view must be limited by the field stop to roughly one spatial pixel. At least two narrow bandwidth spectral sources are required to draw the spectral line for a spatial pixel, but the more spectral sources on this line the better as long as there remains some spectral separation between them. The reference spectral sources should be spaced over CTE_x's spectrum of 400-900 nm, but should be skewed toward the lower wavelengths due to the greater spectral dispersion angle as shown in Figure 5.3. If an on-board calibration source is used, its irradiance should be approximately 0.08 $\mu\text{W}/\text{pixel}$. The reason for this irradiance is that it is the calculated value that the imager will typically see while conducting imaging of the Earth's surface in orbit [17].

For CTE_x, it was determined that the best calibration approach was to use both on-board and external calibration approaches. Using this approach seems logical for a traditional hyperspectral imager using the on-board source to monitor calibration trend-

ing and the external source for the absolute calibration, but chromotomography has different requirements for calibration.

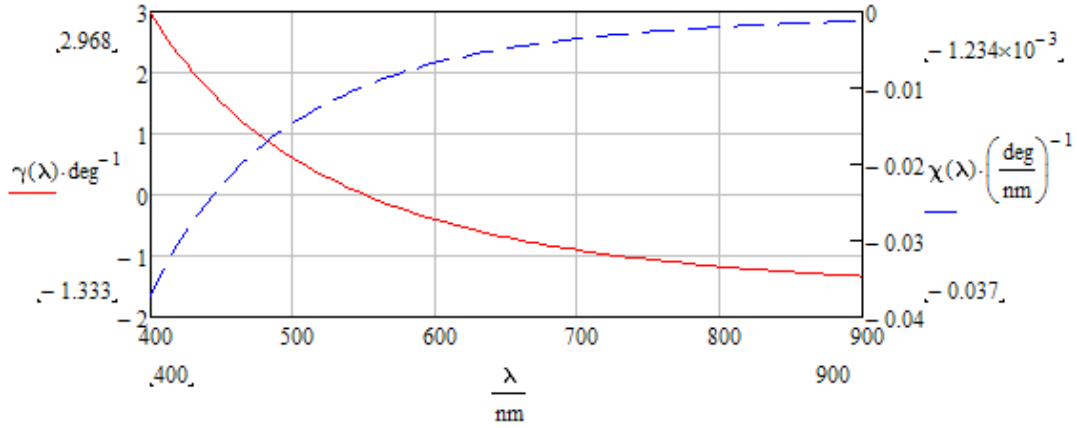


Figure 5.3: Theoretical Spectral Dispersion of the CTEEx Prism [17]

5.4.1 On-board Calibration. For chromotomography, the use of an on-board source is initially necessary to characterize the offset, undeviated wavelength and spectral spread after launch. Unmonitored slight changes in these values during launch can have drastic consequences on the ability of the algorithm to deconvolve the collected images. Providing the imager with a known on-board source will make it easier for the ground team to make slight modifications to algorithm’s variables by knowing what the deconvolved image should look like to measure the offset, undeviated wavelength and spectral spread. Once the algorithm is updated to take into account any launch changes, vicarious external calibration sources can be utilized to fine tune the spectral and radiometric response of the CTEEx imager.

5.4.1.1 On-board Calibration Source Trade Study. The initial trade was to determine where to introduce the on-board calibration source. A calibration source can be introduced either mid-imager or at the aperture. The drawback in introducing the calibration source mid-imager is that a pick-off mirror would be required. A pick-off mirror is a mirror that can be inserted into the optical path to redirect the optical path and then withdrawn as required to restore the original optical path. While on orbit, a mechanical pick off mirror is subject to failure and could catastrophically destroy the

experiment if it became stuck in a position that blocked the imager optical path. There are ways to reduce the risk of a pick-off mirror failure, but the risk can be eliminated altogether by introducing the calibration source at the entrance aperture without blocking the optical path. This can be done if the calibration source mechanism is small enough that it could be placed on the instrument aperture cover, thus not adding any more risk to the instrument, just a little more complexity to the aperture cover. However, a calibration source introduced at the aperture entrance adds the requirement that the beam must be collimated. By being collimated and on-axis, the imager for simplicity of description will believe source is a single point within its field of view, in addition to nearly eliminating the chance of stray light in the imager. Stray light would degrade the capabilities of CTE_x by interfering with the calibration.

Several potential calibration sources that meet the requirements of the imager were considered. These potential sources included a mercury lamp, an irradiance lamp with spectral filter, assorted light emitting diodes, and assorted lasers. Each source had its own advantages and disadvantages.

The first source considered was a single mercury lamp, which is currently used to calibrate the ground-based CTE_x. The mercury lamp provides four distinct peaks at 405, 436, 546, and 579 nm, which are skewed toward the lower wavelengths as required, but has no peak in the upper wavelengths of the CTE_x spectrum. The disadvantage is that in order to get these spectral peaks, a medium (3-4 atms) or high (7-8 atms) pressure mercury lamp has to be used, since low pressure lamps only show a peak in the UV spectrum. The increased pressure of a medium or high pressure mercury bulb may be detrimental to the spectral source's lifetime on-orbit without further characterization. Having a pressurized glass bulb on-orbit would lead to a requirement for secondary containment in case the glass bulb exploded. No vendors that produce space-qualified mercury lamps could be located, so commercial-off-the-shelf (COTS) mercury lamps would have to be used. COTS mercury lamps can be purchased with a collimating optic for \$ 3000 to \$ 4000, but the aluminum housings are designed for convection cooling and would require modification. Another issue with COTS mercury lamps is that most lamps have a requirement to remain nearly vertical. This means that most COTs mercury

lamps would not operate correctly in a non-gravity environment. Only certain types of COTS mercury lamps can be utilized. Also, a second backup lamp is required to reduce chance of failure.

The second source considered was a single irradiance lamp with a filter wheel. The advantages of this setup were that the spectral references could be tailored with narrowband filters and that a low pressure lamp was utilized. However, this method suffered most of the same drawbacks as the single mercury lamp without the higher bulb pressure and bulb orientation issues, and it introduced another level of complexity and possible failure mechanism with the need of a filter wheel. In addition, COTS narrowband filters still have a wide spectral range of 10-15 nm.

The third source considered was using several light emitting diodes (LEDs). LEDs offered several advantages such as numerous spectral choices and cheap redundancy, because a LED is required for each spectral reference wavelength. However, LEDs have some disadvantages. Their spectral width is a broad bell-shaped curve, thus requiring a spectral filter to narrow their spectral response. The peak wavelength can also drift with changes in temperature. The largest problem is that it is difficult to collimate LEDs with better than three degrees of divergence due to them not appearing as a perfect point source.

The final source considered was lasers. Laser diodes and/or diode pumped solid state lasers are offered in numerous narrow bandwidth spectral choices over the spectral range of the imager. COTS heat sinks and collimator assemblies are available for laser diodes. They also have a reduced risk of failure like the LEDs, because a separate laser is required for each spectral reference wavelength. The drawback for lasers is that like the LEDs, but to a lesser extent, the center wavelength drifts slightly with temperature. They also require active control chips to regulate temperature and power, but COTS chips are available.

Table 5.1: On-Board Calibration Source DECMAT

	Risk	Complexity	COTS	Cost	Total
Mercury Lamp	3	1	3.5	3	2.625
Irradiance Lamp/Filters	4	4	3.5	4	3.875
LEDs	1.5	3	2	1	1.875
Lasers	1.5	2	1	2	1.625

To further evaluate the candidate options for on-board calibration sources, the decision matrix (DECMAT) in Table 5.1 was used. Each calibration source was evaluated over four categories. For each category, a one value represents the best rating and four the worst rating. The first category was risk, which evaluated the possible risk of each calibration source failing. The second category represented the complexity of each mechanism. COTS evaluated whether commercial off the shelf hardware could be utilized and if modification was necessary. The final category was cost.

The first category that was examined was risk. LED and lasers tied because they represented the lowest risk, since the failure of one just meant the loss of one spectral reference wavelength rather than the complete loss of the calibration system. The mercury lamp was selected as the least complex, because it required no additional equipment other than containment and collimation optics. For COTs, lasers were selected as the best choice due to their wide availability and likelihood of being easily adapted for space use. LEDs were selected as the cheapest for the cost category followed by laser diodes. Based on the previous advantages and disadvantages, and the DECMAT in Table 5.1, the optimal on-board calibration source is to use a series of lasers.

5.4.1.2 Laser Source Trade Study. There are numerous types of lasers with different wavelengths and complexities available, but laser diodes and diode pumped solid state (DPSS) lasers were the two entirely different systems that were considered for CTE_x. Laser diodes are the simplest. DPSS lasers usually use a laser diode to excite a material. The advantage of DPSS lasers is that they can operate at numerous frequencies through the CTE_x spectral regime. Laser diodes are less complex, but constrained to wavelengths from 405-488 nm and 635 nm and up due to technological issues. It is

possible to create a green laser (532 nm) using a 1064 nm laser diode with a frequency doubler, but currently this is not possible using just a laser diode. Using laser diodes would provide no calibration sources between 489-634 nm. However, given that the theoretical undeviated wavelength for the CTEx is 550 nm, not having spectral references in this range close to the center of rotation is still an issue, but one that can be lived with. Laser diodes will be used for calibration over DPSS lasers due to lower cost and complexity.

When using laser diodes, one needs to be aware of their failure mechanisms. There are numerous failures that can happen during the manufacturing process of laser diodes that will be tested for before launch, but close attention needs to be paid to two during mounting and operation that can lead to catastrophic optical damage. The first one is thermal failure. It can happen during mounting when the diode is not properly connected to its heat sink and during operation if the temperature of the laser diode exceeds its specific operational thermal limits. A heatsink compound that does not outgas can be used between the diode and heatsink during assembly to ensure heat transfer. In addition, the temperature of a laser diode can be controlled using a thermoresistor and thermo-electric cooler (TEC). The second failure mechanism during operation is exceeding the current density limit of the laser diode. The second failure mechanism can be controlled by regulating the current supplied to the laser diode using a laser diode driver [58].

Two different control loops are required for laser diode operation to prevent failure mechanisms. One is a laser driver and the other is a thermo-electric cooler driver. There are two types of laser diode control: automated current control (ACC) and automated power control (APC). ACC seeks to keep a constant current to the laser diode during operation, which is the simplest control, but the intensity of the laser can vary. APC seeks to keep a constant laser intensity by using an integrated photodiode for feedback control. Since the laser diodes will be used for calibration, an APC controller is required.

Space qualification standards for laser diodes are outlined by the NASA parts and packaging program (NEPP), and include performance, screening, destructive physical analysis, and qualification. Performance consists of evaluation criteria for the selection of candidate laser diodes. Screening and destructive physical analysis consists of testing and

inspections. Qualification is close to normal space qualification standards used for other parts with some modifications. Given that the maximum experiment design lifetime is one year, some life expectancy standards do not have to be as high as with other missions and will need to be evaluated on a case by case basis. For further information, NEPP’s publication on High Power Laser Diode Array Qualification and Guidelines for Space Flight Environments can be consulted [58].

The irradiance of each source is required to be close to what the imager array would normally experience under normal operating conditions, which is $0.08 \mu\text{W}/\text{pixel}$. To translate this requirement into laser diode power, the overall calibration of the imager has to be considered. Since the array’s spatial field of view is constrained by the field stop to nearly a pixel during calibration, all the irradiance will be recorded on one pixel. Based on the constrained field of view, the collimated laser diode will need an irradiance of $0.08 \mu\text{W}$ at the entrance aperture. Given that the lowest power for typical laser diode is approximately 5 mW, the irradiance must be reduced.

To reduce the irradiance, two methods are available; shortening the camera exposures time or decreasing the source intensity using a neutral density filter. Shortening prevents the pixels from becoming saturated by giving them less time to ramp up during an exposure. A neutral density filter is designed to either reflect or absorb a certain percentage of a light source’s intensity. The author’s recommendation to reduce the irradiance is to pick a neutral density filter with a close optical density, and then adjust the required exposure time. The exact adjustment of the exposure time can be experimentally determined during ground testing prior to launch.

Given that laser diodes are being used, an absorbent neutral density filter is required in order to prevent back reflections that can damage a laser diode. The sizing of the neutral density filter can be calculated by using Eq. (5.1) [59],

$$OpticalDensity = \log \left[\frac{I_{In}}{I_{Out}} \right] = \log \left[\frac{5000}{0.08} \right] = 4.79 \quad (5.1)$$

where the input intensity $I_{In}=5000 \mu\text{W}$ and the output intensity $I_{Out}=0.08 \mu\text{W}$ is the intensity. Since a neutral density filter of 4.79 is not commonly available using commercial

off the shelf equipment, a 4.0 neutral density filter will be used. Using a 4.0 neutral density filter, Eq. (5.2) gives an intensity output of $0.5 \mu\text{W}$ for a 5 mw laser diode, which is roughly six times brighter than an observed scene, but acceptable given that all the energy may be focused over an area that is slightly larger than an ideal single pixel and the exposure time of the pixels can be adjusted. Eq. (5.3) gives the same intensity output of $0.5 \mu\text{W}$ for a 50 mw laser diode using a 5.0 neutral density filter.

$$I_{Out} = \left[\frac{I_{In}}{10^{OpticalDensity}} \right] = \left[\frac{5000}{10^4} \right] = 0.5 \mu\text{W} \quad (5.2)$$

$$I_{Out} = \left[\frac{I_{In}}{10^{OpticalDensity}} \right] = \left[\frac{50000}{10^5} \right] = 0.5 \mu\text{W} \quad (5.3)$$

The final part of the on-board calibration source trade study was the mounting. The two options that were considered were mounting the spectral sources on the aperture cover or off the aperture cover, while using a fixed mounted mirror on the aperture cover to direct the sources into the optical path. The selected option is to mount the sources on the aperture cover. Although this does slightly complicate the aperture door design, it does simplify the optical alignment because the sources have to be aligned closely parallel to each other. They all must be aligned within 0.05 degrees of each other, which is the designed CTEx angular field of view. As long as they are closely parallel to within 0.05 degrees, the slow dwell mirror could provide a correction to ensure they would be aligned along the optical axis of the telescope's field of view. In addition, mounting them on the aperture door cover assists in the thermal conductivity from each laser diode's heat sink during operation. However, if space requirements dictate mounting them off the aperture door and using a small mirror on the door to introduce them, this would be acceptable as a second choice for the mounting configuration.

The on-board laser calibration system is meant to provide initial calibration for CTEx when the aperture door is closed. However, repeatedly opening and closing the aperture door to track calibration trending between vicarious calibrations can lead to failure of the aperture door. To provide calibration trending reference while the aperture door is open, a filter wheel with several narrow bandwidth filters will be installed in the

collimated beam in front of the prism for this purpose. By rotating a narrow bandwidth filter into the optical beam, the trending of the calibration can be tracked between vicarious calibrations with the aperture door open. Trending of the system calibration is required to let the operator know how much the calibration has changed since the last update and to determine when to do the next vicarious calibration.

The question may be asked, why two on-board calibration systems instead of just using a filter wheel? The laser calibration system provides several benefits that a filter wheel can not. A laser provides a very narrow bandwidth when compared to a narrow bandwidth filter that has a 10-15 nm spread. The laser allows the system a defined reference with no stray light for initial alignment and spectral calibration on orbit, which can not be provided by the filter wheel.

For calibrations, all three systems will be used as follows: The laser calibration system for initial on-orbit calibration and as required to troubleshoot any technical problems. Vicarious calibration will be the primary calibration method for the imager on-orbit. The filter wheel with several narrow bandwidth filters for trending the imager's calibration between vicarious calibrations.

5.4.1.3 On-Board Pixel Characterization. LEDs suffer some draw backs as a calibration source, but they are ideal for pixel characterization. A LED on the aperture door with its dispersion would illuminate the entire primary OAP mirror and subsequent camera array. With an uniform irradiance source across the camera array, each individual pixel response can be characterized.

To use a LED to determine pixel response, this is done without spinning the CTE_x prism. To characterize the pixels, a series of images are taken with varying exposure times. The responses of each pixel to each exposure time can be plotted as shown in Figure 5.4. The pixel response is a function of the log of the exposure time. From this graph, several items can be determined for each pixel: blackout response, gain and saturation for a given source intensity. From this analysis, the pixel gains can be averaged prior to opening the aperture door. Hot or dead pixels can also be identified [60].

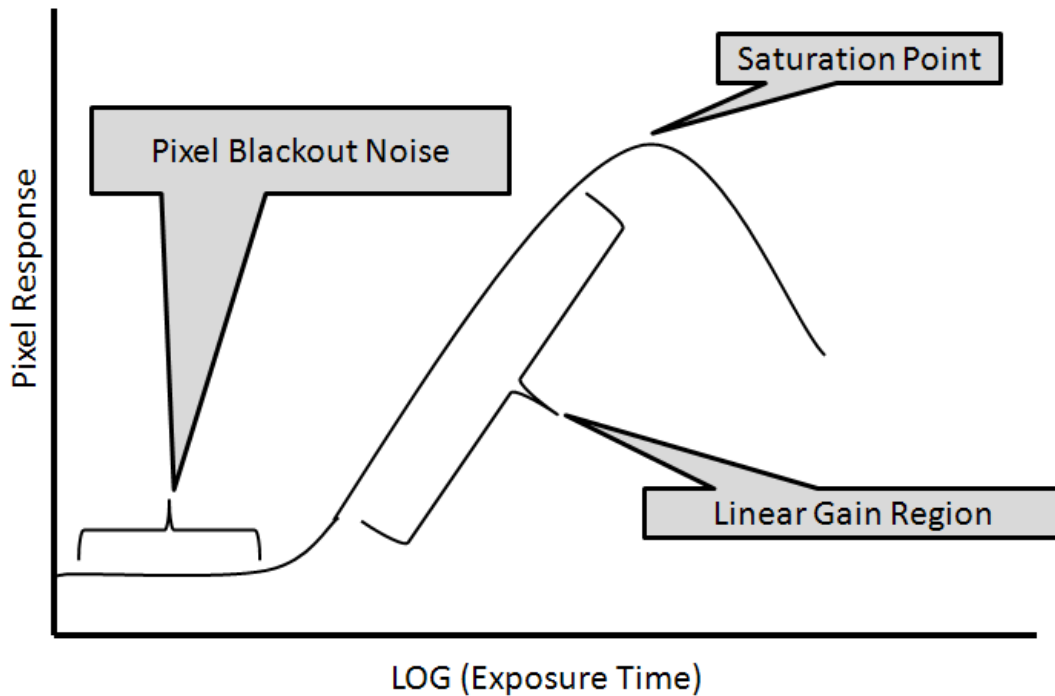


Figure 5.4: Theoretical Pixel Response Versus Log of Exposure Time

For an on-board pixel characterization system, several things are required. A narrow divergence green LED source mounted on the aperture door, which is close to the undeviated prism wavelength of 550 nm. The second item required is the ability to change the exposure time on the camera. The on-board pixel characterization ability will provide a necessary diagnostic tool to quantify the camera array.

5.4.2 External Calibration. The next part of the calibration trade study is to evaluate the individual external calibration techniques. Vicarious calibrations are required to verify spectral and radiometric performance of the instrument while on orbit. For external calibration techniques, several historical techniques cannot be utilized due to the imager design limitations, which include observation of the solar spectrum and moon reflectance. The reason for not using these techniques is because unlike other free flying imagers, CTE_x will be generally nadir pointing and not able to slew to point at the sun and moon because of mechanical and ISS shadowing limitations. With CTE_x nadir pointing, Earth-based vicarious calibration techniques are required.

For vicarious spectral calibration, the optimal technique is to utilize atmospheric absorption features. Every constituent of the Earth's atmosphere absorbs portions of the solar radiance at specific wavelengths, thus not allowing these absorbed wavelengths for the most part to be reflected back to CTE_x for collection. The spectral channel can be determined by selecting known atmospheric absorption features and comparing them to CTE_x data. Since the CTE_x is using roughly 5 nm spectral channels, the spectral accuracy of the instrument can be estimated at +/- 2.5 nm, although spectral resolution is better at lower wavelengths in reality due to greater prism dispersion. In the CTE_x's spectral range of 400-900 nm, there are numerous atmospheric absorption features from which to select. Strong absorption features are desired over weaker ones to ensure that they clearly stand out in the data cubes. While water vapor does show several absorptions within the spectral range of CTE_x, it is not desirable to use due to variable concentrations and the extra modeling required. The desired features for the CTE_x to use during vicarious spectral calibration are the atmospheric oxygen A and B bands since the concentration remains unchanged and these are strong absorptions. The oxygen A and B bands show strong absorptions at 762 nm and 687 nm, respectively [61].

The next part of the vicarious calibration technique trade study is the selection of Earth-based targets for radiometric calibration. For the proposed calibration scheme, two radiometric targets are required. The first target must be of uniform reflectance and large enough to fill the entire field of view of the CTE_x imager such as a desert, dry lake bed, or ice sheet. This target is needed in order to level the gains of all the pixels in the array prior to observing the second target. The second target must be a ground-based target with independent radiometric monitoring during the period of collection to which to compare the imager radiometric intensities. The second target does not need to cover the entire field of view of the imager, but needs to cover a couple of pixels by a couple of pixels in order to compare the imager radiometric measurement with the independently measured radiometric data modeled for the top of the atmosphere.

In order to select the first vicarious target, it is necessary to calculate the field of view of the imager to locate a target that fills the entire field of view. Eq. (2.5) is used to calculate the largest field of view in Eq. (5.4),

$$FOV = \pi \left[\left(\frac{h}{\cos \eta} \right) \tan \left(\frac{\theta}{2} \right) \right]^2 = \pi \left[\left(\frac{450}{\cos 8} \right) \tan (0.05) \right]^2 = 0.494 \text{ km}^2 \quad (5.4)$$

where h is the maximum expected ISS altitude at 450 km, $\frac{\theta}{2}$ is the half angle field of view at 0.05 degrees for the telescope, and η is 8 degrees for the maximum sensor slew off-nadir. The largest theoretical FOV is therefore 0.494 square km, which equates to a circular radius of 0.199 km. Making the assumption that pointing error is acceptable to half of the radius of the field of view, this results in a calculated *Minimum Target Diameter* of 0.597 km in Eq. (5.5),

$$\textit{Minimum Target Diameter} = (2 * R) + R = (2 * 0.199) + 0.199 = 0.597 \text{ km} \quad (5.5)$$

where maximum target field of view radius $R=0.199$ km.

A catalog of vicarious earth-based radiometric test sites is maintained on the United States Geological Survey (USGS) department's website. Although there are numerous sites listed, the Committee on Earth Observing Satellites (COES) has narrowed the list of sites down into eight instrumented sites and six pseudo-invariant test sites for the post launch characterization of space-based optical imaging sensors as shown in Figure 5.5 [9].

For the first radiometric target, any of the six pseudo-invariant sites listed in Figure 5.5 would be sufficient. All six of these are roughly uniform desert sites and larger than 50 km x 50 km. Each site definitely fills the field of view as required in order to level the pixel gains.

The recommended second calibration target is the LSpec Frenchman Flat, Nevada located at 36.80928 North 115.93479 West (50SMF 04984 74245 using MGRS coordi-

CEOS Reference Standard Test Sites							
#	Site	Center Latitude	Center Longitude	WRS-2 Path/Row	Point of Contact (POC)	Affiliation	Email
Instrumented Sites							
1	Dome C, Antarctica	-74.50	123.00	89 / 113	Stephen Warren	University of Washington	sgw@atmos.washington.edu
2	Dunhuang, China	40.13	94.34	137 / 32	Xiuqing Hu	NSMC/CMA	huxq@cma.gov.cn
3	Frenchman Flat, USA	36.81	-115.93	40 / 34	Carol J. Bruegge	NASA/JPL	Carol.J.Bruegge@Jpl.Nasa.Gov
4	Ivanpah Playa, USA	35.57	-115.40	39 / 35	Kurtis J. Thome	NASA/GSFC	kurtis.thome@nasa.gov
5	La Crau, France	43.56	4.66	196 / 30	Patrice Henry	CNES	patrice.henry@cnes.fr
6	Negev, Southern Israel	30.11	35.01	174 / 39	Arnon Karnieli	Ben Gurion University	karnieli@bgu.ac.il
7	Railroad Valley Playa, USA	38.50	-115.69	40 / 33	Kurtis J. Thome	NASA/GSFC	kurtis.thome@nasa.gov
8	Tuz Golu, Turkey	38.83	33.33	177 / 33	Selime Gurol	TUBITAK UZAY	selime.gurol@uzay.tubitak.gov.tr
Pseudo-Invariant Test Sites							
1	Libya 4	28.55	23.39	181 / 40	Patrice Henry	CNES	patrice.henry@cnes.fr
2	Mauritania 1	19.40	-9.30	201 / 47	Patrice Henry	CNES	patrice.henry@cnes.fr
2	Mauritania 2	20.85	-8.78	201 / 46	Patrice Henry	CNES	patrice.henry@cnes.fr
3	Algeria 3	30.32	7.66	192 / 39	Patrice Henry	CNES	patrice.henry@cnes.fr
4	Libya 1	24.42	13.35	187 / 43	Patrice Henry	CNES	patrice.henry@cnes.fr
5	Algeria 5	31.02	2.23	195 / 39	Patrice Henry	CNES	patrice.henry@cnes.fr

Figure 5.5: CEOS Reference Standard Test Sites [9]

nates). The reason for selecting this site over the other seven is that it is continuously instrumented with the data available online and updated every five minutes. Instrumentation provides measurements for surface reflectance, temporal surface reflectance, aerosol optical depth, wind speed and direction, temperature, relative humidity, pressure and soil temperature at the site. The data is available online using the query form as shown in Figure 5.6. Frenchman Flat provides an ideal calibration target with a 300 meter uniform area with 50 meters of that being instrumented by LSpec [20]. The USGS radiometric test site questionnaire is available in Appendix E of this report.

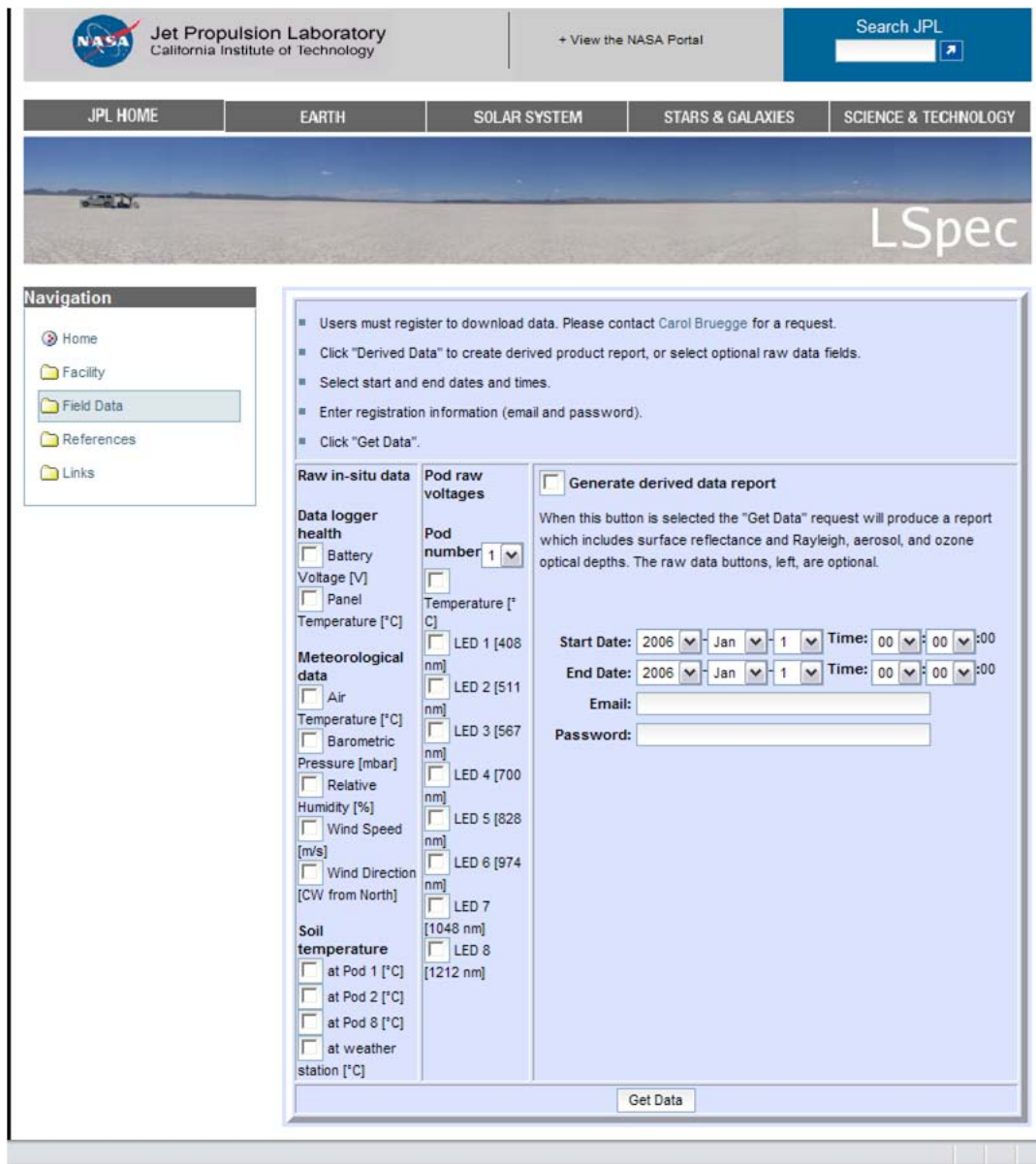


Figure 5.6: LSPEC Frenchman Flat Radiometric Calibration Site Data Query Page [20]

5.4.3 *Lab Experiment.* A lab experiment was conducted looking at the use of lasers for calibration by using the ground-based CTE_x. There were two goals for the experiment. One was to obtain knowledge of laser particulars that would affect calibration of CTE_x. The second goal was to look at the effect of misalignment of the calibration lasers when introduced close to the aperture of CTE_x with the theory being that the centers of rotation for each wavelength would be offset from each other.

The experimental setup displayed in Figure 5.7 was utilized. It consisted of the ground-based CTE_x imager, two laser pointers to simulate laser calibration sources, and several neutral density filters. The lasers used were 532 nm and 635 nm with a power of less than 5 mW. 2.0 and 0.4 optical neutral density filters were used as well as increasing the sampling rate and decreasing the exposure time on the camera to decrease the intensity of the lasers.

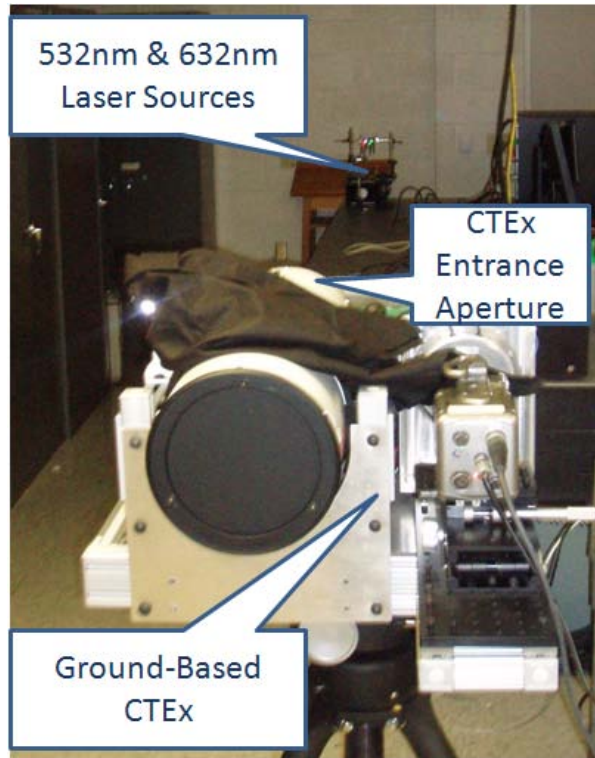


Figure 5.7: Lab Experiment Setup

The lasers were initially aligned to within 0.01 degrees of being parallel to each other. Alignment of the lasers was done by measuring the distance between the lasers at the source and again on the wall at 744 inches from the source. It was estimated that the measurement on the wall could be done to 1/8 inch due to dispersion of the laser beam, thus producing an accuracy for the alignment of 0.01 degrees. Images of the lasers were taken at 145 rotation angles as the prism performed one rotation. The laser alignment was then offset by spreading the lasers spots on the wall to 0.25 inches, which amounted to an offset angle between them of 0.02 degrees from parallel with a +/- error of 0.01

degrees. The images of the offset lasers were then again taken at 145 rotation angles as the prism performed one revolution.

After the experiment was completed, the images from the two data sets were analyzed. Figure 5.8 shows an image of both lasers closely aligned to within 0.01 degrees of parallel and a cross section of that image on the right. It is noticed on the left image that the lasers do not appear as clean sharp points. A cross section of both lasers on the right provides the registered pixel intensity. From the cross section several lessons were learned. First, the array was saturated by the intensity of the lasers as shown by the flat tops rather than sharp peaks. An optical filter with a greater density should have been used to prevent saturation. Two, the lasers were not perfectly collimated, which should have been expected when using laser pointers. The imperfect collimation is evident by the rough area displayed on the ramp up and down for each peak, which also shows the optics for the ground-based CTE_x were focused. If they were perfectly collimated, it would be a straight peak with no ramp. The effect of the less than perfect collimation was increased during the experiment because the laser sources were introduced roughly 12 ft from the aperture, thus allowing a greater amount of beam dispersion.

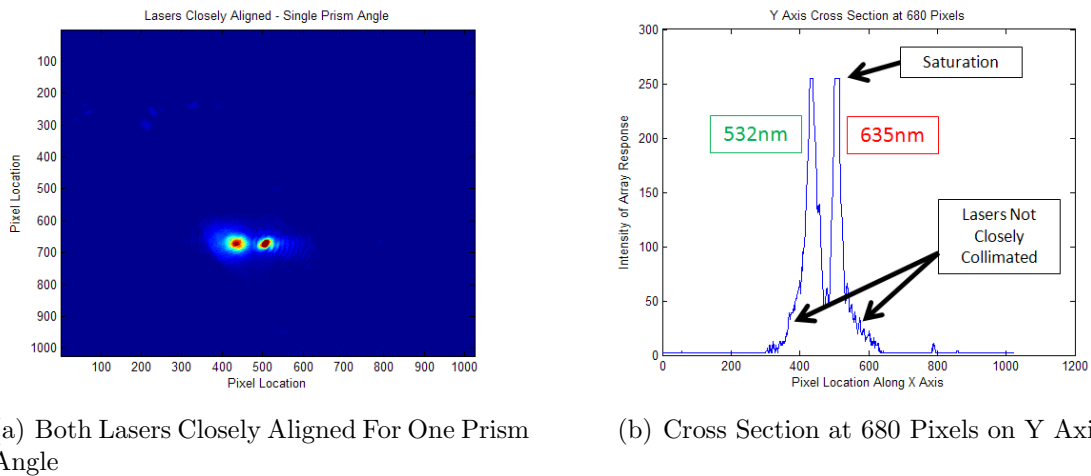


Figure 5.8: Array Saturation and Imperfect Collimation

Both of these issues should not be present in the on-board laser calibration system for CTE_x. To prevent saturation, 4.0 and 5.0 optical density filters will be used to prevent over saturation of the array in addition to manipulating the exposure time. To lower

the effect of beam dispersion, on-board lasers will be better collimated and introduced directly at the aperture giving the sources very little distance to diverge prior to the array.

These errors in the lab experiment provided some results for the first goal of obtaining knowledge of laser particulars that would affect calibration of CTE_x, but even with the errors, the second goal of the experiment, the effect of misalignment of the calibration lasers when introduced close to the aperture, is still able to be demonstrated without recollecting the data. Figure 5.9 represents four of the images at 90 degree prism rotation angle intervals that were taken with the laser sources closely aligned and overlaid. As expected, the centers of rotation are close to being coincident, since care was taken to align the lasers to within 0.01 degrees of parallel. The projected rotational path of each source is depicted by the ellipses.

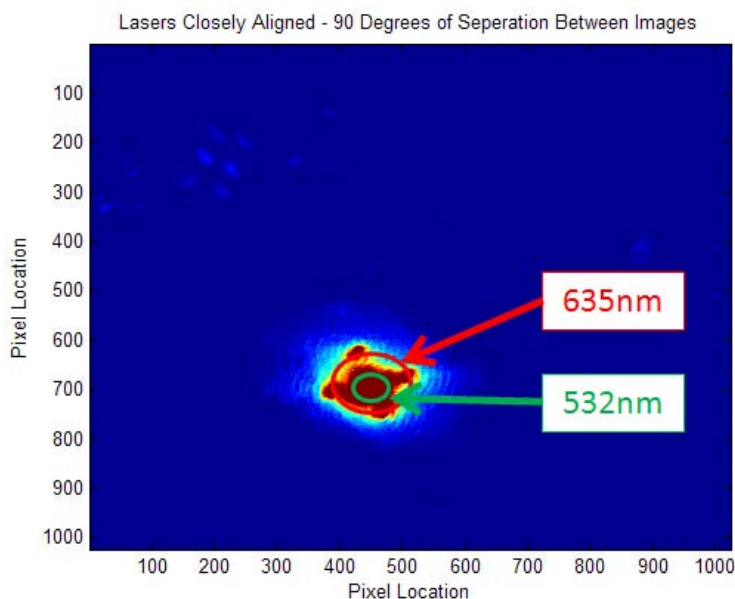
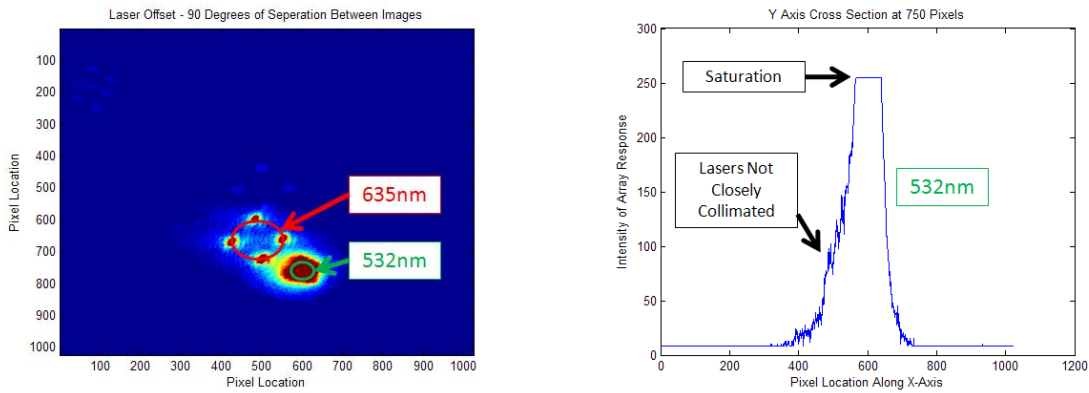


Figure 5.9: Lasers Closely Aligned Showing Coincident Centers of Rotation for Four Prism Rotational Angles

Figure 5.10 represents four of the images at 90 degree prism rotation angle intervals that were taken of the lasers offset at 0.02 degrees from parallel with a +/- error of 0.01 degrees overlaid. The centers of rotation for each source wavelength are not coincident as expected. This test, along with the previous image, confirms that the alignment between the laser sources is closely tied to the location of the centers of rotation for each source.

The image on the right of Figure 5.10 is a cross section of the 532 nm source showing the saturation occurring at its center of rotation due to imperfect collimation and 532 nm being close to the undeviated wavelength of 550 nm.



(a) Both Lasers Offset For Four Prism Rotational Angles

(b) Saturation Profile For Green Laser at 750 Pixels on Y Axis

Figure 5.10: Lasers Offset Showing Mis-Aligned Centers of Rotation

With the effect of the alignment of the calibration lasers shown on the center of rotation, it is necessary to define how close the calibration lasers must be aligned to parallel. If the centers of rotation are offset, a simple matlab code can be used to locate the center of each wavelength circle or ellipse and then shift the center of rotations to a common point in order to obtain the accurate calibration values. So, the lasers do not have to be perfectly parallel to each other because they can be digitally realigned. However, all the lasers must be aligned within 0.05 degrees of each other, because this is the field of view of the telescope. Once aligned within 0.05 degrees of each other, the laser diode mount with all four diodes should be aligned as close as possible to the center of the field of view, but this does not have to be precise, because the slow steering mirror can provide ± 8 degrees of correction.

5.5 Results

5.5.1 Procedures. Figure 5.11 provides an overview of the initial alignment, focusing and calibration procedure for CTE_x upon start of initial operations from the JEM. This procedure flows in a logical order from top to bottom and intentionally contains redundant procedures. The pixels are characterized using the camera's internal

shutter and the on-board LEDs to understand each pixel’s blackout noise and gain, and can be used to level the pixel gains. The laser diodes will be used to determine changes in offset, spectral spread and undeviated wavelengths resulting from launch and installation on the JEM as explained in Section 5.4 and Figure 5.2. The next procedure after opening the aperture door is the use of Earth-based targets for external calibration as discussed in Subsection 5.4.2. The pixel gain correction will use one of the six uniform USGS pseudo-invariant sites to level the pixel gain prior to imaging a sodium street light to ensure focus optimization as discussed in Section 5.2. Vicarious spectral calibration will be done looking for the atmospheric oxygen absorptions for the A and B bands, followed by a final radiometric characterization using the LSpec Frenchmann Flat site discussed in Subsection 5.4.2. After the initial calibration procedure, the laser diodes will only be utilized to troubleshoot any anomalies. If the aperture door remains closed for an extended period, the laser diodes could be used to monitor calibration trending in place of opening the aperture door and using the filter wheel.

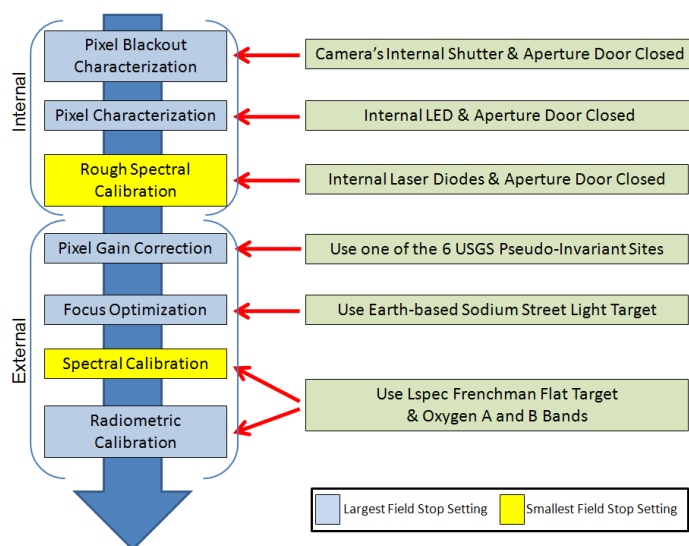


Figure 5.11: Theoretical CTEX On-Orbit Initial Calibration Flow Chart

Figure 5.12 provides a flow chart of the on-orbit maintenance calibration procedures. There are two procedures, an absolute calibration and a calibration trending. The calibration trending will be used routinely to monitor calibration trends and give an indication of when an absolute calibration is required. The absolute calibration procedure will be utilized as required.

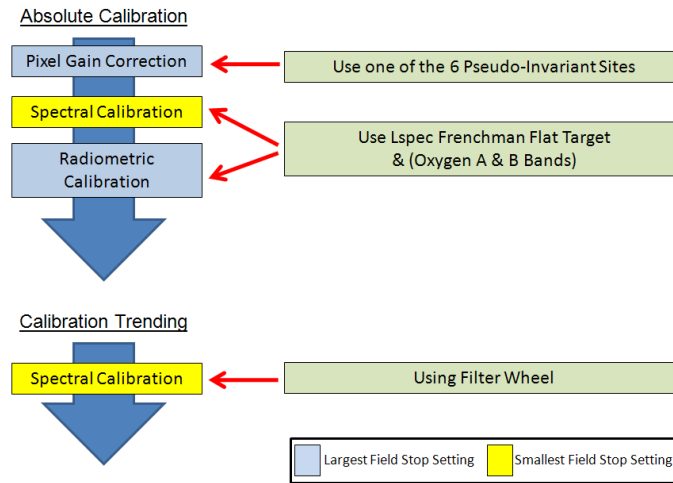


Figure 5.12: Theoretical CTEX On-Orbit Maintenance Calibration Flow Chart

5.5.2 *Design Requirements.* The following section outlines design requirements that were developed through this section for alignment and calibration subsystems. Where possible, equipment components were selected from vendors for inclusion.

The telescope design was covered in Chapter Four, but it is important to recognize some of the design features as part of this section. For maintaining the alignment of the OAPs, EPO-TEK 320 epoxy will be utilized to secure the adjustment screws on the OAPs once the telescope is aligned. One of the field stop settings will be as close as possible to one spatial pixel for use in calibration. A backup focus target will be included on the field stop mount.

Four on-board laser diode calibration sources will be included in the design of the aperture door. The four sources will be positioned on a thermally conductive raised mount oriented in the direction of the slow steering mirror of the telescope. If space limitations prevent this location then the laser diode sources may be positioned differently with a mirror on the aperture door to correctly direct the laser sources into the main aperture. All four lasers must be aligned within 0.05 degrees of each other.

For assembly of the laser diodes, the following parts are suggested for inclusion during fabrication.

- 1 x Sony 405nm Laser Diode (5mW)

- 1 x Nichia 445nm Laser Diode (50mW)
- 1 x Sanyo 670nm Laser Diode (5mW)
- 1 x Opnext 852nm Laser Diode (50mW)
- 4 x Optima 5.6mm LDM 1100 Kits (Laser Diode Mounts)
- 4 x Optima 5.6mm ADP 9056 Kits (Laser Diode Collimation Optics)
- 1 x Optima Heat Sink Compound
- 2 x 4.0 Neutral Density Filter (0.5 inch diameter)
- 2 x 5.0 Neutral Density Filter (0.5 inch diameter)
- 4 x IcHaus iC-WKN (CW Laser Diode Driver)

Due to the low power of the laser diodes, a thermal control system may not be required. However, short of experimenting to confirm or deny this the main components of the thermal control system for each diode is listed below.

- 4 x Laird Technologies (Optotec) Thermoelectric Coolers
- 4 x Linear Technologies (LTC1923) TEC Controller
- 4 x Thermoresistors

The secondary on-board calibration source requires a filter wheel with several narrow bandwidth or multi-bandwidth filters. There are numerous space-qualified filter wheels that satisfy the requirements, so there is no need to narrow the selection at this time until assembly of the imager due to unknown volume constraints. As far as the filters, they will be utilized for two purposes; one for calibration trending and another to filter uniform scenes like vegetation, etc, in order to limit artifacts in the scene. The issue of what filters are required to filter uniform scenes has not been looked at yet, but will be the driving factor in the determination of what filters to incorporate in the filter wheel.

The final part for the internal calibration system are the LEDs for the aperture door to characterize the camera's pixels. The selected LEDs are 525 nm, which is close to the theoretical undeviated wavelength for the prism at 550 nm.

- 3 x OPTEK OVGL Series 525nm Green LEDs

VI. Conclusions

The following chapter contains an overview and conclusions for each research topic investigated as part of this thesis as well as proposed future research topics. It is organized into five sections: Ground-Based CTE_x Structure; Telescope Design Review; Focus, Alignment and Calibration; Proposed Future Work; and Final Conclusions.

6.1 *Ground-Based CTE_x Structure*

In Chapter Three, a structure was designed to allow a ground-based CTE_x to be built and tested as a risk mitigation measure for the construction and testing of the space-based CTE_x. The driving requirement for the structure was not only to mount and support all components, but to have no structural natural frequencies within the range of excitation frequencies that the prism motor/encoder could generate (spin rate). The design methodology used finite element eigenvalue analysis to evaluate possible structural configurations. Chapter Three detailed the evolution of the ground-based CTE_x structural design up to fabrication.

Figure 6.1 is a photograph of the completed ground-based CTE_x instrument. The structure was constructed by the AFIT model shop using the design generated in Chapter Three. The ground-based CTE_x was constructed over the course of a week. Upon completion, the structure was turned over to the AFIT Physics Department for final assembly and testing.



Figure 6.1: Constructed Portable Ground-Based CTE_x Imager [18]

The ground-based CTE_x testing was completed. No structural or vibrational issues were experienced during the testing, thus validating the design methodology using finite element modeling and eigenvalue analysis. The results of the ground-based CTE_x are published in a master's thesis titled *Development and Characterization of a Field-Deployable Fast Chromotomographic Imager* by O'Dell [18].

6.2 Telescope Design Review

In Chapter Four, a design review of a proposed off-axis Mersenne telescope by RC Optical Systems (RCOS) for the space-based CTE_x was conducted. RCOS was contracted by AFIT to build the space-based CTE_x telescope. The design review and approval was a contract requirement and a critical step in the procurement process because design approval by AFIT triggered the start of parts procurement by the contractor and the disbursement of the first 25 percent payment of the contract to RCOS. The contract requirement to approve the drawings allowed AFIT to review the design prior to fabrication to ensure the design met all requirements and could feasibly survive launch and the space environment.

A critical part of Chapter Four and the design review was the creation of preliminary verification requirements. The preliminary verification requirements were derived from the contract. Through a conference call with RCOS, the list of verification requirements were balanced against RCOS's current progress. The finalized list of preliminary verification requirements narrowed down as part of this research were provided to RCOS as the briefing requirements for the telescope design review.

At the completion of the review, AFIT gave approval of the telescope design. The proposed design met all size, optical and mechanical requirements. Appropriate measures and considerations were being taken by the contractor to ensure the design's optical alignment and subcomponents could withstand the launch and space environments. The tentative scheduled date provided by RCOS for delivery of the telescope to AFIT is the first week in May 2010 [19].

6.3 Focus, Alignment and Calibration

In Chapter Five, a trade study was conducted for focusing, maintaining alignment and calibrating the space-based CTE_x. The result of this trade study was to identify the optimal solution that best addressed each one of these critical areas to enable high-quality images to be collected on orbit. The endstate was either the identification of a mechanism, procedure or both to accomplish each task.

Section 5.2 highlighted the focusing trade study for CTE_x. The only adjustable focus point in the CTE_x optical path is located on the imaging array. Vicarious focusing techniques were identified as the best method to focus the instrument on orbit. To use vicarious focusing techniques, a sodium street light will be imaged at night as CTE_x steps through a preselected range of focus settings. Once downloaded, the image with the sharpest sodium features will be select as the optimal setting. As a secondary method, a focus target will be included on the field aperture slide that can be inserted into the optical path to focus the array [17].

Section 5.3 identified alignment concerns for CTE_x during launch and on-orbit operations. The two main concerns were the alignment of the prism and collimated beam. However, since the prism design is still developing, only the alignment of the collimated beam was addressed. The alignment of the collimated beam could be maintained as long as the primary and secondary off-axis parabolic (OAP) mirrors remained parallel to each other. The telescope contractor selected EPO-TEK 820 epoxy to permanently lock the mirror adjustment screws in place once the telescope is aligned. The cementing of the adjustment screws will significantly increase the likelihood that the primary and secondary OAPs remain parallel throughout the life of CTE_x. Multiple methods could have been used but this was the most simple.

Section 5.4 detailed the trade study that was conducted into how to calibrate CTE_x on orbit. The result was three separate calibration sources. The first source will be a laser diode system on the inside of the CTE_x aperture door to provide an initial calibration method and for troubleshooting. The primary calibration method for CTE_x will be to use vicarious Earth-based targets. For absolute spectral calibration, CTE_x

will be able to utilize the oxygen A and B bands in the atmosphere. For radiometric calibration, two targets will be utilized: one to level the array pixel gain and the other for absolute radiometric calibration. Green LEDs will be included on the aperture cover for pixel characterization and to locate hot and dead pixels. The final calibration method identified for CTE_x was the inclusion of a filter wheel/slide for trending the spectral calibration while the aperture door remains open on orbit. This combination will ensure the integrity of CTE_x's calibration over the imager's lifetime and provide a known source for troubleshooting if required.

As a result, Chapter Five identified a tentative procedure for focusing and calibrating CTE_x on-orbit and the hardware components that need to be integrated into the design. Upon delivery of the telescope and fabrication of the imaging system, the calibration procedure will need to be verified as part of the ground characterization prior to launch. Since CTE_x represents a new type of imager, this verification of procedures is necessary to ensure the sequence is correctly identified as depicted in Figure 5.11 and Figure 5.12. The focusing, alignment and calibration procedures identified here are based on those of other successful space instruments, though CTE_x procedures and hardware will be unique, these studies give high confidence of success.

6.4 Proposed Future Work

The research contained in this thesis was completed to answer several of the design requirements for CTE_x as the design matures. Throughout the course of this research, several topics were identified that require further exploration and development. These identified topics are follow on research to the work that is contained in this document on the path toward a successful space experiment.

The first area that requires follow on research is the prism mount and encoder design. As the lead in the Physics Department for the prism design nears a conceptual optical design, input will be required on its mounting feasibility to ensure that the alignment of the prism can be maintained when subjected to known launch and operational loads. As mentioned in Section 5.3, the mounting of the prism was one of the two alignment concerns because shifts in the prism would cause changes in how the col-

lected image wavelengths were dispersed onto the array face and thus detrimental to the algorithm's ability to reconstruct a traditional hyperspectral cube. Small changes in the prism's alignment can be accounted for by calibrating CTE_x, but large changes in the alignment could be detrimental to the experiment. The reason that conceptual prism mounts need to be explored up front after the conceptual prism design is to ensure the prism's alignment can be maintained before finalizing the design. To develop a prism mount, several preliminary items are required. The first is a conceptual prism design. Another key component is the selection of the rotation stage/encoder design. Contrary to previous CTE_x evolutions, both prisms will have their own rotation stage/encoder to allow them to be rotated together to obtain spectral data or counter rotated to obtain a traditional spatial image. Once the prism design and rotation stage/encoder mechanism are selected, the mounting options must be researched.

The second area that requires follow on research is the field stop design. The aperture shapes and sizes for the field stop are being designed by the lead in the Physics Department. However, several other events must occur. A focus target needs to be selected from COTS items for inclusion at the end of the field stop to provide a secondary focus means. The bar containing the apertures and focus target must be designed and manufactured by the AFIT modeling shop. The final part of the field stop design is the procurement of the Physik Instruments M-122 Precision Micro-Translation Stage recommended by RCOS as the optimal linear slide for the field stop.

The third area that requires follow on research is the fabrication of the optical enclosure and baffling. The telescope contractor will provide the CAD models for these items, but it will be up to AFIT to fabricate them. The items will require the procurement of aluminum sheet and fabrication by the AFIT modeling shop.

The final area that requires follow on research is the selection of filters and a filter wheel/slide for inclusion in CTE_x's optical package as mentioned in Section 5.5. As mentioned in this section, the filters will serve two purposes: trending calibration and filtering uniform spectral scenes. Chromotomography has technological difficulties exploiting very uniform spectral scenes due to noise when the image is deconvolved. Two methods can be used to remove the noise in very uniform spectral scenes: increasing the

number of prism rotational angles used per revolution and using a filter in the optical path to remove the spectral uniformity such as vegetation. The selection of the bandpasses for the filters is not determined by the calibration trending use, but by the requirement to eliminate noise in uniform scenes. Selection of the bandpass filters will need to be completed by the lead in the Physics Department first. The next requirement will be to select and procure a filter wheel or linear filter slide that can accommodate the required bandpass filters and fit in the volume constraints of CTE_x's optical package.

6.5 Final Conclusions

The chromotomographic hyperspectral imaging experiment at AFIT will demonstrate a new technology for the imaging of static scenes and transient combustion events. The lab and ground-based experiments were already completed successfully and verified the usefulness of a chromotomographic hyperspectral imager. The data obtained from the ground-based CTE_x was presented at the Department of Defense 2009 Space Experiments Review Board. The design and construction of the space-based CTE_x is underway at this time with a manifest for launch expected in the near future.

The work contained in this thesis contributed significantly to the overall effort to demonstrate the capabilities of a chromotomographic hyperspectral imager. It contributed to the successful demonstration of a ground-based CTE_x as well as to the overall initial design effort for the space-based CTE_x. With further research and design, the space-based CTE_x stands a very good chance to get off the ground and prove the usefulness of a chromotomographic hyperspectral imager for imaging static and transient combustion scenes.

Appendix A. Airborne/Spaceborne Spectral Imagers As Of May 2007 [1]

Chapter 5 – OVERVIEW OF CURRENTLY AVAILABLE IMAGERS

5.1 AIRBORNE / SPACEBORNE SYSTEMS [1,9]

Name	Full Name	Manufacturer Country	Number of Bands	Spectral Range (µm)	Band Width at FWHM (nm)
AAHIS	Advanced Airborne Hyperspectral Imaging System	SETS Technology	288	0.432 – 0.832	6
AHI	Airborne Hyperspectral Imager	Hawaii Institute of Geophysics and Planetology	256	7.5 – 11.7	100
AHS	Airborne Hyperspectral Scanner	Daedalus Enterprise Inc.	48	0.433 – 12.70	
AIP	Airborne Instrument Program	Lockheed USA		2.00 – 6.40	
AIS-1	Airborne Imaging Spectrometer	NASA, JPL USA	128	0.90 – 2.10 1.20 – 2.40	9.3 10.6
AMSS	Airborne Multispectral Scanner MK-II	Geoscan Pty Ltd.	46	0.50 – 12.00	
ARES		USA	75	2.00 – 6.50	
ARIES	Australian Resource Information and Environment Satellite	Australia	128	0.40 – 2.50	
APEX	Airborne Prism Experiment		Programmable to a max of 300	0.38 – 2.50	10
CHRISS	Compact High Resolution Imaging Spectrograph Sensor	Science Applications Int. Corp. (SAIC) USA	40	0.43 – 0.87	
CIS	Chinese Imaging Spectrometer	Shanghai Institute of Technical Physics China	91	0.40 – 12.50	
DAIS 21115	Digital Airborne Imaging Spectrometer	GER Corp. Germany	211	0.40 – 12.00	
DAIS 3715	Digital Airborne Imaging Spectrometer	GER Corp. Germany	37	0.40 – 12.00	
DAIS 7915	Digital Airborne Imaging Spectrometer	GER Corp. Germany	79	0.40 – 12.00	
DAIS 16115	Digital Airborne Imaging Spectrometer	GER Corp. Germany	160	0.40 – 12.00	

OVERVIEW OF CURRENTLY AVAILABLE IMAGERS

Name	Full Name	Manufacturer Country	Number of Bands	Spectral Range (µm)	Band Width at FWHM (nm)
EART EXPLORER		ESA	202 (?)	(3)10 – 1000	
EO-1		USA	7	0.43 – 2.35	
EPS-A	Environmental Probe System	Germany	32	0.40 – 12.00	
EPS-H	Environmental Probe System	Germany	76 * 32 32 12	0.43 – 1.05 * 1.50 – 1.80 2.00 – 2.50 8.00 – 12.00	*Customised according user requirements
FLI/PMI	Fluorescence Line Imager / Programmable Multispectral Imager	Moniteq Ltd.	228	0.43 – 0.805	
FTVFHSI	Fourier Transform Visible Hyperspectral Imager	Kestrel Corp., FIT	256	0.44 – 1.15	
GERIS	Geophysical and Environmental Research Imaging Spectrometer	Germany	63	0.40 – 2.50	
HIRIS	High Resolution Imaging Spectrometer	USA	192	0.40 – 2.50	
HYDICE	Hyperspectral Digital Imagery Collection Experiment	USA	210	0.40 – 2.50	7.6 – 14.9
HYMAP		Integrated Spectronics Australia	126	0.45 – 2.50	15 – 20
HYPERION		TRW	220	0.40 – 2.5	10
IISRB	Infrared Imaging Spectrometer	Bomen	1720	3.50 – 5.00	
IMSS	Image Multispectral Sensing	Pacific Advanced Technology	320	2.00 – 5.00	
IRIS	Infrared Imaging Spectrometer	ERIM USA	256	2.00 – 15.00	
ISM	Imaging Spectroscopic Mapper	DESPA	128	0.80 – 3.20	
LIVTIRS 1	Livermore Imaging Fourier Imaging Spectrometer	Lawrence Livermore USA		3.00 – 5.00	



OVERVIEW OF CURRENTLY AVAILABLE IMAGERS

Name	Full Name	Manufacturer Country	Number of Bands	Spectral Range (µm)	Band Width at FWHM (nm)
LIVTIRS 2	Livermore Imaging Fourier Imaging Spectrometer	Lawrence Livermore USA		8.00 – 12.00	
MAIS	Modular Airborne Imaging System	Shanghai Institute of Technical Physics China	71	0.44 – 11.8	
MAS	Modis Airborne Simulator	Daedalus Enterprise Inc. USA	50	0.53 – 14.50	
MERIS	Medium Resolution Imaging Spectrometer	ESA	15	0.40 – 1.05	
MIDIS	Multiband Identification and Discrimination Imaging Spectroradiometer	Surface Optics Corp., JPL, USA	256	0.40 – 30.00	
MIVIS	Multispectral Infrared and Visible Imaging Spectrometer	Daedalus Enterprise Inc. USA	102	0.43 – 12.70	
MODIS	Moderate Resolution Imaging Spectrometer	NASA USA	36	0.41 – 14.24	
OMIS	Operative Modular Airborne Imaging Spectrometer		128	0.46 – 12.50	
PROBE-1			100 – 200	0.44 – 2.54	11 – 18
ROSIS	Reflective Optics System Imaging Spectrometer	DLR, GKSS, MBB Germany	128	0.45 – 0.85	5
SASI	Shortwave Infrared Airborne Spectrographic Sensor		160	0.85 – 2.45	10
SFSI	SWIR Full Spectrographic Imager	CCRS Canada	122	1.20 – 2.40	10.3
SMIFTS	Spatially modulated Imaging Fourier Transform	Hawaii Institute of Geophysics USA	75	1.00 – 5.00	
SSTI HSI	Small Satellite Technology Initiative Hyperspectral Imager	TRW Inc. USA	384	0.40 – 2.50	
TRWIS III	TRW Imaging Spectrometer	TRW Inc USA.	384	0.30 – 2.50	

OVERVIEW OF CURRENTLY AVAILABLE IMAGERS

Name	Full Name	Manufacturer Country	Number of Bands	Spectral Range (μm)	Band Width at FWHM (nm)
VIFIS	Variable Interference Filter Imaging Spectrometer	University of Dundee	60	0.44 – 0.89	10
VIMS-V	Visible Infrared Mapping Spectrometer	ASI	512	0.30 – 1.05	
WIS	Wedge Imaging Spectrometer	Hughes St. Barbara Research Center USA	170	0.40 – 2.50	
WARFIGHTER (WF-1)		Phillips Laboratory USA	280	0.45 – 5.00	

5.2 GROUND BASED / HAND HELD SYSTEMS

Name	Manufacturer Country	Number of Bands	Spectral Range (μm)	Technology
GALAAD (Prototype)	ATIS France		7.0 – 14.0	Double grating with needle mask
CTHIS LWIR (CromoTomographic Hyperspectral Imaging Spectrometer)	Solid State Scientific Corporation USA	40	6.5 – 11.0	Rotating prism
CTHIS MWIR (CromoTomographic Hyperspectral Imaging Spectrometer)	Solid State Scientific Corporation USA	64	2.7 – 5.0	Rotating prism
ImSpector N10	Spectral Imaging Ltd. (Specim) Finland	Spectral resol 5.0 nm	0.7 – 1.0	Prism-Grating-Prism (PGP)
ImSpector N17	Spectral Imaging Ltd. (Specim) Finland	Spectral resol 10.0 nm	0.9 – 1.75	Prism-Grating-Prism (PGP)
Orion IR Multispectral Imager (SWIR, MWIR, LWIR models)	CEDIP France	4 or 6 per model	SWIR MWIR LWIR customized	Filter wheel



OVERVIEW OF CURRENTLY AVAILABLE IMAGERS

Name	Manufacturer Country	Number of Bands	Spectral Range (μm)	Technology
Sherlock LWIR	Pacific Advanced Technology USA	Spectral resol. 3 nm at $\lambda = 3.0\mu\text{m}$	8.0 – 10.5	IMSS (Image Multi Spectral Sensing)
Sherlock MWIR	Pacific Advanced Technology USA	Spectral resol. 33 nm at $\lambda = 8.0\mu\text{m}$	3.0 – 5.0	IMSS (Image Multi Spectral Sensing)

Appendix B. Verification Matrix

Appendix C. Telescope Minimum Design Requirements [2]

**MINIMUM REQUIREMENTS
FOR
SPACE IMAGING COMPONENT
SPACE IMAGING AND POWER LABORATORY**

GENERAL

This specification describes the performance, hardware and services to be provided in conjunction with a space-rated telescope imaging system. The requirement is for a system consisting of mirror optics, beam and focus controls, prism rotation stage, and an imaging device. The system is intended to be used for a space-based hyperspectral imaging system that requires a 1-inch diameter collimated input beam to the prism prior to image acquisition. The telescope must also include a field stop to limit the field of view (the image must not fill the entire focal plane). The telescope, control devices, and imaging camera shall all be manufactured as one unit. The system shall fit inside a 75 x 80 x 185 cm box, with desired dimensions of 60 x 30 x 110 cm.

The materials and component parts shall be of good commercial quality, consistent with the performance requirements of the components for spaceflight.

Workmanship shall be consistent with best commercial practice, and must be able to achieve manned space qualification.

The equipment shall be fully tested and meet all specifications prior to shipment.

OVERALL DIMENSIONS

The system shall fit inside a 75 x 80 x 185 cm box, with desired dimensions of 60 x 30 x 110 cm, and meet all optical, steering, space qualification, and other requirements. It is intended that the vendor will prepare a detailed engineering design of the requested system after receiving a contract award. The purchaser will review the design package in a timely manner. Once agreement is reached on all issues brought out during the review, the purchaser shall approve the design and the vendor will proceed with fabrication.

PERFORMANCE SPECIFICATIONS

Collecting Aperture	Largest possible subject to the geometric constraints, a field stop to control field of view (FOV), a collimated 1-inch diameter beam into a prism rotation stage immediately before the imager, and the additional constraints below.
Collecting Aperture Conditions:	Given a nominal target range of 350 km, a ground sample distance (GSD) of 10m is required based on a 20 micron pixel pitch.
Image Quality:	Two times diffraction-limited performance or better. Zero chromatic aberration.
	The collimated beam diameter (at the telescope output) of 0.95 inches.

Field Stop:	<p>The field stop should limit the telescope field of view to 0.05 degrees. An adjustable field stop is desirable.</p> <p>For a field stop at the prime focus, this requires a 0.88mm (square) clear aperture. Outer dimensions (blocking portion of stop) should be at least 7.2mm)</p>
Beam Steering:	<p>Five degrees of beam steering are desired. The system must steer in the along-track direction and dwell on a spot as the system flies over (direction of flight is parallel to the 185cm dimension of the box).</p> <p>Ability to steer beam +/- 5 degrees at an angle rate of 100 mrad/sec.</p>
Fast Steering Mirror:	<p>To compensate for jitter, a fast-steering mirror somewhere in the system (before the field stop) is desirable. Any potential location should be considered, including at the secondary mirror.</p>
Focus Control:	<p>Active focus control for the system must be included.</p>
Camera:	<p>Phantom v12.1 or comparable (1 kHz frame rate or higher, 768 x 768 pixel or greater readout area).</p>
Interfaces:	<p>The final system need not be accompanied by a functioning control software suite that controls all components (though it is desirable – bid as an option), but the system must be accompanied by the necessary motors/encoders/piezos/etc to perform all tasks.</p>

IMAGING SYSTEM CONSTRUCTION

All component parts of the chamber will be manufactured in accordance with industry best practices. Documentation will be maintained in accordance with the NASA Technical Standards Program (<http://standards.nasa.gov>) and the NASA Electronic Parts and Packaging Program (<http://nepp.nasa.gov/npsl/index.htm>) for human spaceflight systems.

The final system must be capable of space qualification testing according to the NASA Technical Standards Program and the NASA Electronic Parts and Packaging Program. The system must also be capable of surviving a space launch and operating successfully in an exposed space environment.

PREPARATION FOR MANUFACTURING

Adequate design details to consist of drawings and models shall be provided to document the performance of the design prior to manufacturing. These shall consist of a general layout illustrating dimensions of the system, documentation of the expected performance of the system, and analysis of ability of the system to meet all requirements. The purchaser will review the

package in a timely manner. Once agreement is reached on all issues brought out during the review, the purchaser shall approve the package and the vendor will proceed with fabrication.

DELIVERY

The company shall disassemble the imaging system after factory testing as needed to ensure safe shipping, and provide assembly and re-test the system at WPAFB.

OPERATION AND MAINTENANCE MANUAL

An Operation and Maintenance Manual will be provided. The manual will consist of the following:

- ... Electrical drawings.
- ... Major component vendor literature.
- ... General arrangement drawing or descriptive literature.
- ... Calibration instructions.
- ... Operating instructions.
- ... Programming routines.
- ... Test documentation showing system meets requirements.

Appendix D. RCOS Selected Component Literature [3–8]

ADRS Series

Mechanical-Bearing Rotary Stage

High torque output, direct-drive brushless servomotor

Cog-free slotless motor design for outstanding velocity stability

Direct coupled, high-accuracy rotary encoder

Ultra-low-profile minimizes working height



Aerotech's ADRS series with its direct-drive technology and low profile provide a superior alternative to belt- and worm-drive stages.

Compact Package

The design of the ADRS series direct-drive rotary stage was optimized to minimize stage height. The low profile of the stage reduces the effective working height of the system minimizing "stack-up" related errors. In addition to the low overall height, the ADRS series provides a clear aperture that can be used for product feed-through or laser beam delivery.

Brushless Direct-Drive

To maximize positioning performance, the ADRS series utilizes direct-drive brushless motor technology. Direct-drive technology is optimized for 24/7 production environments, as there are no brushes to replace and no gear trains or belts to maintain. Direct drive also provides quicker acceleration and higher top speeds than gear- or belt-driven mechanisms, yielding higher total overall throughput.

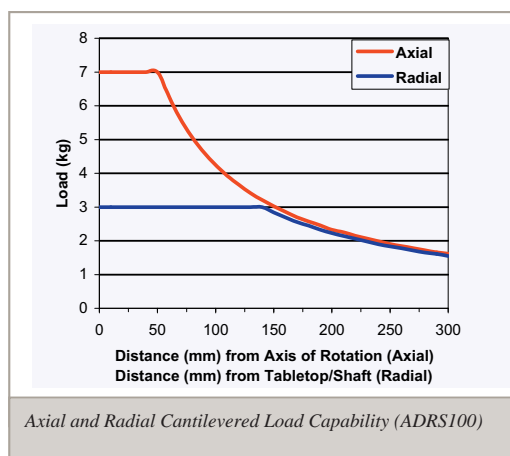
The low maintenance and high-throughput characteristics of the ADRS series provide a stage that yields the lowest total cost of ownership.

Slotless Motor

The ADRS series uses a slotless stator design that eliminates torque ripple. This motor technology provides ultra-smooth velocity stability comparable to a high-quality DC brush motor without all the DC motor's inherent maintenance requirements. Since the slotless motor is directly coupled to the tabletop, velocity disturbances created by toothed belt drives or worm gears are eliminated.

Multiple Configurations

The ADRS series is available in 100 mm, 150 mm, and 200 mm versions. Each stage has options for different motor windings to better match the stage to different operating conditions. The -B winding option provides the highest possible speed operation for a given available bus voltage, while the -A winding gives greater output torque for comparable current levels. Metric and "English" pattern tabletops are available and slotted mounting holes enable attachment to 25 mm and 1 inch hole pattern breadboards. The tabletop of the ADRS series has a labyrinth seal that protects the bearings and encoder from contamination. An optional shaft end seal is available for applications where the bottom of the stage is exposed to contamination.



Axial and Radial Cantilevered Load Capability (ADRS100)

ADRS Series SPECIFICATIONS

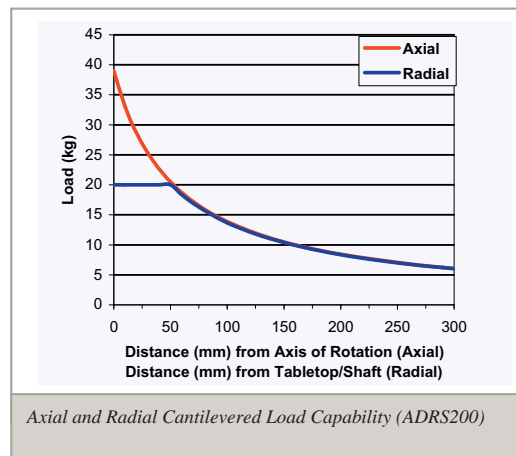
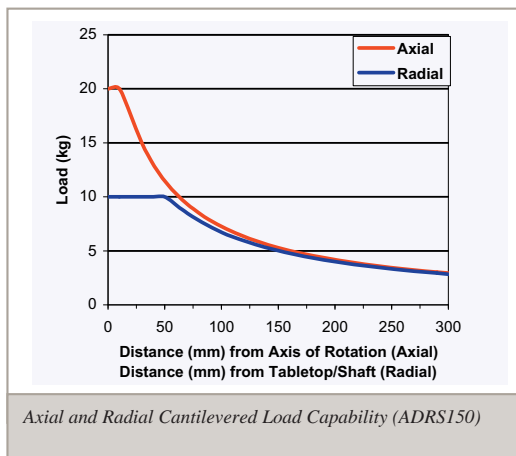
ADRS Series		ADRS-100		ADRS-150		ADRS-200	
Tabletop Diameter		95 mm		140 mm		190 mm	
Aperture		6 mm		15 mm		25 mm	
Motor (-A/-B)		S-76-35-A	S-76-35-B	S-130-39-A	S-130-39-B	S-180-44-A	S-180-44-B
Continuous Current, Stall	A_{pk}	2	4	3.8	7.6	2.7	5.3
	A_{rms}	1.4	2.8	2.7	5.4	1.9	3.8
Bus Voltage		320	160	320	160	320	160
Resolution		0.87-87.3 μ rad (0.18-18 arc sec)		0.315-31.5 μ rad (0.065-6.5 arc sec)			
Max Speed ⁽¹⁾		1500 rpm		600 rpm	400 rpm		
Accuracy	Uncalibrated			388 μ rad (80 arc sec)			
	Calibrated ⁽²⁾	29.1 μ rad (6 arc sec)		48.5 μ rad (10 arc sec)		48.5 μ rad (10 arc sec)	
Repeatability		14.6 μ rad (3 arc sec)		19.4 μ rad (4 arc sec)		19.4 μ rad (4 arc sec)	
Max Load ⁽³⁾	Axial	7 kg		20 kg		40 kg	
	Radial	3 kg		10 kg		20 kg	
Axial Error Motion ⁽⁴⁾		2 μ m		5 μ m		5 μ m	
Radial Error Motion ⁽⁴⁾		3 μ m		5 μ m		5 μ m	
Tilt Error Motion		48.5 μ rad (10 arc sec)		97 μ rad (20 arc sec)		97 μ rad (20 arc sec)	
Inertia		Unloaded		0.00038 kg-m ²		0.00242 kg-m ²	
Total Mass		2.0 kg		4.3 kg		7.6 kg	
Finish	Tabletop			Hardcoat			
	Stage			Black Anodize			

Notes:

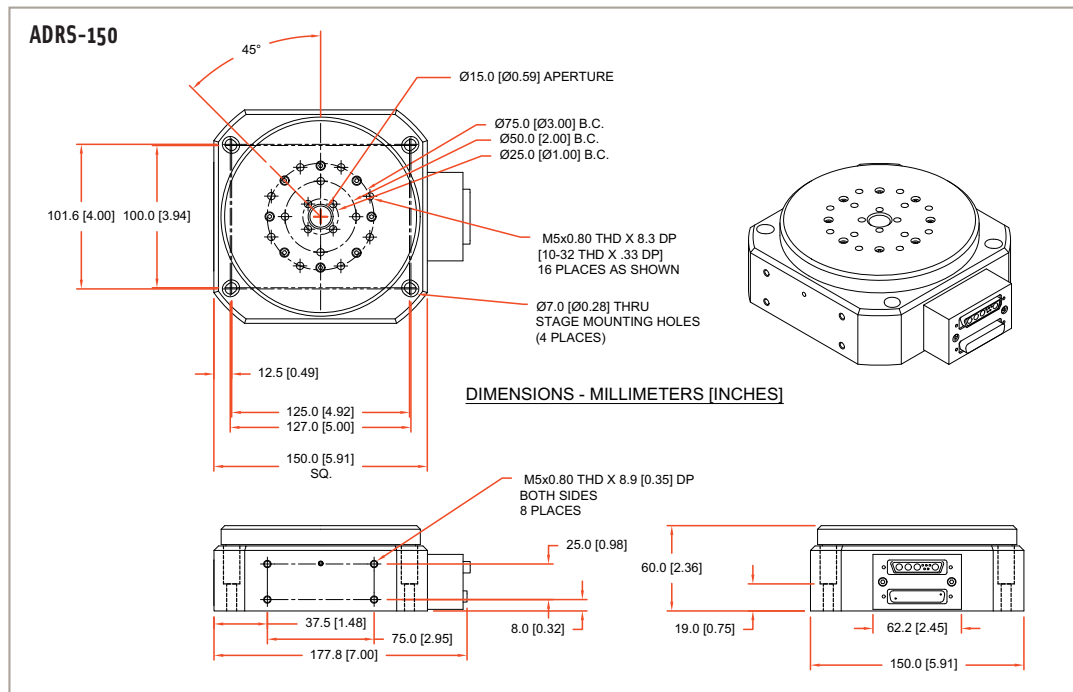
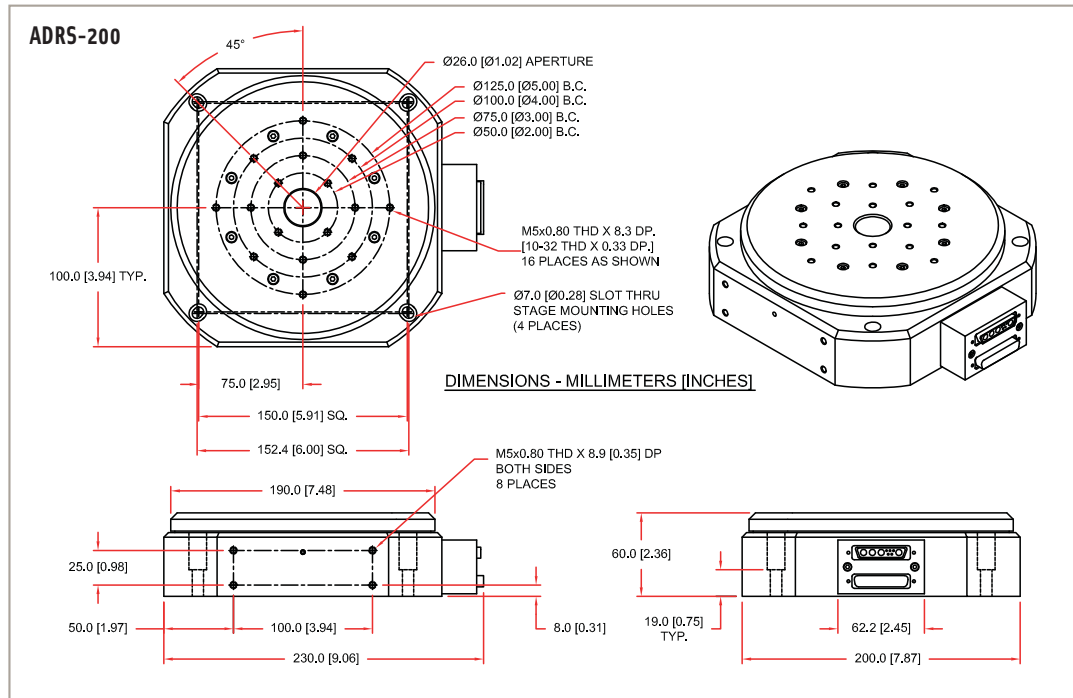
- Maximum speed is based on stage capability. Actual speed may depend on encoder resolution, load, amplifier bus voltage, and motor. See the S-series rotary motor for more information.
- With HALAR.
- Maximum loads are mutually exclusive.
- For the ADRS-100, error motion specifications are below 700 rpm. Above 700 rpm, the max radial error is 5 microns. Errors measured 50 mm (2 in) above the tabletop.

ADRS Maximum Encoder Frequency

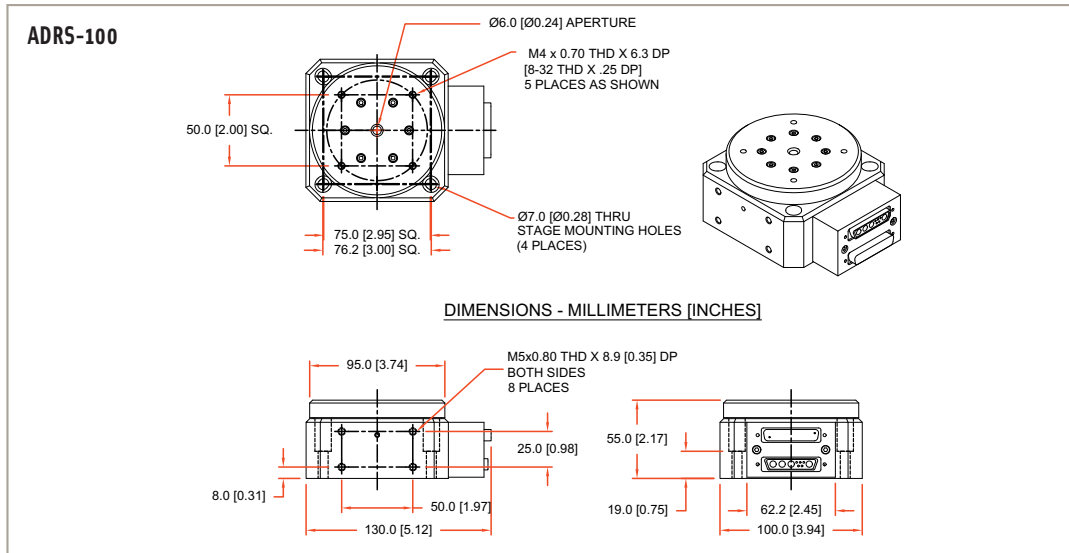
Resolution-Speed	ADRS-100	ADRS-150	ADRS-200
AS/X5/X10	1500 rpm	600 rpm	600 rpm
X25	1067 rpm	384 rpm	384 rpm
X50	533 rpm	192 rpm	192 rpm



ADRS Series DIMENSIONS



ADRS Series DIMENSIONS and ORDERING INFORMATION



Ordering Example

ADRS	-200	-M	-A	-AS	-S
Series	Width (mm)	Mounting Pattern	Winding Option	Position Transducer	Construction Options
	-100	-M	-A	-AS	-S
	-150	-U	-B	-X	
	-200				

ADRS Series Direct-Drive Rotary Stage

ADRS-100	100 mm wide direct-drive rotary stage with 1.8 N-m peak torque output
ADRS-150	150 mm wide direct-drive rotary stage with 11.7 N-m peak torque output
ADRS-200	200 mm wide direct-drive rotary stage with 30 N-m peak torque output

Mounting Pattern

-M	Metric-dimension mounting pattern and holes
-U	English-dimension mounting pattern and holes

Winding Options

-A	Low speed, high torque-constant winding option
-B	High speed, low torque-constant winding option

Position Transducer

-AS	Standard feedback device, 1 Vpp sine wave output, 10,000 cycles per rev on ADRS-200/150, 3600 cycles per rev on ADRS-100
-X5	Square wave digital output, 50,000 cycles per rev on ADRS-200/150 and 18,000 cycles per rev on ADRS-100
-X10	Square wave digital output, 100,000 cycles per rev on ADRS-200/150 and 36,000 cycles per rev on ADRS-100
-X25	Square wave digital output, 250,000 cycles per rev on ADRS-200/150 and 90,000 cycles per rev on ADRS-100
-X50	Square wave digital output, 500,000 cycles per rev on ADRS-200/150 and 180,000 cycles per rev on ADRS-100

Note: Digital output encoder signals are synthesized with a 16 MHz clock. Care must be taken to ensure that the encoder sample rate on the controller is at least 16 MHz or higher. Slower clock rates are available on request.

Construction Options (ADRS 150 & 200)

-S	Bottom shaft seal (not available on ADRS-100; ADRS-100 has an integral bottom labyrinth seal)
-NS	No bottom shaft seal

Ensemble™ HPe/HLe/CP/CL/MP

Networked, Panel-Mount Drives

Network drives through a high-speed serial interface to coordinate up to ten axes of motion

Select linear (HLe/CL) or pulse width modulation (HPe/CP/MP) amplifiers

Coordinate motion using up to five independent tasks

Drive and control linear or rotary brushless, DC brush servo, and micro-stepping motors

Command various motion types including: point-to-point, linear and circular interpolation, electronic gearing, and velocity profiling

Program in AeroBASIC™, Microsoft .NET (C#, VB.NET, and Managed C++), or LabVIEW®

Remotely command drives over Ethernet, USB, or RS-232 with an ASCII interface available for both Windows® and non-Windows® programs (including Linux)

Diagnose, tune, and program through an advanced Windows-based interface

UL listed, CE approved

The Ensemble™ is Aerotech's next-generation, multi-axis controller for moderate- to high-performance applications. Versatility, power, and affordability make the Ensemble ideal for applications from basic laboratory experimentation and general-purpose positioning to advanced OEM systems.

Versatile, Flexible, Stand-Alone Multi-Axis Control

Network multiple Ensemble HPe/HLe/CP/CL/MP combination controllers/drives for up to ten axes of coordinated motion, and seamlessly mix and match amplifiers (linear and PWM) and motor types (brush, brushless, and stepper) within the same positioning system using a common programming and control platform. High-



Clockwise from upper left: Ensemble HPe, Ensemble HLe, Ensemble CL, Ensemble MP, and Ensemble CP.

accuracy linear motor air-bearing stages can be directed from the same controller/drive running lower precision stages with servo or stepper motors. Each controller/drive can be reconfigured to accept different motors and feedback devices, allowing customers to adapt to changing system needs. Optional on-board encoder interpolation provides programmable axis resolution, including the ability to change interpolation (multiplication) values through software.

Powerful and Intuitive Programming

Monitor and control all aspects of the positioning system, no matter how complex, through the Ensemble GUI

Ensemble HPe/HLe/CP/CL/MP DESCRIPTION

Integrated Development Environment software. An Autotuning utility minimizes startup time by allowing easy optimization of motion axes. Functional programs that can be modified and used in customer applications are included in the online Help. Pre-coded LabVIEW® VIs, AeroBASIC™ programming functionality, .NET tools for C#, VB.NET, and managed C++, make the Ensemble even easier to use.

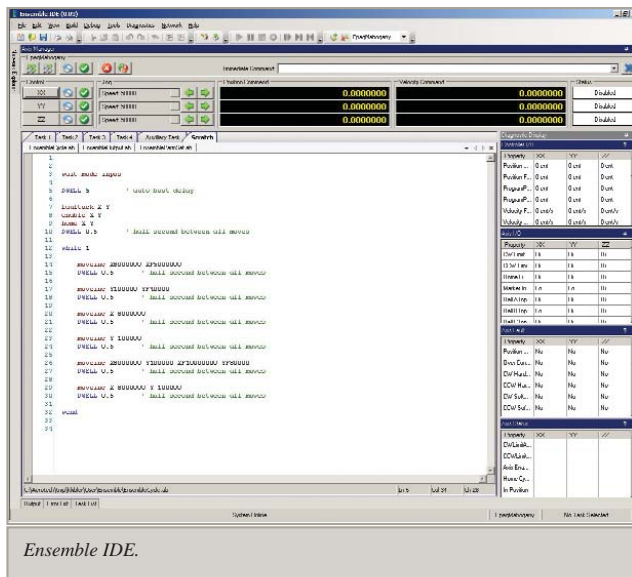
Advanced DSP Control

The processing power of a 225 MHz double precision, floating-point DSP supplies exceptional performance in a variety of applications including point-to-point motion, linear and circular interpolation, multi-axis error correction, 2D error mapping, direct commutation of linear and rotary brushless servomotors, and on-board servo autotuning. High-speed interrupts and data logging capabilities provide

a real-time link to external systems. The Ensemble HPe/HLe/CP/CL/MP controller/drive combination also offers high-speed position latching capability and single-, dual-, or triple-axis PSO (Position Synchronized Output), depending on model. Whether the requirement is simple point-to-point motion or complex velocity-profiled contours with output on the fly, Ensemble ensures peak performance for critical operations.

Enhancing a Legacy of Success

Ensemble carries forward a legacy of success that originated in Aerotech's A3200 and Soloist™ controllers. Enhanced capabilities make it an obvious choice for aggressive motion control applications. The Ensemble motion control architecture builds upon the Soloist™ intuitive graphical user interface, while improving multi-axis control through advanced features.



Ensemble IDE.

Ensemble HPe/HLe/CP/CL/MP COMPARISON



Ensemble HPe
Width: 99 mm
Height: 232.4 mm



Ensemble HLe
Width: 206.9 mm
Height: 234.3 mm



Ensemble CP
Width: 63.5 mm
Height: 198.2 mm



Ensemble CL
Width: 103.7 mm
Height: 265.2 mm



Ensemble MP
Width: 41.1 mm
Height: 141.2 mm

Ensemble Comparison Chart	Ensemble HPe	Ensemble HLe	Ensemble CP	Ensemble CL	Ensemble MP
PC Interface	Ethernet or USB				
Current Output, Peak	10-150 A	10-20 A	10-30 A	10 A	10 A
Current Output, Continuous	5-75 A	5-10 A	5-15 A	5 A	5 A
Bus Voltage	10-320 V	40-80 V	10-320 V	40 V	10-80 V
Amplifier Type	PWM	Linear	PWM	Linear	PWM
Input Type	2 or 3 Phase AC	2 Phase AC	2 Phase AC	2 Phase AC	DC
Motor Style	Brush, Brushless, Stepper				
Base I/O	4-DO/6-DI 1-AO/1-AI	4-DO/6-DI 1-AO/1-AI	4-DO/6-DI 1-AO/1-AI	4-DO/6-DI 1-AO/1-AI	1-AI
Additional I/O (Additional to Base I/O)	16-DO/16-DI 3-AO/3-AI	16-DO/16-DI 3-AO/3-AI	16-DO/16-DI 1-AO/1-AI	16-DO/16-DI 1-AO/1-AI	8-DO/8-DI 1-AO/1-AI
ESTOP Input	Yes	Yes	Yes	Yes	Yes
Brake Input Capable	Yes	Yes	Yes	Yes	Yes
Single Axis PSO ⁽¹⁾	Yes	Yes	Yes	Yes	Yes
Dual Axis PSO ⁽¹⁾	Yes	Yes	No	No	No
Triple Axis PSO ⁽¹⁾	Yes	Yes	No	No	No
Ethernet Capable for Third-Party I/O	Yes	Yes	No	No	No
Auxiliary Keep Alive	Yes	Yes	Yes	Yes	Yes

Notes:

1. PSO not available on Ensemble CP/MP when using integral MXU.

Ensemble HPe SPECIFICATIONS

Ensemble HPe	Units	10	20	30	50	75	100	150	
Output Voltage ⁽¹⁾	VDC	10-320 ⁽²⁾							
Peak Output Current (1 sec)	A _{pk}	10	20	30	50	75	100	150	
Continuous Output Current ⁽³⁾	A _{pk}	5	10	15	25	37	50	75	
Power Amplifier Bandwidth	kHz	Selectable Through Software							
PWM Switching Frequency	kHz	20							
Minimum Load Inductance	mH	0.1 @ 160 VDC (1.0 mH @ 320 VDC)							
Operating Temperature	°C	0 to 50							
Storage Temperature	°C	-30 to 85							
Weight	kg (lb)	2.36 (5.2)			6.64 (14.6)			11.06 (24.4)	
Maximum Shunt Regulator Dissipation	W	40 (Optional)		40	440	440	440	440	
Power Input	VAC	Single- or Three-Phase 7-240 VAC, 50-60 Hz ⁽⁴⁾							
Encoder Input Frequency	kHz	200 kHz Amplified Sine (For Onboard Multipliers), 40 MHz TTL Square Wave							
Current Loop Update Rate	kHz	20 kHz							
Servo Loop Update Rate	kHz	1 to 20 kHz							
Keep Alive/Auxiliary Power Supply ⁽⁵⁾	—	Optional							
Brake Output	—	Optional							
Position Synchronized Output	—	Single Axis Standard, Two/Three Axis Optional							
Digital Inputs	—	6 Optically-Isolated (2 High Speed)							
Digital Outputs	—	4 Optically-Isolated							
Analog Inputs	—	One 16-bit Differential							
Analog Outputs	—	One 16-bit Single-Ended							
Additional I/O ⁽⁶⁾	—	16/16 Digital; 3/3 In/Out							
MXH	—	Up to x65536							
Ethernet	—	Optional							
Emergency Stop Sense Input (ESTOP) ⁽⁷⁾	—	Yes							
Resolver Interface	—	Optional ⁽⁸⁾							
Shared Bus for Regen	—	No						Yes	

Notes:

- Output voltage dependent on input voltage.
- 10-120 VDC bus requires external transformer and auxiliary power option for logic power.
- Peak value of the sine wave; rms current for AC motors is 0.707(A_{pk}).
- Optional three-phase input available on Ensemble HPe models.
- Auxiliary power option requires single phase 115-240 VAC 50-60 Hz.
- Requires IO option.
- Requires external relay to remove AC power.
- One- or two-channel input.

Ensemble HLe SPECIFICATIONS

Ensemble HLe	Units	10-40	20-40	10-80
Output Voltage ⁽¹⁾	VDC	±40	±40	±80
Peak Output Current (1 sec) ⁽²⁾	A _{pk}	10	20	10
Continuous Output Current ^(2,8)	A _{pk}	5	10	5
Power Amplifier Bandwidth	kHz	Selectable Through Software		
Minimum Load Inductance	mH	0		
Operating Temperature	°C	0 to 50		
Storage Temperature	°C	-30 to 85		
Weight	kg (lb)	10.36 (22.8)		
Maximum Shunt Regulator Dissipation	W	N/A		
Power Input	VAC	Single-Phase 7-240 VAC, 50-60 Hz		
Encoder Input Frequency	kHz	200 kHz Amplified Sine (For Onboard Multipliers), 40 MHz TTL Square Wave		
Current Loop Update Rate	kHz	20 kHz		
Servo Loop Update Rate	kHz	1 to 20 kHz		
Keep Alive/Logic Power Input ⁽⁴⁾	—	Optional		
Brake Output	—	Optional		
Position Synchronized Output	—	Single Axis Standard, Two/Three Axis Optional		
Digital Inputs	—	6 Optically-Isolated (2 High Speed)		
Digital Outputs	—	4 Optically-Isolated		
Analog Inputs	—	One 16-bit Differential		
Analog Outputs	—	One 16-bit Single-Ended		
Additional I/O ⁽⁵⁾	—	16/16 Digital; 3/3 In/Out		
MXH	—	Up to x65536		
Ethernet	—	Optional		
Emergency Stop Sense Input (ESTOP) ⁽⁶⁾	—	Yes		
Resolver Interface	—	Optional ⁽⁷⁾		

Notes:

1. Output voltage dependent upon input voltage.
2. Peak value of the sine wave; rms current for AC motors is 0.707(A_{pk}).
3. 10-120 VDC bus requires external transformer and auxiliary power option for logic power.
4. Auxiliary power option requires single phase 115-240 VAC 50-60 Hz.
5. Requires IO option.
6. Requires external relay to remove AC power.
7. One- or two-channel input.
8. Load dependent.

Ensemble CP/CL/MP SPECIFICATIONS

CP Electrical Specifications		
Logic Input Voltage	VAC	85 to 240
Bus Input Voltage	VAC	14 to 240
Output Voltage	VDC	20 to 340
Peak Output Current	A _{pk}	10 to 30
Continuous Output Current	A _{pk}	5 to 15
PWM Switching Frequency	kHz	20
Power Amplifier Bandwidth	kHz	Software Selectable
Minimum Load Inductance	mH	0.1 @ 160 VDC (1 mH @ 320 VDC)
Digital Inputs and Outputs	Standard	4 opto inputs; 2 high-speed opto inputs; 4 opto outputs
	Optional	16 additional opto inputs; 16 additional opto outputs
Analog Inputs and Outputs	Standard	1 (±10 VDC, 16-bit) input; 1 (±10 VDC, 16-bit) output
	Optional	1 additional (±10 VDC, 12-bit) input; 1 additional (±10 VDC, 16-bit) output
Encoder Inputs		TTL RS-422 standard, and auxiliary encoder input; optional amplified sine encoder input on primary encoder channel; programmable resolution up to 1024 times the analog encoder resolution; 250 kHz amplified sine primary
Operating Temperature	°C	0 to 50
Storage Temperature	°C	-30 to 85
Weight	kg (lb)	1.6 (3.6)

CL Electrical Specifications		
Logic Input Voltage	VAC	85-240
Bus Input Voltage	VAC	56 VAC (center tapped transformer; two 28 VAC windings)
Output Voltage	VDC	±40
Peak Output Current	A _{pk}	10 (load dependent)
Continuous Output Current	A _{pk}	5 (load dependent)
Power Amplifier Bandwidth	kHz	Software Selectable
Minimum Load Inductance	mH	0
Digital Inputs and Outputs	Standard	4 opto inputs; 2 high-speed opto inputs; 4 opto outputs
	Optional	16 additional opto inputs; 16 additional opto outputs
Analog Inputs and Outputs	Standard	1 (±10 VDC, 16-bit) input; 1 (±10 VDC, 16-bit) output
	Optional	1 additional (±10 VDC, 12-bit) input; 1 additional (±10 VDC, 16-bit) output
Encoder Inputs		TTL RS-422 standard, and auxiliary encoder input; optional amplified sine encoder input on primary encoder channel; programmable resolution up to 1024 times the analog encoder resolution; 250 kHz amplified sine primary
Operating Temperature	°C	0 to 50
Storage Temperature	°C	-30 to 85
Weight	kg (lb)	3.8 (8.4)

MP Electrical Specifications		
Logic Input Voltage	VDC	24 to 80
Bus Input Voltage	VDC	10 to 80
Output Voltage	VDC	10 to 80
Peak Output Current	A _{pk}	10
Continuous Output Current	A _{pk}	5
PWM Switching Frequency	kHz	20
Power Amplifier Bandwidth	kHz	Software Selectable
Minimum Load Inductance	mH	0.1 @ 80 VDC
Digital Inputs and Outputs	Standard	None
	Optional	8 opto inputs; 8 opto outputs
Analog Inputs and Outputs	Standard	1 (±10 VDC, 16-bit) input
	Optional	1 additional (±10 VDC, 12-bit) input; 1 (additional ±10 VDC, 16-bit) output
Encoder Inputs		TTL RS-422 standard, and auxiliary encoder input; optional amplified sine encoder input on primary encoder channel; programmable resolution up to 1024 times the analog encoder resolution; 250 kHz amplified sine primary
Operating Temperature	°C	0 to 50
Storage Temperature	°C	-30 to 85
Weight	kg (lb)	0.45 (1.0)

Ensemble CP/CL/MP FEATURES

Feature	Details	
Axes	Up to 10 axes of coordinated motion	
Axis Loop Type/Update Rate	PID loop with up to 20 kHz servo update rate with feedforward; four user-configurable digital filters (e.g., notch, low pass)	
On-Board Memory	Program Storage	2 MB flash memory for user programs, parameters, miscellaneous storage
	Program Execution	8 MB RAM
Driver Type Compatibility	Brushless (linear or rotary) servo with on-board commutation DC brush servo Stepper/microstepper (on-board commutation)	
Position Feedback	Encoder interface, differential RS-422 signal, sine, cosine, and marker; 32 MHz input data rate; optional onboard analog encoder interpolation (of up to 1024-times encoder multiplication)	
Position Modes	Absolute, incremental, dynamic trajectory correction	
Motion Types	Independent Motions	Point-to-point incremental; target position or velocity; velocity profiles; time based; free run
	Coordinated Motions	Advanced queuing and deferred execution features for simultaneous command execution
	Interpolated Motions	Up to 10-axis linear and circular interpolation
	Digitally Geared Motions	Gearing with optional auxiliary encoder input
	Advanced Features	Automatic PID loop gain computation (autotuning)
	Contouring	Cubic spline curve-fitting; velocity profiling
	Error Mapping	2D error mapping, backlash compensation
Acceleration Profiles	Linear and jerk limiting parabolic; independent acceleration and deceleration profiles possible	
Acceleration Ramp	Rate, time, or distance based; independent acceleration and deceleration capability	
Programmable Multitasking	Up to 5 independent tasks	
Programming	Command Set	AeroBASIC™, LabVIEW®, VB.Net, C#
Command Execution Modes	AUTO	Program runs complete upon startup
	SINGLE	Full debug capability to step, step over, step into individual program lines
	IMMEDIATE	Commands are executed upon entry
	REMOTE	Command execution controlled by remote host through Ethernet, RS-232, or IEEE-488 communications port via ASCII strings
Process Time	Command execution up to 1000 lines of code per 1 ms (from command sent to motion start); read request @ 1 ms; average is 7 μs per program line (e.g., c = a + b)	
Additional Interfaces	Serial	10/100 Base-T Ethernet communication interface for system setup, application networking, embedded programming, immediate commands, and Modbus over TCP; USB communication interface for system setup, application networking, Windows® PC control interface
	Machine Control	Estop discrete input to stop all axes

**This product family has been replaced by the following new product:
 >> S-340 Piezo Tip / Tilt-Platform**

S-340 High-Speed Piezo Tip/Tilt Platforms



- Fixed Orthogonal Axes with a Common Pivot Point
- 4 mrad Optical Beam Deflection
- For Mirrors to 100 mm Ø
- Sub-µrad Resolution
- Closed-Loop Versions for Better Linearity
- Differential Design for Excellent Temperature Stability
- Zero Friction Flexure Guides
- Single-Moving-Platform, Parallel-Kinematics Design: Equal Dynamics for all Axes, Better Linearity & Temperature Stability

S-340 piezo tip/tilt platforms are fast and compact tilt units, providing precise angular movements of the top platform in two orthogonal axes. The tip/tilt range is 2 mrad (equivalent to 4 mrad optical beam deflection) with sub-µrad reso-

lution. Closed-loop versions are available for highest accuracy and repeatability. S-340 systems are designed for mirrors up to 100 mm diameter and have outstanding angular stability over a wide temperature range.

Application Examples

- Image stabilization
- Laser beam stabilization
- Beam switching
- Adaptive optics systems
- Laser beam steering & scanning
- Correction of polygon scanner errors
- Interlacing, dithering

models are ideal for applications where the position is controlled by an external loop, based on data provided by a sensor (e.g. PSD, quad cell, CCD chip, etc.).

The closed-loop versions are equipped with two pairs (one per axis) of LVDT (linear variable differential transformer) sensors operated in a bridge circuit for ultra-high resolution and angular stability. They provide sub-µrad resolution and repeatability.

Higher Performance Through Parallel Kinematics

S-340 tip/tilt platforms feature a single moving platform, parallel-kinematics design with a common pivot point. Compared to stacked, multi-axis systems, the parallel-kinematics design provides faster response and better linearity with equal dynamics for all axes in a smaller package.

Working Principle / Lifetime

S-340 tip/tilt platforms are equipped with two pairs of long-life, ceramic-encapsulated, high-performance PICMA® piezo drives operating as a unit in push/pull mode. The aluminum case is equipped with an integrated, FEA-modeled (finite element analysis) circular flexure featuring zero stiction, zero friction and exceptional guiding precision. Since drives and guides are frictionless and not subject to wear and tear, these units offer an exceptionally high level of reliability.

Notes

See the "Selection Guide" on p. 3-8 for comparison with other steering mirrors.

See the "Piezo Drivers & Nanopositioning Controllers" section

Ordering Information

S-340.A0
 Θ_x, Θ_y Piezo Tip/Tilt Platform, 2 mrad, Aluminum Top Plate

S-340.i0
 Θ_x, Θ_y Piezo Tip/Tilt Platform, 2 mrad, Invar Top Plate

S-340.S0
 Θ_x, Θ_y Piezo Tip/Tilt Platform, 2 mrad, Steel Top Plate

S-340.T0
 Θ_x, Θ_y Piezo Tip/Tilt Platform, 2 mrad, Titanium Top Plate

S-340.AL
 Θ_x, Θ_y Piezo Tip/Tilt Platform, 2 mrad, Aluminum Top Plate, Closed-Loop

S-340.iL
 Θ_x, Θ_y Piezo Tip/Tilt Platform, 2 mrad, Invar Top Plate, Closed-Loop

S-340.SL
 Θ_x, Θ_y Piezo Tip/Tilt Platform, 2 mrad, Steel Top Plate, Closed-Loop

S-340.TL
 Θ_x, Θ_y Piezo Tip/Tilt Platform, 2 mrad, Titanium Top Plate, Closed-Loop

Ask about custom designs!

for our comprehensive line of low-noise modular and OEM control electronics for computer and manual control.

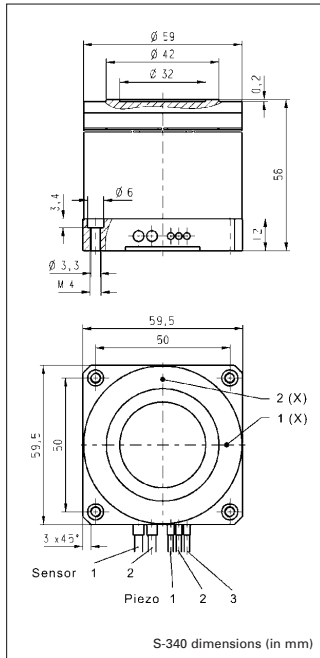
Materials Match

Platform	Recommended Models	Mirror
Aluminum	Aluminum	S-340.Ax
Invar	Zerodur glass	S-340.ix
Titanium	BK7 glass	S-340.Tx
Steel		S-340.Sx

**This product family has been replaced
by the following new product:
>> S-340 Piezo Tip / Tilt-Platform**

Piezo • Nano • Positioning

PI



Technical Data

Models	S-340.x0	S-340.xL	Units	Notes see page 3-26
Active axes	Θ_x, Θ_y	Θ_x, Θ_y		
* Open-loop tilt angle 0 to 100 V	2 (4 optical)	2 (4 optical)	mrad $\pm 20\%$	A2
* Closed-loop tilt angle	-	2 (4 optical)	mrad	A3
Integrated feedback sensor	-	4 x LVDT		B
** Closed-loop / open-loop resolution	- / 0.1	0.5 / 0.1	μrad	C1
Closed-loop linearity (typ.)	-	± 0.1	%	
Full-range repeatability (typ.)	-	± 1	μrad	C3
Electrical capacitance	6.0 / axis	6.0 / axis	$\mu\text{F} \pm 20\%$	F1
*** Dynamic operating current coefficient (DOCC)	0.38 / axis	0.38 / axis	$\mu\text{A}/(\text{Hz} \times \mu\text{rad})$	F2
**** Unloaded resonant frequency (f_0)	1.4	1.4	$\text{kHz} \pm 20\%$	G2
**** Resonant frequency w/ $\phi 50 \times 15$ mm glass mirror	0.9	0.9	$\text{kHz} \pm 20\%$	G3
**** Resonant frequency w/ $\phi 75 \times 22$ mm glass mirror	0.4	0.4	$\text{kHz} \pm 20\%$	G3
Distance, pivot point to platform surface (T)	7.5	7.5	mm	
**** Platform moment of inertia	18000	18000	$\text{g} \cdot \text{mm}^2$	
Operating temperature range	- 20 to 80	- 20 to 80	$^{\circ}\text{C}$	H2
Voltage connection	3 x VL	3 x VL		J1
Sensor connection	-	2 x L		J2
Weight (w/o cables)	335	335	$\text{g} \pm 5\%$	
Material (case / platform)	Al / depends on version	Al / depends on version		L
Recommended amplifier/controller (codes explained page 3-9)	G [†] , C	H [†] , E		

- Piezo Actuators
- Nanopositioning & Scanning Systems
- Active Optics / Steering Mirrors**
- Tutorial: Piezo-electrics in Positioning
- Capacitive Position Sensors
- Piezo Drivers & Nanopositioning Controllers
- Hexapods / Micropositioning
- Photonics Alignment Solutions
- Motion Controllers
- Ceramic Linear Motors & Stages
- Index

* Mechanical tilt, optical beam deflection is twice as large.
 ** For calibration information see p. 3-7.
 Resolution of PZT tip/tilt platforms is not limited by friction or stiction. Noise equivalent motion with E-503 amplifier.
 *** Dynamic Operating Current Coefficient in μA per Hz and μrad .
 Example: Sinusoidal scan of $100 \mu\text{rad}$ at 10 Hz requires approximately 0.38 mA drive current.
 **** Value for aluminum top plate. Lower resonant frequency for other platforms due to higher moment of inertia: titanium: $\pm 60\%$; invar: $\pm 200\%$; steel: $\pm 190\%$.
[†] With (1 x E-505.00S + 2 x E-505.00) or 1 x E-503.00S

E-616 Controller for Multi-Axis Piezo Tip/Tilt Mirrors and Platforms

Flexible Multi Channel OEM Electronics with Coordinate Transformation



Ordering Information

E-616.SS0

Multi Channel Servo-Controller / Driver for Piezo Tip/Tilt Mirror Platforms with SGS and Differential Drive

E-616.S0

Multi Channel Servo-Controller / Driver for Piezo Tip/Tilt Mirror Platforms with SGS and Tripod Drive

- **Three Integrated Amplifiers Provide up to 10 W Peak Power**
- **Closed-Loop and Open-Loop Versions**
- **Internal Coordinate Transformation Simplifies Control of Parallel Kinematics Designs (Tripod & Differential Drive)**
- **Compact and Cost-Effective Design for OEMs**

The E-616 is a special controller for piezo based tip/tilt mirrors and tip/tilt platforms. It contains two servo controllers, sensor channels and power amplifiers in a compact unit. The controller works with high-resolution SGS position sensors used in PI piezo mechanics and provides optimum position stability and fast response in the nanometer and prad-range respectively. A high output power of 10 W per channel allows dynamic operation of the tip/tilt mirrors for applications such as (laser) beam steering and stabilization.

Tripod or Differential Piezo Drive? One for All!

PI offers two basic piezo tip/tilt mirror designs. Both are parallel-kinematics designs where the individual piezo actuators affect the same moving platform. With the tripod design (e.g. S-325, see p. 2-92) the platform is driven by three piezo actuators placed with 120° spacing. The differential drive design (S-330, see p. 2-88 or S-334, see p. 2-90) with two orthogonal axes and a fixed pivot point is based on two pairs of actuators operating in

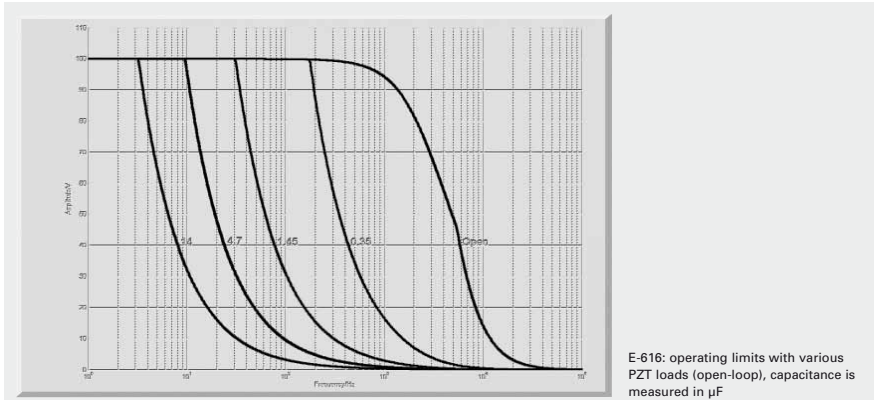
push / pull-mode. The differential evaluation of two sensors per axis provides an improved linearity and resolution.

Internal Coordinate Transformation Simplifies Control

Parallel-kinematics require the transformation of the commanded tilt angles into the corresponding linear motion of the individual actuators. In the E-616.S0, this is taken care of by an integrated circuit, eliminating the need of additional external hardware or software. Additionally with the E-616.S0 all actuators can be commanded by an offset-voltage simultaneously. As a result a vertical movement, for example for optical path tuning, is obtained.

Simple Setup and Operation

To facilitate integration, setup and operation the E-616 features both front and rear panel connections: The 25 pin sub-D piezo & sensor connector is located on the front, along with offset trim pots and LEDs for Power and Overflow. A 32 pin rear connector allows commanding and reading the sensor and amplifier monitor outputs.



E-616: operating limits with various PZT loads (open-loop), capacitance is measured in μF

Technical Data

Model	E-616.S0	E-616.SS0
Function	Controller for parallel-kinematics piezo tip/tilt mirror systems with strain gauge sensors, tripod design	Controller for parallel-kinematics piezo tip/tilt mirror systems with strain gauge sensors, differential design
Tilt axes	2	2
Sensor		
Servo characteristics	P-I (analog), notch filter	P-I (analog), notch filter
Sensor type	SGS	SGS
Sensor channels	3	2
External synchronization	200 kHz TTL	200 kHz TTL
Amplifier		
Control input voltage range	-2 V to +12 V	-2 V to +12 V
Output voltage	-20 V to +120 V	-20 V to +120 V
Amplifier channels	3	3
Peak output power per channel	10 W	10 W
Average output power per channel	5 W	5 W
Peak current	100 mA	100 mA
Average current per channel	50 mA	50 mA
Current limitation	Short-circuit-proof	Short-circuit-proof
Voltage gain	10	10
Amplifier bandwidth, small signal	3 kHz	3 kHz
Amplifier bandwidth, large signal	See frequency diagram	See frequency diagram
Ripple, noise, 0 to 100 kHz	<20 mVpp	<20 mVpp
Amplifier resolution	<1 mV	<1 mV
Interfaces and operation		
Piezo / sensor connector	25-pin sub-D connector	25-pin sub-D connector
Analog input	32-pin connector	32-pin connector
Sensor monitor output	0 to +10 V for nominal displacement	0 to +10 V for nominal displacement
Sensor monitor socket	32-pin connector	32-pin connector
Display	Power-LED and sensor OFL display	Power-LED and sensor OFL display
Miscellaneous		
Operating temperature range	5 °C to 50 °C	5 °C to 50 °C
Overheat protection	Max. 75 °C, deactivation of the piezo voltage output	Max. 75 °C, deactivation of the piezo voltage output
Dimensions	160 mm x 100 mm x 10 TE	160 mm x 100 mm x 10 TE
Mass	700 g	700 g
Operating voltage	12 to 30 V DC	12 to 30 V DC
Power consumption	30 W	30 W

Linear Actuators & Motors

Nanopositioning / Piezoelectrics

Piezo Flexure Stages / High-Speed Scanning Systems

Linear

Vertical & Tip/Tilt

2- and 3-Axis

6-Axis

Fast Steering Mirrors / Active Optics

Piezo Drivers / Servo Controllers

Single-Channel

Multi-Channel

Modular

Accessories

Piezoelectrics in Positioning

Nanometrology

Micropositioning

Index

M-122 Precision Micro-Translation Stage

Fast & Compact with Direct Position Measurement



The M-122.2DD miniature translation stage features an optical linear encoder with 0.1 μm position resolution and a highly efficient ballscrew.

- Travel Range 25 mm
- 0.1 μm Optical Linear Encoder for Highest Accuracy & Repeatability
- Min. Incremental Motion to 0.2 μm
- Max. Velocity 20 mm/s
- Cross-Roll Bearings
- Recirculating Ball Screw Drives Provide High Speeds & Long Lifetimes

The M-122 palm-top-sized translation stage combines small dimensions, high speeds and very high accuracy at a competitive price. It features a space-saving, folded drive train with the servo motor and drive screw side-by-side. Equipped with a non-contacting optical linear encoder and a preloaded, precision-ground, ball-screw, these stages can provide much higher accuracy and better repeatability than conventional stepper motor stages or rotary encoder-equipped servo motor stages.

Low Friction, High Speed, Maintenance-Free

Due to its low-friction, the backlash-free ball screw yields significantly higher mechanical

efficiency than leadscrews, and allows maintenance-free, high duty-cycle operation at high velocities up to 20 mm/sec.

XY and XYZ Combinations

M-122 stages can be combined to very compact XY and XYZ systems. The M-122.AP1 mounting bracket is available to mount the Z-axis.

Limit and Reference Switches

For the protection of your equipment, non-contact Hall-effect limit and reference switches are installed. The direction-sensing reference switch supports advanced automation applications with high precision.

Low Cost of Ownership

The combination of these positioners with the networkable, single-channel C-863 Mercury™ servo motor controller (s. p. 4-114) offers high performance for a very competitive price in both single- and multi-axis configurations. For multi-axis applications, the C-843 PC plug-in controller board with on-board servo amplifiers (s. p. 4-120) is another cost-effective alternative.

Application Examples

- Photonics packaging
- Fiber positioning
- Metrology
- Quality assurance testing
- Testing equipment
- Micromachining

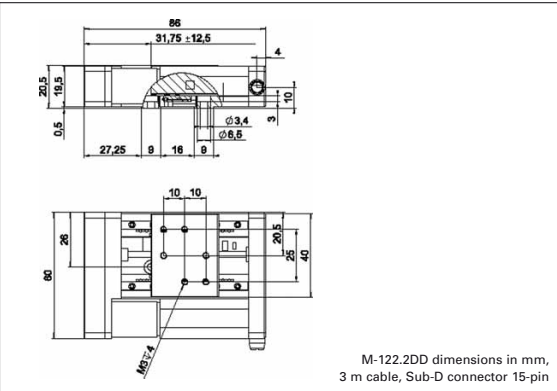
Ordering Information

M-122.2DD
High-Precision Translation Stage,
25 mm, Direct-Drive DC Motor,
Ballscrew

Accessories

M-122.AP1
Angle bracket for vertical
mounting of M-122 stages

Ask about custom designs



M-122.2DD dimensions in mm,
3 m cable, Sub-D connector 15-pin

Technical Data

Model	M-122.2DD
Active axes	X
Motion and positioning	
Travel range	25 mm
Integrated sensor	Linear encoder
Sensor resolution	0.1 μm
Design resolution	0.1 μm
Min. incremental motion	0.2 μm
Backlash	0.2 μm
Unidirectional repeatability	0.15 μm
Pitch	$\pm 150 \mu\text{rad}$
Yaw	$\pm 150 \mu\text{rad}$
Max. velocity	20 mm/s
Origin repeatability	1 μm
Mechanical properties	
Drive screw	Recirculating ballscrew
Thread pitch	0.5 mm
Stiffness in motion direction	0.25 N/ μm
Max. load	50 N
Max. push/pull force	20 N
Max. lateral force	25 N
Drive properties	
Motor type	DC motor
Operating voltage	0 to $\pm 12 \text{ V}$
Electrical power	2.25 W
Limit and reference switches	Hall-effect
Miscellaneous	
Operating temperature range	-20 to +65
Material	Aluminum, steel
Dimensions	86 x 60 x 20.5 mm
Mass	0.22 kg
Recommended controller/driver	C-863 (single-axis) C-843 PCI board (up to 4 axes)



EPO-TEK[®] 320

Technical Data Sheet

For Reference Only
Optical, Opaque Epoxy

Number of Components:	Two	Minimum Bond Line Cure Schedule*:	
Mix Ratio By Weight:	10:2	65°C	2 Hours
Specific Gravity:		23°C	24 Hours
Part A	1.10		
Part B	0.87		
Pot Life:	1 Hour		
Shelf Life:	1 year at room temperature		

*Note: Container(s) should be kept closed when not in use. *Please see Applications Note available on our website.
- TOTAL MASS SHOULD NOT EXCEED 25 GRAMS -*

Product Description:

EPO-TEK[®] 320 is a two component, black-colored and optically opaque epoxy designed for optical, medical, and opto-electronic packaging of semiconductor devices and components. It is a widely used fiber-optic grade epoxy.

EPO-TEK[®] 320 Advantages & Application Notes:

- Optically opaque between IR and VISIBLE regions of light, including 185 – 2500 nm range
- It can be used for room temperature curing, low temp, or box oven elevated temperature cure.
- Many modifications are available, such as viscosity, electrical insulation, Tg, and flexibility. Contact techserv@epotek.com for your best recommendation.
- Suggested applications
 - Optical:
 - blocking light in photonics packaging through VIS and NIR range; sensor packaging including IR detectors packaged in TO-cans
 - bonding of various optics including lens, prism, diodes
 - adhesion to metals, most plastics, and glasses.
 - Fiber Optic: sealing / potting fibers into the boot, ferrule, or fiber feed-through of the package wall
 - Medical: bonding/ potting/ sealing of optics used for imaging related electronics; complies with USP Class VI biocompatibility standards
- The low viscosity nature allows syringe dispensing and automation, hand, brushing, roller coating, tooth-pick or spatula, and pour or dipping.

Typical Properties: *(To be used as a guide only, not as a specification. Data below is not guaranteed. Different batches, conditions and applications yield differing results; Cure condition: varies as required ; * denotes test on lot acceptance basis)*

Physical Properties:	
*Color: Part A: Black Part B: Clear/Colorless	Die Shear Strength @ 23°C: ≥ 15 Kg / 5,100 psi
*Consistency: Slightly thixotropic paste	Degradation Temp. (TGA): 384°C
*Viscosity (100 @ RPM/23°C): 700 – 1,200cPs	Weight Loss:
Thixotropic Index: 5.7	@ 200°C: 0.27%
*Glass Transition Temp.(Tg): ≥ 55°C (Dynamic Cure	@ 250°C: 0.45%
20—200°C /ISO 25 Min; Ramp -10—200°C @ 20°C/Min)	@ 300°C: 0.80%
Coefficient of Thermal Expansion (CTE):	Operating Temp:
Below Tg: 29 x 10 ⁻⁶ in/in/°C	Continuous: - 55°C to 200°C
Above Tg: 100 x 10 ⁻⁶ in/in/°C	Intermittent: - 55°C to 300°C
Shore D Hardness: 83	Storage Modulus @ 23°C: 261,271 psi
Lap Shear Strength @ 23°C: > 2,000psi	*Particle Size: ≤ 20 Microns
Optical Properties @ 23°C:	
Index of Refraction @ 23°C: N/A	Spectral Transmission @ 23°C: < 1% @ 300 - 2500nm
Electrical & Thermal Properties:	
Thermal Conductivity: N/A	Volume Resistivity @ 23°C: ≥ 1 x 10 ⁶ Ohm-cm
Dielectric Constant (1KHz): N/A	Dissipation Factor (1KHz): N/A

EPOXY TECHNOLOGY, INC.
14 Fortune Drive, Billerica, MA 01821-3972 Phone: 978.667.3805 Fax: 978.663.9782
www.EPOTEK.com

Epoxyes and Adhesives for Demanding Applications™

This information is based on data and tests believed to be accurate. Epoxy Technology, Inc. makes no warranties (expressed or implied) as to its accuracy and assumes no liability in connection with any use of this product.

Appendix E. USGS Radiometric Questionnaire on Frenchman Flat [9]

IVOS test site questionnaire: QA4EO-WGCV-IVO-CSP-001

Appendix 1: Template for CEOS reference standard test site

CEOS Reference standard test site for Land radiometric gain

CEOS Reference: QA4EO-WGCV-IVO-CSP-xxx¹

Name of site: Lspec Frenchman

Point of contact:

Address:

Range of applications¹:

¹ to be completed by QA4EO secretariat

IVOS test site questionnaire: QA4EO-WGCV-IVO-CSP-001

1. Site location

1.1. Identification and characterisation

1.1.1. Site Name

Lspec at Frenchman Flat

1.1.2. Location

Latitude: 36.80928 N

Longitude: -115.93479 W

1.1.3. Google Earth Image (1x1 degree around the site center)



1.1.4. Altitude

940 m

Questionnaire for Cal/Val test site characterisation for land imager radiometric gain

IVOS test site questionnaire: QA4EO-WGCV-IVO-CSP-001

1.1.5. Description of the landscape

The Frenchman Flat vicarious calibration site is situated on a homogeneous section of the Frenchman Flat dry lake-bed found North-North-East of Mercury, Nevada on the Nevada Test Site (NTS) range. This is the site of the LED Spectrometer (LSpec) autonomous calibration facility (<http://lspec.jpl.nasa.gov>).

Hard clay desert playa surrounded by light creosote and sage scrub

Natural playa extent is roughly 3 x 4 Km but majority of surface is scarred by weapons testing debris such as roads, buildings, bunkers and bridges

1.1.6. Environment

1.1.7. Topography



Figure 1: Site topography

1.2. Site view

Site photos are available at <http://lspec.jpl.nasa.gov>

IVOS test site questionnaire: QA4EO-WGCV-IVO-CSP-001



Figure 2: Site overview

2. Logistic information

2.1.Site proximity from road

I-95

2.2.Access

Road

2.3.Nearest town

Las Vegas

2.4.Distance from nearest town/port

100km Northwest of Las Vegas, Nevada, USA

2.5.Logistics (Hotel, Restaurant, etc.)

IVOS test site questionnaire: QA4EO-WGCV-IVO-CSP-001

2.6. Access to Communications

2.7. Owner

3. Site Climatology

3.1. General atmospheric conditions: Meteorological conditions

3.1.1. Annual pluviometry

DESERT ROCK WSMO, NEVADA (262251)

Period of Record Monthly Climate Summary

Period of Record : 4/ 1/1984 to 6/30/2007

Average Total Precipitation (in.)	0.45	1.31	0.50	0.51	0.10	0.22	0.36	0.26	0.52	0.49	0.27	0.34	5.34
Average Total SnowFall (in.)	0.0	0.0	0.0	0.0	0.0	0.0	0.0	0.0	0.0	0.0	0.0	0.0	0.0
Average Snow Depth (in.)	0	0	0	0	0	0	0	0	0	0	0	0	0

3.1.2. Wind

3.1.3. Clear sky conditions

Average number of days with clear skies >300

3.2. Atmosphere characterisation

3.2.1. Aerosol characteristics

3.2.1.1. Seasonal variation of the aerosol

3.2.1.2. AOT_550: Historical data

Questionnaire for Cal/Val test site characterisation for land imager radiometric gain

IVOS test site questionnaire: QA4EO-WGCV-IVO-CSP-001

3.2.1.3.Data from AERONET CIMEL network

Historical record of site from mid-November, 2006

Operational Time at 'Frenchman_Flat' Site

484 Days [1.326 Years] : Start Date: 11-DEC-2006; Latest Date: 13-MAY-2008

Total Processed Data [Years represent total data equivalent]

- Level 1.0 AOD: 453 Days [1.241 Years]
- Level 1.5 AOD: 434 Days [1.189 Years]
- Level 2.0 AOD: 0 Days [0.000 Years]

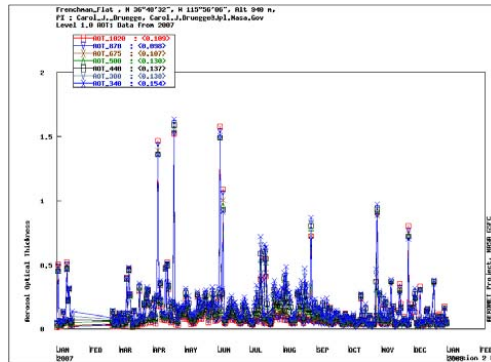


Figure 3: Monthly variability of AOT (2007)

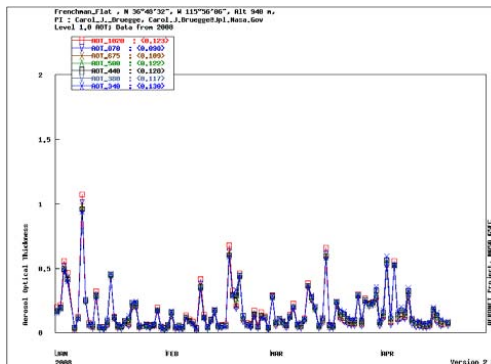


Figure 4: Monthly variability of AOT (2008)

Questionnaire for Cal/Val test site characterisation for land imager radiometric gain

IVOS test site questionnaire: QA4EO-WGCV-IVO-CSP-001

3.2.1.4. Nominal values of AOT at 450, 550, 650, 850 nm

3.2.1.5. Absolute error of AOT at 450, 550, 650, 850 nm

3.2.1.6. Model of aerosol used

3.2.1.6.1. Granulometry

3.2.1.6.2. Refraction index used

3.2.1.7. Alpha

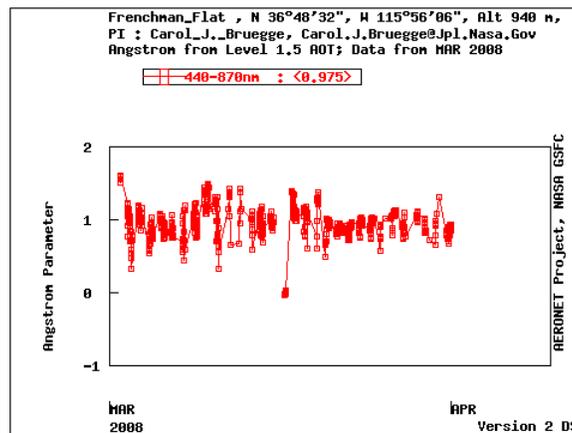


Figure 5: Monthly variability of Angstrom coefficient (2008)

3.2.2. Water vapour content characteristics

3.2.2.1. Water vapour content origin

Questionnaire for Cal/Val test site characterisation for land imager radiometric gain

IVOS test site questionnaire: QA4EO-WGCV-IVO-CSP-001

3.2.2.2. Seasonal variation of the water vapour content

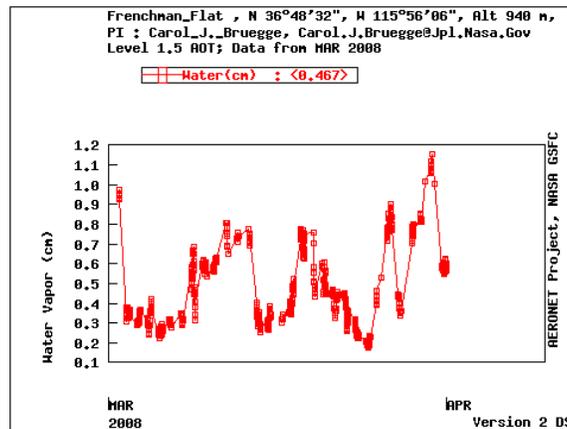


Figure 6: Monthly variability of water vapour content (2008)

3.2.2.3. Mean and accuracy

3.3. Surface characterisation

3.3.1. Surface albedo characteristics

3.3.2. Surface reflectance characteristics

3.3.2.1. Instrumentation used for characterisation

Hyperspectral surface reflectance is measured about twice a year via ASD FR Field spectrometer. For further information, see: <http://lspec.jpl.nasa.gov>

3.3.2.2. Route of traceability

Met: manufacturer's initial calibration (RM Young & Campbell)

Questionnaire for Cal/Val test site characterisation for land imager radiometric gain

IVOS test site questionnaire: QA4EO-WGCV-IVO-CSP-001

3.3.2.3. Mean reflectance at Nadir (full spectrum)

3.3.2.4. Uncertainty of reflectance (please give breakdown of uncertainty contributions)

3.3.2.5. Mean reflectance at Nadir at 450, 550, 650, 850 nm

3.3.2.6. $\Delta\rho$ at 450 nm, 550, 650, 850 nm

3.3.3. BRDF (or specific angles)

3.3.3.1. Instrument used

3.3.3.2. Relative error on BRDF correction at $\theta_s=45$ degrees, $\theta_v=30$ degrees

3.3.4. Surface reflectance – variability across site (uniformity) (%)

- Fairly clear area: 1000 m square clocked corners N-S & E-W
- Homogenous area: 300 m square clocked sides N-S & E-W
- Monitored area: 50m square clocked sides N-S & E-W

4. Site instrumentation (Nominal)

4.1. Meteorological instrumentation (list)

4.1.1. Meteo station (Temperature, pressure, humidity)

Questionnaire for Cal/Val test site characterisation for land imager radiometric gain

IVOS test site questionnaire: QA4EO-WGCV-IVO-CSP-001

4.1.2. Pluviometer

4.1.3. Anemometer

4.2. Atmospheric instrumentation

4.2.1. Instrument used for aerosol characterisation

4.2.1.1. Instrument used

4.2.1.2. Route of traceability

4.2.1.3. Measurement protocol

4.2.1.3.1. Scanning mode

4.2.1.3.2. Spectral characteristics

4.2.1.3.3. Frequency of measurements

4.2.2. Instrument used for surface irradiance characterisation

4.2.2.1. Instrument used

4.2.2.2. Route of traceability

4.2.2.3. Measurement protocol

Questionnaire for Cal/Val test site characterisation for land imager radiometric gain

IVOS test site questionnaire: QA4EO-WGCV-IVO-CSP-001

4.2.3. Instrument used for water vapour content characterisation

4.2.3.1. Instrument used

4.2.3.2. Route of traceability

4.2.3.3. Measurement protocol

4.3. Surface instrumentation

4.3.1. Instrument used for reflectance/radiance characterisation

4.3.1.1. Instrument used

4.3.1.2. Route of traceability

4.3.1.3. Measurement protocol

4.3.1.3.1. Scanning mode

4.3.1.3.2. Spectral characteristics

4.3.1.3.3. Frequency of measurements

4.3.2. Instrument used for BRDF characterisation

4.3.2.1. Instrument used

4.3.2.2. Route of traceability

Questionnaire for Cal/Val test site characterisation for land imager radiometric gain

IVOS test site questionnaire: QA4EO-WGCV-IVO-CSP-001

4.3.2.3. Measurement protocol

4.3.2.3.1. Scanning mode

4.3.2.3.2. Spectral characteristics

4.3.2.3.3. Frequency of measurements

5. Current status of the site

5.1. Instrumented

Instrumented, Automated

5.2. Maintained (source and commitment of funding)

- Visited and maintained quarterly
- Source of funding for maintenance: US Government
- Restricted access

5.3. Regularly visited (state frequency)

- Human
- Satellite
- Aircraft
- Automated

IVOS test site questionnaire: QA4EO-WGCV-IVO-CSP-001

6. Site usage

6.1. Historical record of comparisons (ground, aircraft and satellite)

6.2. Date / sensor / location of results

6.3. Regularity of satellite data (if known)

6.4. Satellite and sensor ID

7. Contact information

7.1. Point of Contact (Name and address)

Carol J. Bruegge, Ph.D.

Earth Remote Sensing Science

NASA/ Jet Propulsion Laboratory Mail Stop 183-601

4800 Oak Grove Dr.

Pasadena, CA 91109-8099

Tel: + 818-354-4956

Fax: + 818-354-5148

E-mail: Carol.J.Bruegge@Jpl.Nasa.Gov

7.2. Instrumentation maintenance

Questionnaire for Cal/Val test site characterisation for land imager radiometric gain

IVOS test site questionnaire: QA4EO-WGCV-IVO-CSP-001

8. Dataset availability and owner

8.1.Dataset

8.2.Owner

8.3.Availability

9. References

9.1.Bibliography

9.1.1. Characterization of the site

9.1.2. Description of the methodology

9.1.3. Description of the instrumentation

9.1.4. Description of applications for vicarious calibration

9.2.Site Web

<https://lspec.jpl.nasa.gov/>

IVOS test site questionnaire: QA4EO-WGCV-IVO-CSP-001

The screenshot shows the JPL website header with the NASA logo and 'Jet Propulsion Laboratory California Institute of Technology'. A search bar for 'Search JPL' is visible. Below the header is a navigation menu with links for 'JPL HOME', 'EARTH', 'SOLAR SYSTEM', 'STARS & GALAXIES', and 'SCIENCE & TECHNOLOGY'. A banner image shows a desert landscape with the text 'LSpec' overlaid. A 'Navigation' sidebar on the left lists 'Home', 'Facility', 'Field Data', 'References', and 'Links'. The main content area features a photograph of the LSpec LED Spectrometer setup on a tripod in a desert field, with mountains in the background. Below the photo is the caption: 'LED Spectrometer (LSpec) LED pods at Frenchman Flat'.

9.3. General acknowledgement

For AERONET data : We thank Carrol Bruegge and her staff for establishing and maintaining the site used in this investigation.

Bibliography

1. Vagni, F., *Survey of Hyperspectral and Multispectral Imaging Technologies*, North Atlantic Treaty Organization, May 2007, TR-SET-065-P3.
2. Black, J., “Minimum Design Requirements For Space Imaging Component,” July 2009, Appendix of telescope design contract awarded to RC Optical Systems.
3. Aerotech, *ADRS Series Mechanical-Bearing Rotary Stages*, January 2010, <http://www.aerotech.com/products/pdf/ADRS.pdf>.
4. Aerotech, *Ensemble Multi-Axis Motion Control Software*, January 2010, <http://www.aerotech.com/products/PDF/Ensemble.pdf>.
5. Physik Instrumente, *S-340 High-Speed Piezo Tip/Tilt Platforms*, January 2010, <http://www.physikinstrumente.com/en/pdf/S340-Datasheet-alt.pdf>.
6. Physik Instrumente, *E-616 Controller for Multi-Axis Piezo Tip/Tilt Mirrors and Platforms*, January 2010, <http://www.physikinstrumente.com/en/products/prdetail.php?sortnr=603900>.
7. Physik Instrumente, *M-122 Precision Micro-Translation Stage*, January 2010, <http://www.physikinstrumente.com/en/pdf/M122-Datasheet.pdf>.
8. Epoxy Technology, *EPO-TEK 320 Technical Data Sheet*, January 2010, <http://www.epotek.com/SSCDOcs/datasheets/320.pdf>.
9. United States Geological Survey, *USGS Catalogue of Worldwide Test Sites for Sensor Characterization*, November 2009, <http://calval.cr.usgs.gov/sites-catalog-map.php>.
10. Short, N. M., “The Remote Sensing Tutorial,” September 2009, <http://rst.gsfc.nasa.gov/Front/overview.html>.
11. Department of Defense, *Multispectral Users Guide*, August 1995.
12. Black, J. and Cobb, R., “Space Chromotomography Experiment (CTEx),” September 2009, 2009 DOD Space Experiments Review Board Brief.
13. NASA’s Goddard Space Flight Center, *Earth Observing 1*, December 2009, <http://eo1.gsfc.nasa.gov/Technology/Hyperion.html>.
14. Folkman, M. A., Pearlman, J., Liao, L. B., and Jarecke, P. J., “EO-1/Hyperion hyperspectral imager design, development, characterization, and calibration,” *Hyperspectral Remote Sensing of the Land and Atmosphere*, edited by W. L. Smith and Y. Yasuoka, Vol. 4151, SPIE, 2001, pp. 40–51.
15. Corson, M. R. and Davis, C. O., “HICO Science Mission Overview,” September 2009, <http://www.ioccg.org/sensors/HICO-IOCCG13.pdf>.
16. 377th Air Base Wing Public Affairs, “Tactical Satellite 3 Factsheet,” Tech. rep., Kirtland Air Force Base, October 2009, <http://www.kirtland.af.mil/library/factsheets/factsheet.asp?id=12887>.
17. Hawks, M. R., “CTEx Optical Design Notes,” 2009, Unpublished work of LtCol Michael Hawks, Engineering Physics Department, Air Force Institute of Technology.

18. O'Dell, D. C., *Development and Characterization of a Field-Deployable Fast Chromotomographic Imager*, Master's thesis, Air Force Institute of Technology, Wright-Patterson AFB, March 2010.
19. RC Optical Systems, *AFIT CTS Platform Update*, December 2009, Teleconference between AFIT and RC Optical Systems with associated slides.
20. NASA Jet Propulsion Laboratory, *LED Spectrometer (LSpec) LED pods at Frenchman Flat*, November 2009, <https://lspec.jpl.nasa.gov/index.html>.
21. Wertz, J. R. and Larson, W. J., *Space Mission Analysis and Design*, Microcosm Press, Hawthorne, CA, 3rd ed., 1999.
22. Opto-Knowledge Systems, Inc., *Why Spectral Imaging?*, December 2009, <http://www.techexpo.com/WWW/opto-knowledge/why-spectral.html>.
23. Bostick, R. L. and Perram, G. P., "Hyperspectral Imaging Using Chromotomography: A Fieldable Visible Instrument for Transient Events," *International Journal of High Speed Electronics and Systems*, Vol. 18, No. 3, 2008.
24. Murguia, J. E., Reeves, T. D., Mooney, J. M., Ewing, W. S., Shepherd, F. D., and Brodzik, A. K., "Compact visible/near-infrared hyperspectral imager," *Infrared Detectors and Focal Plane Arrays VI*, edited by E. L. Dereniak and R. E. Sampson, Vol. 4028, SPIE, 2000, pp. 457–468.
25. Bostick, R. L., Perram, G. P., and Tuttle, R., "Characterization of spatial and spectral resolution of a rotating prism chromotomographic hyperspectral imager," *Next-Generation Spectroscopic Technologies II*, edited by M. A. Druy, C. D. Brown, and R. A. Crocombe, Vol. 7319, SPIE, 2009, p. 731903.
26. Sheirich, P., *An Engineering Trade Space Analysis for a Space-Based Hyperspectral Chromotomographic Scanner*, Master's thesis, Air Force Institute of Technology, Wright-Patterson AFB, March 2009.
27. Pearlman, J., Carman, S., Segal, C., Jarecke, P., Clancy, P., and Browne, W., "Overview of the Hyperion Imaging Spectrometer for the NASA EO-1 mission," *Geoscience and Remote Sensing Symposium, 2001. IGARSS '01. IEEE 2001 International*, Vol. 7, 2001, pp. 3036–3038 vol.7.
28. Beiso, D., "Overview of Hyperion on-orbit instrument performance, stability, and artifacts," *Applied Imagery Pattern Recognition Workshop, 2002. Proceedings. 31st*, Oct. 2002, pp. 95–101.
29. NASA, "EO-1 Firsts: Hyperion Science Validation," December 2009, <http://eo1.gsfc.nasa.gov/new/general/firsts/hyperion.html>.
30. Ungar, S., Pearlman, J., Mendenhall, J., and Reuter, D., "Overview of the Earth Observing One (EO-1) mission," *Geoscience and Remote Sensing, IEEE Transactions on*, Vol. 41, No. 6, June 2003, pp. 1149–1159.
31. Corson, M., Korwan, D., Lucke, R., Snyder, W., and Davis, C., "The Hyperspectral Imager for the Coastal Ocean (HICO) on the International Space Station," *Geoscience and Remote Sensing Symposium, 2008. IGARSS 2008. IEEE International*, Vol. 4, July 2008, pp. IV –101–IV –104.

32. NASA, "TACSAT 3 Information," <http://www.nasa.gov/centers/wallops/missions/tacsat3.html>, September 2009.
33. Raytheon, "Advanced Responsive Tactically Effective Military Imaging Spectrometer (ARTEMIS) Fact Sheet," Raytheon Homepage, September 2009, <http://www.raytheon.com/capabilities/products/stellent/groups/sas/documents/content/cms04-022843.pdf>.
34. AFRL, "Tactical Satellite 3 Fact Sheet," NASA Homepage, September 2009, <http://www.nasa.gov/centers/wallops/pdf/329093main-TacSat-3-fact-20sheet-20April-202009.pdf>.
35. Hecht, E., *Optics*, Addison Wesley, San Francisco, CA, 4th ed., 2002.
36. Lockwood, R. B., Cooley, T. W., Nadile, R. M., Gardner, J. A., Armstrong, P. S., Payton, A. M., Davis, T. M., and Straight, S. D., "Advanced responsive tactically effective military imaging spectrometer (ARTEMIS): system overview and objectives," *Imaging Spectrometry XII*, edited by S. S. Shen and P. E. Lewis, Vol. 6661, SPIE, 2007, p. 666102.
37. Chrien, T., Schiller, S., Silny, J., and Lockwood, R. B., "On-Orbit Calibration and Focus of Responsive Space Remote Sensing Payloads," *4th Responsive Space Conference*, AIAA, Los Angeles, CA, April 2006.
38. Lockwood, R., Cooley, T., Nadile, R., Gardner, J., Armstrong, P., Davis, T., Straight, S., Chrien, T., Gussin, E., and Makowski, D., "Advanced Responsive Tactically-Effective Military Imaging Spectrometer (ARTEMIS) Development and On-Orbit Focus," *Geoscience and Remote Sensing Symposium, 2008. IGARSS 2008. IEEE International*, Vol. 4, July 2008, pp. IV-251-IV-254.
39. Cook, R. D., and Michael E. Plesha, D. S. M., and Witt, R. J., *Concepts and Applications of Finite Element Analysis*, John Wiley and Sons, Hoboken, NJ, 4th ed., 2002.
40. Satellite Tool Kit, *Satellite Tool Kit Frequently Asked Questions*, October 2009, <http://www.stk.com/resources/faqSystem/files/2118.pdf>.
41. Fisher, R. E., "Optical Design and Engineering," *1994 OSA Annual Meeting Short Courses*, Optical Society of America, Dallas, Texas, October 1994.
42. Corson, M., "E-mail Coorespondance," October 2009, Michael Corson's response to a couple of the arthor's questions concerning HICO capabilities.
43. Thome, K., Biggar, S., Anderson, N., Czapla-Myers, J., Lockwood, R., Miller, S., Cooley, T., Chrien, T., Schiller, S., Silny, J., and Glennon, M., "Preflight and Vicarious Calibration of Artemis," *Geoscience and Remote Sensing Symposium, 2008. IGARSS 2008. IEEE International*, Vol. 1, July 2008, pp. I-249-I-252.
44. Jarecke, P. J., Yokoyama, K. E., and Barry, P., "On-orbit solar radiometric calibration of the Hyperion instrument," *Imaging Spectrometry VII*, edited by M. R. Descour and S. S. Shen, Vol. 4480, SPIE, 2002, pp. 225-230.
45. Vixen Optics, *Vixen R150S and R200SS Manual*, March 2009, <http://www.vixenoptics.com/downloads.htm>.

46. Vision Research, *Phantom V5.1 Camera Specifications*, March 2009, www.visionresearch.com/uploads/docs/.../V5/DS-v51.pdf.
47. Allied Motion Technologies Corporation, *CM-5000 Hollow Shaft Motor/Encoder Specifications*, March 2009, <http://www.alliedmotion.com/Products/Series.aspx?s=48>.
48. Quickset International, *Hercules Tripod Specifications*, March 2009, <http://www.quickset.com/pages/ultra-stable-tripods/63.php>.
49. 8020, "Company Product Catalog," March 2009, <http://www.8020.net/Product-Catalog.asp>.
50. Optics, V., "Vixen R200SS Optical Layout Drawing," March 2009, E-mailed by Mike Fowler, a support representative at Vixen Optics.
51. Swenson, E. D., "MECH542 Finite Element Analysis," March 2009, Unpublished class lecture notes of LtCol Eric D. Swenson, Astronautics Department, Air Force Institute of Technology.
52. RC Optical Systems, *Special Projects at RC Optical Systems*, September 2009, <http://www.rcopticalsystems.com/telescopes/projects.html>.
53. Swenson, E. D., "E-mail Coorespondance," November 2009, E-mail sent to RC Optics.
54. NASA, *NASA STD 6016 - Standard Materials and Process Requirements for Spacecraft*, July 2008.
55. NASA, *NASA STD 5017 - Design and Development Requirements for Mechanisms*, June 2006.
56. Miller, S. D., *Investigation of a Novel Compact Vibration Isolation System for Space Applications*, Master's thesis, Air Force Institute of Technology, Wright-Patterson AFB, March 2010.
57. NASA, *NASA STD 7001 - Payload Vibroacoustic Test Criteria*, June 1996.
58. NASA, *NASA Parts and Packaging Program - High Power Laser Diode Array Qualification and Guidelines for Space Flight Environments*, 2006.
59. Clark, J., "The Beer-Lambert Law," December 2009, <http://www.chemguide.co.uk/analysis/uvvisible/beerlambert.html>.
60. Janesick, J. R., *Scientific Charge-Coupled Devices*, SPIE Press, Bellinham, WA, 1st ed., 2001.
61. Guanter, L., Richter, R., and Moreno, J., "Spectral calibration of hyperspectral imagery using atmospheric absorption features," *Appl. Opt.*, Vol. 45, No. 10, 2006, pp. 2360–2370.

REPORT DOCUMENTATION PAGE

Form Approved
OMB No. 074-0188

The public reporting burden for this collection of information is estimated to average 1 hour per response, including the time for reviewing instructions, searching existing data sources, gathering and maintaining the data needed, and completing and reviewing the collection of information. Send comments regarding this burden estimate or any other aspect of the collection of information, including suggestions for reducing this burden to Department of Defense, Washington Headquarters Services, Directorate for Information Operations and Reports (0704-0188), 1215 Jefferson Davis Highway, Suite 1204, Arlington, VA 22202-4302. Respondents should be aware that notwithstanding any other provision of law, no person shall be subject to a penalty for failing to comply with a collection of information if it does not display a currently valid OMB control number.

PLEASE DO NOT RETURN YOUR FORM TO THE ABOVE ADDRESS.

1. REPORT DATE (DD-MM-YYYY) 25-03-2010	2. REPORT TYPE Master's Thesis	3. DATES COVERED (From - To) Jan 2009 - Mar 2010	
4. TITLE AND SUBTITLE Design Analysis of a Space Based Chromotomographic Hyperspectral Imaging Experiment		5a. CONTRACT NUMBER	
		5b. GRANT NUMBER	
		5c. PROGRAM ELEMENT NUMBER	
		5d. PROJECT NUMBER	
		5e. TASK NUMBER	
		5f. WORK UNIT NUMBER	
6. AUTHOR(S) Book, Todd A., MAJ, USA		8. PERFORMING ORGANIZATION REPORT NUMBER AFIT/GA/ENY/10-M01	
7. PERFORMING ORGANIZATION NAMES(S) AND ADDRESS(S) Air Force Institute of Technology Graduate School of Engineering and Management (AFIT/EN) 2950 Hobson Way WPAFB OH 45433-7765		10. SPONSOR/MONITOR'S ACRONYM(S)	
9. SPONSORING/MONITORING AGENCY NAME(S) AND ADDRESS(ES) Undisclosed Sponsor		11. SPONSOR/MONITOR'S REPORT NUMBER(S)	
12. DISTRIBUTION/AVAILABILITY STATEMENT APPROVED FOR PUBLIC RELEASE; DISTRIBUTION UNLIMITED			
13. SUPPLEMENTARY NOTES			
14. ABSTRACT This research develops the design of several components and/or systems for an experimental space-based chromotomographic hyperspectral imager that is being built by the Air Force Institute of Technology. The design work included three separate topics. The first topic was the development of a structure utilizing finite element analysis and eigenvalue modal analysis for the ground-based version of the chromotomographic experiment. The ground-based experiment was performed as a risk mitigation measure for the space-based experiment. The second topic included a design review of a contractor's proposed off-axis mersenne telescope for the space-based chromotomographic hyperspectral imager. The third topic addressed was a trade study of on-orbit focus, alignment and calibration schemes for the space-based version of the chromotomography experiment.			
15. SUBJECT TERMS chromotomography, hyperspectral			
16. SECURITY CLASSIFICATION OF:		17. LIMITATION OF ABSTRACT	18. NUMBER OF PAGES
a. REPORT	b. ABSTRACT	c. THIS PAGE	177
U	U	U	
		Unclassified	19a. NAME OF RESPONSIBLE PERSON Dr. Jonathan T. Black, AFIT/ENY
			19b. TELEPHONE NUMBER (Include area code) 937-785-3636, 4578

Standard Form 298 (Rev. 8-98)
Prescribed by ANSI Std. Z39-18

Form Approved
OMB No. 074-0188